Title
Coherent Diffractive Imaging with Enhanced Contrast Mechanisms

Author
Rana, Arjun

Publication Date
2021

Peer reviewed|Thesis/dissertation

UNIVERSITY OF CALIFORNIA
Los Angeles

Coherent Diffractive Imaging with Enhanced Contrast Mechanisms

A dissertation submitted in partial satisfaction
of the requirements for the degree
Doctor of Philosophy in Physics

by

Arjun Rana

2021

ABSTRACT OF THE DISSERTATION

Coherent Diffractive Imaging with Enhanced Contrast Mechanisms

by

Arjun Rana
Doctor of Philosophy in Physics
University of California, Los Angeles, 2021
Professor Jianwei Miao, Chair

Coherent diffractive imaging (CDI) is an imaging technique which uses reconstruction algorithms in place of lenses to avoid aberration, which becomes vital in the x-ray regime. Over the last two decades, CDI has served as an invaluable tool to reveal the structure and chemical composition of a wide range of material and biological systems, providing insight across many disciplines. As part of the modern scientific frontier, CDI continues to evolve as an integral tool for the investigation of increasingly complex systems, while pushing the spatiotemporal limit. This work contains three studies which demonstrate extended capabilities of CDI through the utilization of fundamental light-matter interactions in tandem with advanced algorithms.

First, the development of a novel broadband reconstruction algorithm called "Spectrum Probe and Image Reconstruction" (SPIRE) is presented in the context of attosecond imaging. An understanding of incoherent scattering permits the development of SPIRE which is shown to outperform other broadband reconstruction algorithms through the use of novel constraints. SPIRE is tested with a set of numerical simulations and a tabletop experiment with a white LED source. The results demonstrate the viability of CDI with broadband

illumination and on ultrafast time scales.

Second, x-ray magnetic circular dichroism (XMCD) is used to probe the magnetization of a geometrically confined ferromagnet on the nanoscale. A novel vector tomography algorithm titled “Vector REal Space Iterative Reconstruction Engine (Vector RESIRE)" is used to directly reconstruct the 3D magnetization vector field in addition to the sample structure, without any prior assumptions. Topological analysis of the reconstruction result reveals a network of non-trivial magnetic point defects known as hedgehogs. The 3D spatial distribution of hedgehogs serve to validate the current theory of hedgehog confinement and potential of metalattices in spintronics applications.

In the appendix, polarization-dependent imaging contrast (PIC) is used to map the orientation of the crystal c-axis of calcium carbonate in a coral skeleton. Hierarchical clustering is applied to 4D scanning transmission electron microscope (STEM) data from the same sample to gain additional information about the crystal grain structure. The PIC and 4D STEM results are correlated to elucidate growth and nucleation conditions for coral.

The dissertation of Arjun Rana is approved.

Pietro Musumeci

Jose A. Rodriguez

Shenshen Wang

Jianwei Miao, Committee Chair

University of California, Los Angeles

2021

To the memory of my parents . . .

who always encouraged my academic pursuits

and set me on this path,

but could not be here to see its end.

TABLE OF CONTENTS

LIST OF FIGURES

LIST OF TABLES

ACKNOWLEDGMENTS

Firstly I'd like to thank my advisor John Miao for his thoughtful mentorship during the years I've spent in the Coherent Imaging group. As a pioneer in CDI, John's perspective has been invaluable in guiding the path of my graduate research. Additionally, I acknowledge my committee for the time and effort they've spent to evaluate this work. Thank you to all the past and present members of the Coherent Imaging group, and collaborators from all over the world.

Minh—for the heated discussions about physics and math, and the numerous collaborations that followed.
Mike—for being in the trenches beside me through countless beamtimes, and sharing the best office in Knudsen.
David, Paul—for being my study partners for the comp, roommates for many years, and good friends.
Adam, Rich, Dani—my de facto brothers. Thank you for always being there.

Lastly, a special acknowledgment to R.T. Chach whose love and support motivated me to persevere through difficult times and complete my graduate work.

Chapter 2 is an adapted and partially modified version, including figures, of the article "Potential of Attosecond Coherent Diffractive Imaging", *Phys. Rev. Lett.* **125**, 086101 (2020). Copyright (2020) by the American Physical Society. I acknowledge the coauthors for their contributions: J. Zhang, M. Pham, A. Yuan, Y. H. Lo, H. Jiang, S. Osher and J. Miao.

Chapter 3 is an adapted and partially modified version, including figures, of the article "Direct observation of geometry-confined 3D topological spin textures", *in prep.*, (2021). I acknowledge the coauthors for their contributions: C.-T. Liao, E. Iacocca, J. Zou, M. Pham, E. Cating Subramanian, Y. H. Lo, S. Ryan, X. Lu, C. Bevis, R. Karl, A. Glaid, Y.-S. Yu, D. Shapiro, S. Yazdi, S. Osher, H. Kapteyn, V. Crespi, J. Badding, Y. Tserkovnyak, M. Murnane and J. Miao.

Appendix A is an adapted and partially modified version, including figures, of the article "X-ray linear dichroic ptychography", *Proc. Natl. Acad. Sci. USA* **118**, e2019068118 (2021). Copyright (2021) National Academy of Sciences. I acknowledge the coauthors for their contributions: Y. H. Lo, J. Zhou, D. Morrill, C. Gentry, B. Enders, Y.-S. Yu, C.-Y. Sun, D. A. Shapiro, R. W. Falcone, H. C. Kapteyn, M. M. Murnane, P. U. P. A. Gilbert, and J. Miao.

I acknowledge support by STROBE: A National Science Foundation Science and Technology Center under Grant No. DMR 1548924 and the Office of Basic Energy Sciences of the US DOE (DE-SC0010378).

VITA

2016–2021	NSF STROBE Graduate Fellow
2015, 2016–2021	Graduate Student Researcher Coherent Imaging Group Department of Physics and Astronomy *University of California, Los Angeles* Los Angeles, California
2013–2016	Graduate Teaching Assistant Department of Physics and Astronomy *University of California, Los Angeles* Los Angeles, California
2011	B.A. Physics Department of Physics and Astronomy *Rutgers University* New Brunswick, New Jersey

PUBLICATIONS

A. Pryor Jr.*, Y. Yang*, **A. Rana**, et al., "GENFIRE: A generalized Fourier iterative reconstruction algorithm for high-resolution 3D imaging", *Scientific Reports* **7**, 10409 (2017)

Y. H. Lo, L. Zhao, M. Gallagher-Jones, **A. Rana**, J. J. Lodico, W. Xiao, B.C. Regan and J. Miao, "In situ coherent diffractive imaging", *Nature Communications* **9**, 1826 (2018)

A. Pryor, Jr., **A. Rana**, et al., "Single-shot 3D coherent difractive imaging of core-shell nanoparticles with elemental specifcity", *Scientific Reports* **8**, 8284 (2018)

M. Pham, P. Yin, **A. Rana**, S. Osher and J. Miao, "Generalized proximal smoothing (GPS) for phase retrieval", *Optics Express* **27**, 2792-2808 (2019)

Y. H. Lo, C. Liao, J. Zhou, **A. Rana**, et al., "Multimodal x-ray and electron microscopy of the Allende meteorite", *Science Advances* **5**, eaax3009 (2019)

M. Pham, **A. Rana**, J. Miao and S. Osher, "Semi-implicit relaxed Douglas-Rachford algorithm (sDR) for ptychography", *Optics Express* **22**, 31246 (2019)

A. Rana*, J. Zhang*, M. Pham, A. Yuan, Y. H. Lo, H. Jiang, S. Osher and J. Miao, "Potential of attosecond coherent diffractive imaging", *Physical Review Letters* **125**, 086101 (2020)

D.J. Chang, D.S. Kim, **A. Rana**, X. Tian, J. Zhou, P. Ercius, and J. Miao, "Ptychographic atomic electron tomography: Towards three-dimensional imaging of individual light atoms in materials", *Physical Review B* **102**, 174101 (2020)

Y. H. Lo, J. Zhou, **A. Rana**, et al., "X-ray linear dichroic ptychography", *Proceedings of the National Academy of Sciences* **118**, e2019068118 (2021)

Y. Yang*, J. Zhou*, F. Zhu*, Y. Yuan*, D. Chang, D. S. Kim, M. Pham, **A. Rana**, X. Tian, Y. Yao, S. Osher, L. Hu, P. Ercius and J. Miao, "Determining the three-dimensional atomic structure of an amorphous solid", *Nature*, (in press)

A. Rana*, C.-T. Liao*, et al., "Direct observation of geometry-confined 3D topological spin textures", *in preparation* (2021)

* denotes equal contribution

CHAPTER 1

Technical background

This chapter provides a brief introduction to the scientific and technical principles that form the foundation of this work. A full treatment of the topics contained in this chapter can be found in the cited references.

1.1 CDI

Coherent diffractive imaging (CDI), the underlying basis of this work, is an imaging technique that uses computational phase retrieval algorithms in lieu of lenses to reconstruct an image from scattered illumination. The origins of CDI lie in a brief note published by Sayre in 1952 [1]. In light of the recently published Nyquist-Shannon sampling theorem, Sayre presents the possibility of reconstructing the electron density of an isolated object from its Fourier transform, provided the phases are known. This note served as the formal problem statement for CDI—to recover $T(x, y)$ when given the measurement $M(k_x, k_y) = |\mathcal{F}\{T(x, y)\}|^2$, where $T(x, y)$ is the projected transmission function of the object, $\mathcal{F}$ is the Fourier transform and $M(k_x, k_y)$ is the measured diffraction pattern intensity. The transmission function corresponds to the complex index of refraction of the material,

$$T(x, y) \propto e^{\frac{2\pi i}{\lambda} \int \delta(x,y,z) + i\beta(x,y,z)\, dz} \tag{1.1}$$

and thus maps the structure of the object with chemical specificity.

The importance of the missing phases is illustrated by the canonical “phase swapping" example in fig. 1.1.

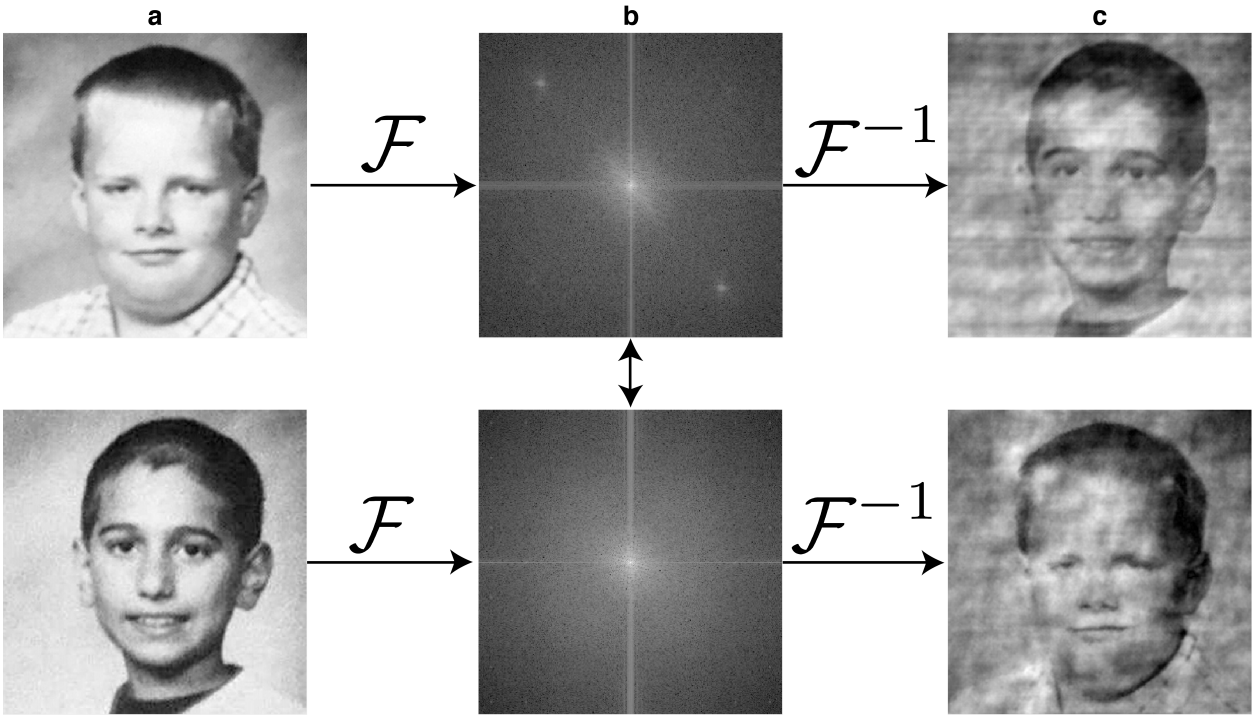

Figure 1.1. An example to illustrate the importance of phases. **(a)** The real space images of two school children. **(b)** The two images in (a) are Fourier transformed and their phases exchanged while leaving the magnitudes unchanged.**(c)** After inverse Fourier transform, the original images from (a) appear to be switched, exemplifying the importance of the phase in image reconstruction.

1.1.1 The oversampling theorem

The key to solving the phase problem in CDI is the oversampling of the diffraction intensity. Although the oversampling concept was proposed by Bates [2], Miao formulated the oversampling theorem [3, 4], which laid the foundation for the eventual first experimental demonstration of CDI by Miao et al. in 1999 [5]. Oversampling sets a rigorous Fourier space sampling condition in order to perform phase retrieval of an isolated, non-crystalline object.

The oversampling theorem can be understood by considering x_N, a $1D$ discrete signal of length N. The measured data correspond to the magnitudes of the discrete Fourier transform (DFT) of x_N

$$|X_k| = \sum_{n=0}^{N-1} |x_n e^{\frac{2\pi i k n}{N}}| \ , \qquad k = \{0, \ldots, N-1\} \ . \tag{1.2}$$

In the case where x_N is purely real, $|X_k|$ contains $N/2$ unique data points due to Hermitian symmetry. Similarly, in the case where x_N is complex, $|X_k|$ contains N data points, but $2N$ points need to be recovered corresponding to the magnitudes and phases of x_N. From the perspective of information conservation, there is an incompatibility between the amount of data contained in the measurement and the amount required to reconstruct the signal. Another important component of the oversampling method lies in the fact that the diffraction pattern of a non-crystalline object is continuous, and thus may be sampled at arbitrarily fine sampling intervals. If we zero-pad x_N to length $2N$,

$$\begin{aligned} x_{Np} &= \{x_N, \overbrace{0, \ldots, 0}^{N}\} \\ |X_{kp}| &= \sum_{n=0}^{2N-1} |x_{np} e^{\frac{2\pi i k n}{2N}}| \\ &= \sum_{n=0}^{N-1} |x_n e^{\frac{2\pi i k n}{2N}}| \ , \qquad k = \{0, \ldots, 2N-1\} \end{aligned} \tag{1.3}$$

we see that padded signal x_{Np} solves the data imbalance problem. Returning to information conservation, the concatenation of an a priori quantity of zeros to x_N effectively reduces the amount of data to be recovered. Equivalently, the amount of information in the measurement $|X_{kp}|$ is twice that of $|X_k|$, while the non-trivial size of the signal to be recovered, x_N, remains unchanged. The experimental requirements imposed by the oversampling criteria can be summarized by σ, the oversampling ratio

$$\sigma = \frac{N_{total}}{N_{unknown}} \geq 2 \tag{1.4}$$

where N_{total} is the total size of the discrete signal and $N_{unknown}$ is the size of the non-zero region [3]. For an n-dimensional image, the oversampling ratio in each dimension relates to the oversampling degree O as

$$O = \sigma^{(1/dim(\mathbb{R}^n))} \ . \tag{1.5}$$

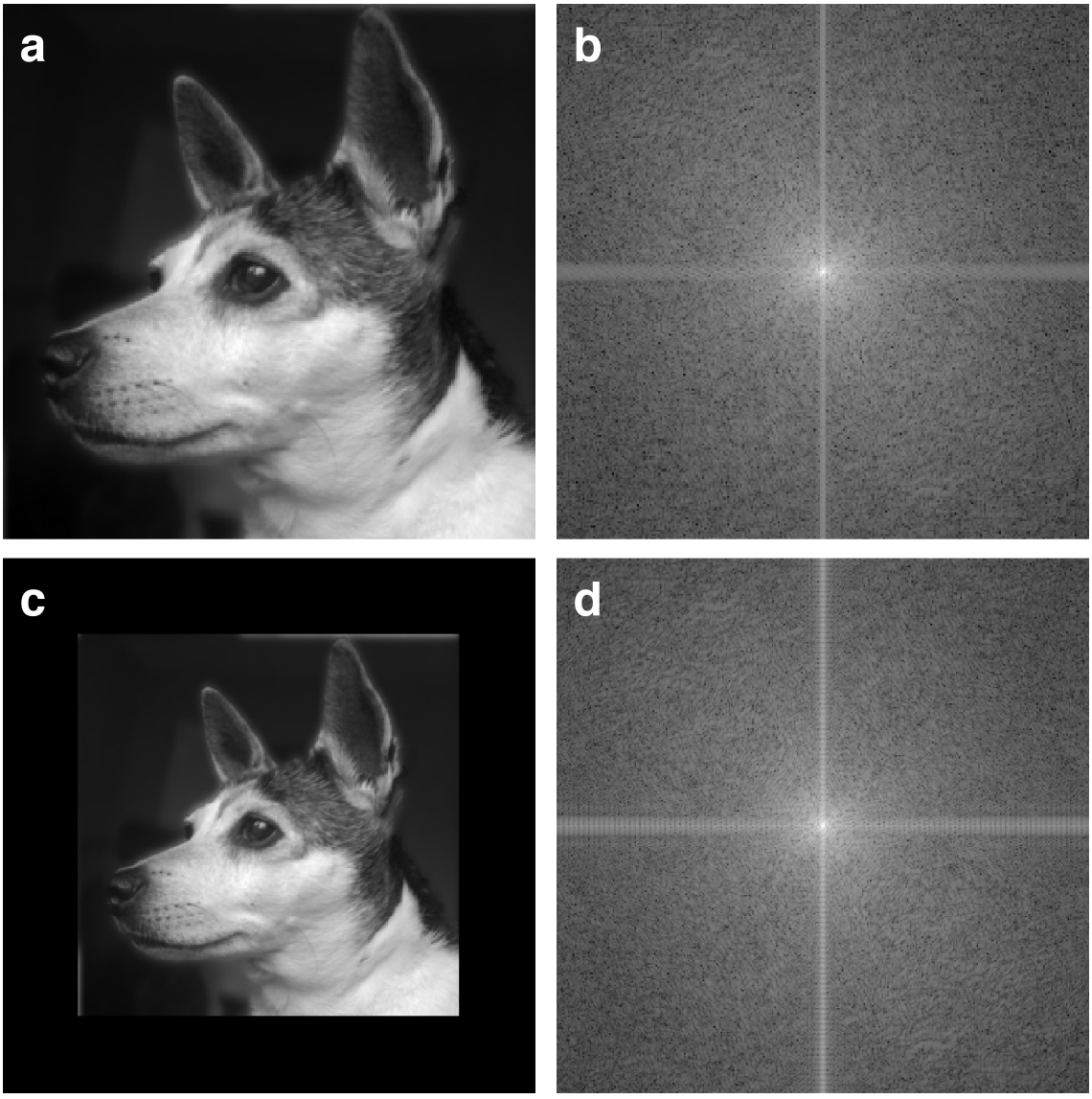

Figure 1.2. An example of oversampling in 2D. **(a)** An image of a dog and **(b)** the corresponding Fourier magnitudes. **(c)** An oversampled version of the image shown in (a), with $\sigma = 2$ and **(d)** the corresponding Fourier magnitudes.

The oversampling criterion imposes direct constraints on experimental parameters, which may be understood by considering the elementary example of $1D$ single slit diffraction. Figure 1.3 illustrates the experimental schematic, where coherent illumination of wavelength λ is incident on a slit of length a, representing the sample to be imaged. This sample is placed a distance D from a detector of pixel size P.

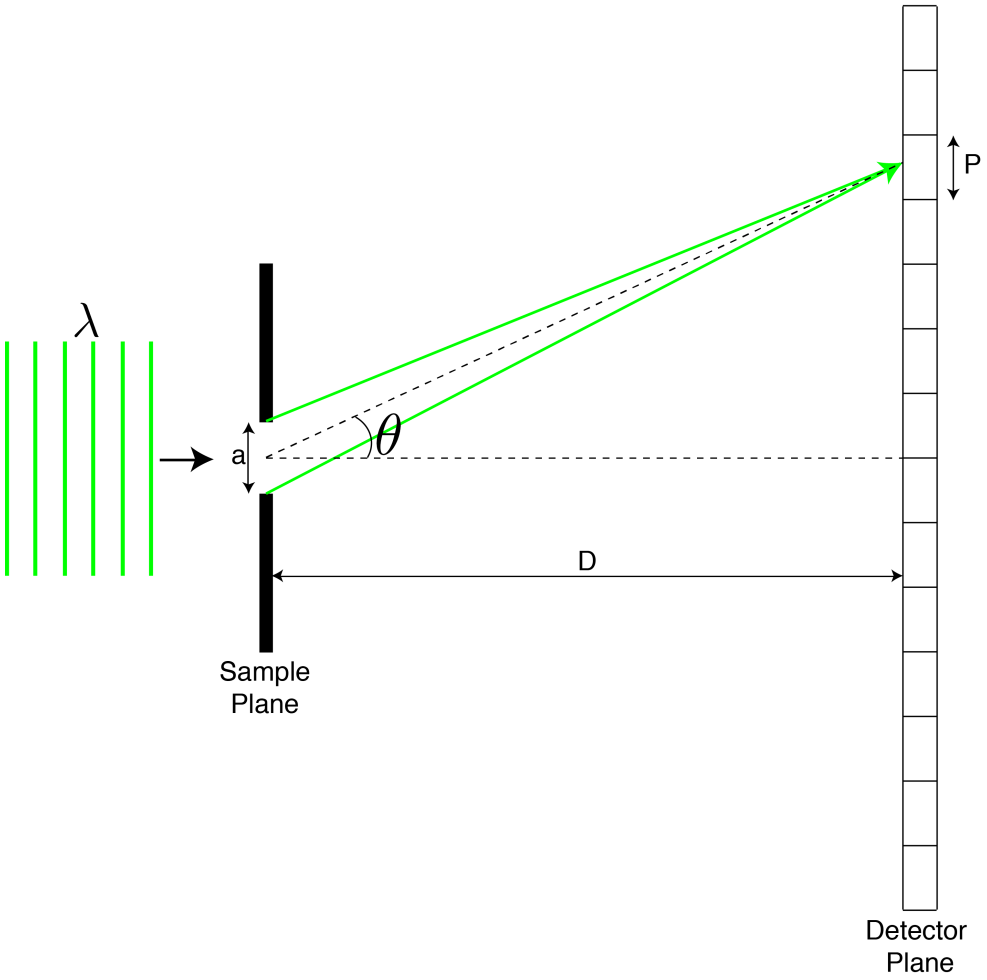

Figure 1.3. Oversampling in the context of single slit diffraction. Coherent illumination of wavelength λ is incident on a slit of width a. We consider the interference fringes observed on a discrete detector placed a distance D away from the slit.

If we consider all the light arriving at a pixel situated at an angle θ with respect to the optical axis, the path length difference between light arriving at the pixel from opposite ends of the sample is $s = asin\theta \approx a\theta$ (with the far-field approximation). The constructive interference condition

$$a\theta_n = n\lambda \ , \qquad n = 1, 2, 3, \ldots \tag{1.6}$$

determines that maxima occur with angular spacing $\delta_a = \lambda/a$. Consequently, the separation of adjacent maxima on the detector plane is $D\delta_a$ and can be expressed in reciprocal space as

$$\omega = \frac{1}{D\delta_a} = \frac{a}{\lambda D} \ . \tag{1.7}$$

Oversampling requires that the sampling frequency of the detector, ω_p, must be at least twice ω in order to have sufficient data for phase retrieval

$$\omega_p = \frac{1}{P} \geq \frac{2a}{\lambda D} \tag{1.8}$$

and thus constrains the experimental parameters

$$O \equiv \frac{\lambda D}{aP} \geq 2 \ . \tag{1.9}$$

1.1.2 Experimental demonstration of CDI

The first experimental demonstration of CDI utilized soft x-rays to illuminate a sample made of gold nano-dots arranged into a pattern of six letters, as shown in fig. 1.4a. The diffraction pattern shown in fig. 1.4c was collected in accordance with the oversampling theorem, and then reconstructed at a resolution of ~ 75 nm as seen in fig. 1.4d.

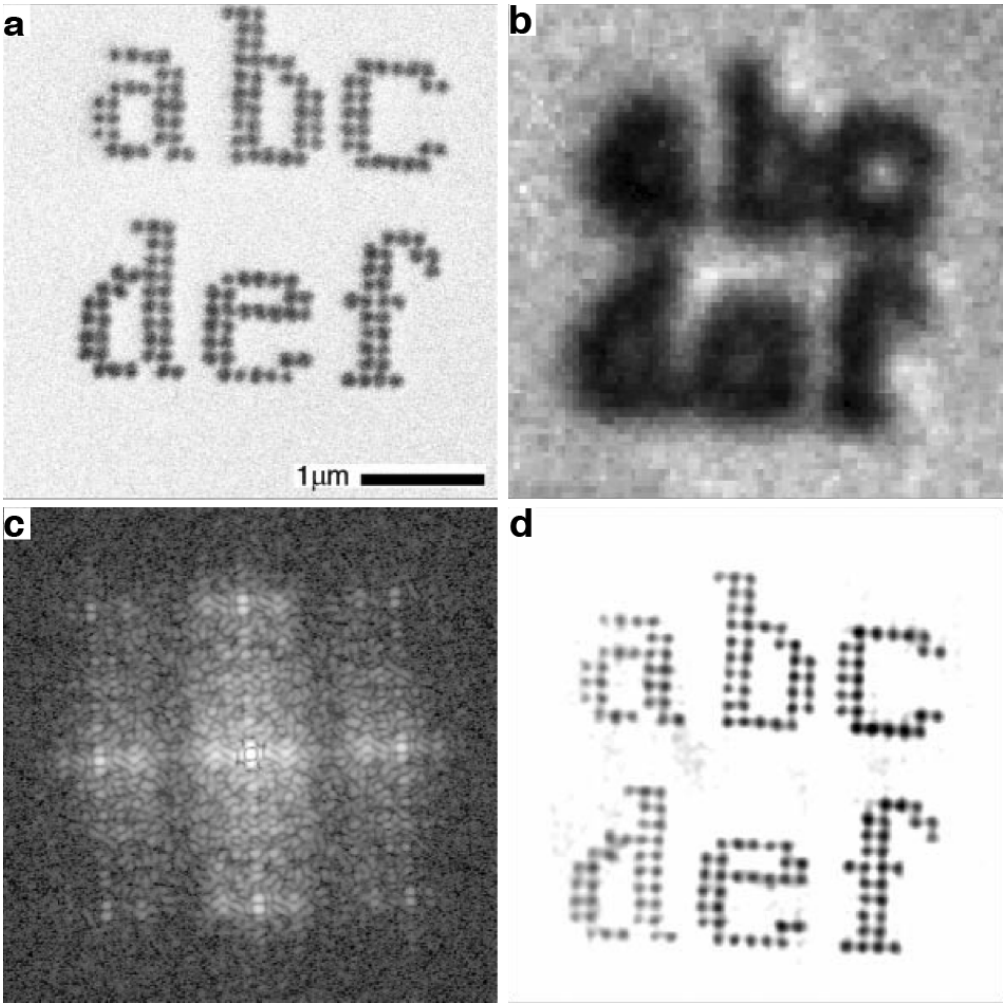

Figure 1.4. The first experimental demonstration of CDI. **(a)** A scanning electron microscope image of the specimen. The specimen was fabricated by depositing gold dots, each $\sim$ 100 nm in diameter and 80 nm thick, on a silicon nitride membrane. **(b)** An optical microscope image of the specimen. **(c)** A diffraction pattern of the specimen (using a logarithmic intensity scale). The central 15-pixel-radius circular area is supplied by the squared magnitude of the Fourier transform of the optical microscope image (b). **(d)** The specimen image as reconstructed from the diffraction pattern of (c). *Reprinted by permission from Springer Nature: Nature [5], copyright (1999).*

1.1.3 Resolution in CDI

The achievable resolution of CDI with a given experimental setup can be understood by considering the momentum space representation of the example shown in fig. 1.3, which is illustrated below in fig. 1.5.

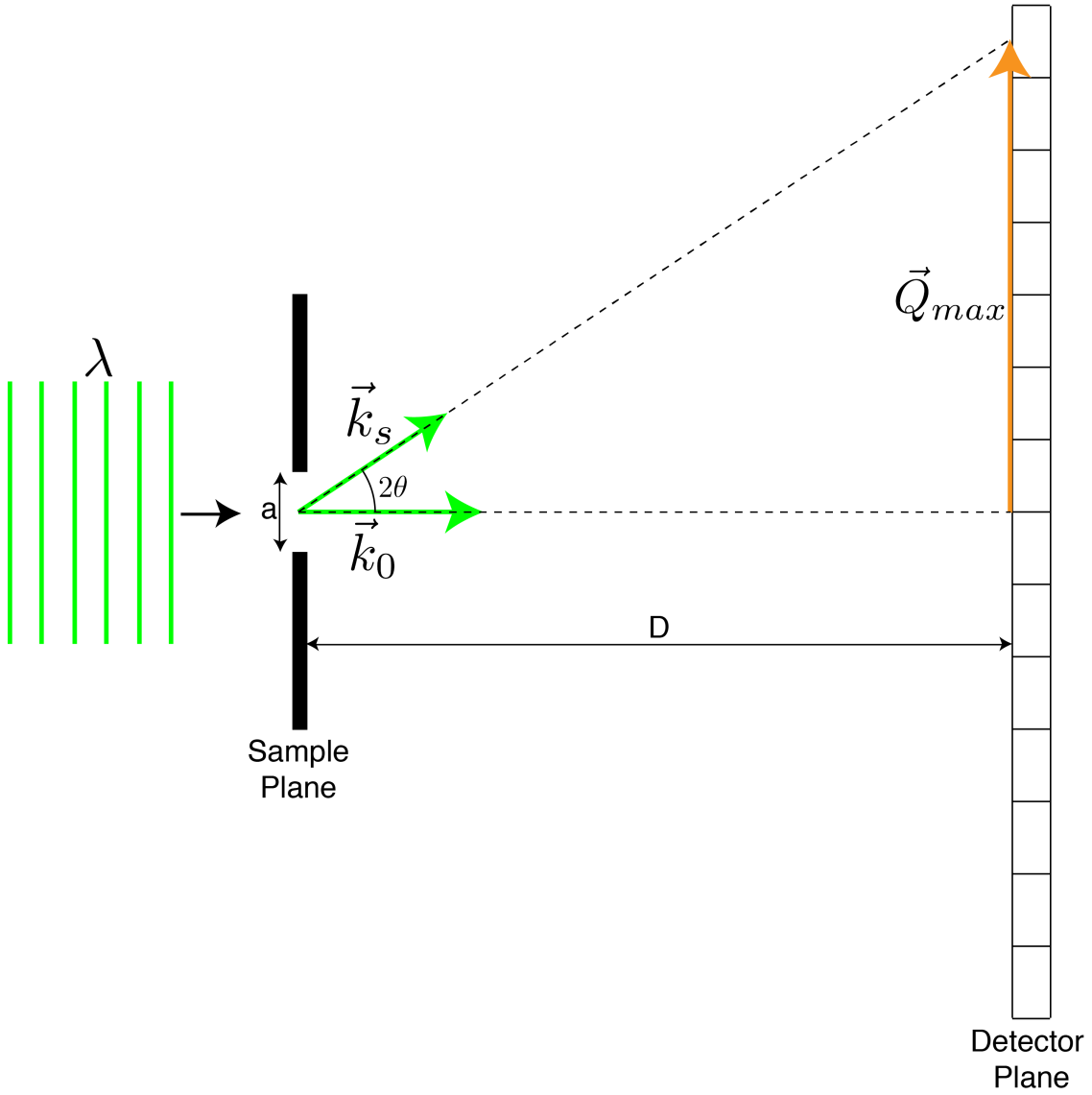

Figure 1.5. Diffraction limited resolution in the context of single slit diffraction. In momentum space, an incident wave-vector $\vec{k}_0$ is scattered to $\vec{k}_s$ at an angle 2θ, resulting in a momentum transfer of $\vec{Q}_{max}$.

Elastic scattering imposes that the incident and scattered wave-vectors are equal in magnitude

$$|\vec{k}_0| = |\vec{k}_s| = \frac{2\pi}{\lambda} \ , \tag{1.10}$$

implying that $\vec{k}_0$, $\vec{k}_s$ and the maximum scattering vector $\vec{Q}_{max}$ form an isosceles triangle from which the magnitude of $\vec{Q}_{max}$ can be calculated

$$|\vec{Q}_{max}| = \frac{4\pi}{\lambda} sin\frac{2\theta}{2} \ . \tag{1.11}$$

Bragg's condition for constructive interference states that the momentum transfer must point between two reciprocal lattice points, so that $\vec{Q}_{max}$ corresponds to d, the diffraction limited resolution in real space

$$d = \frac{2\pi}{|\vec{Q}_{max}|} = \frac{\lambda}{2sin\theta} \tag{1.12}$$

of a CDI instrument which can collect scattered light up to an angle 2θ.

1.1.4 HIO

Oversampling is a statement about the feasibility of phase retrieval, but does not provide a solution for the problem. Optimization is a branch of mathematics dedicated to solving a family of problems, including phase retrieval. A detailed overview is out of the scope of this work, but an example of a simple phase retrieval algorithm is discussed here to aid understanding of more complex algorithms implemented in the later chapters of this work[†]. A flow diagram of one such algorithm, Hybrid Input-Output (HIO) [7] is shown in fig. 1.6.

[†]see [6] for a good introduction to optimization

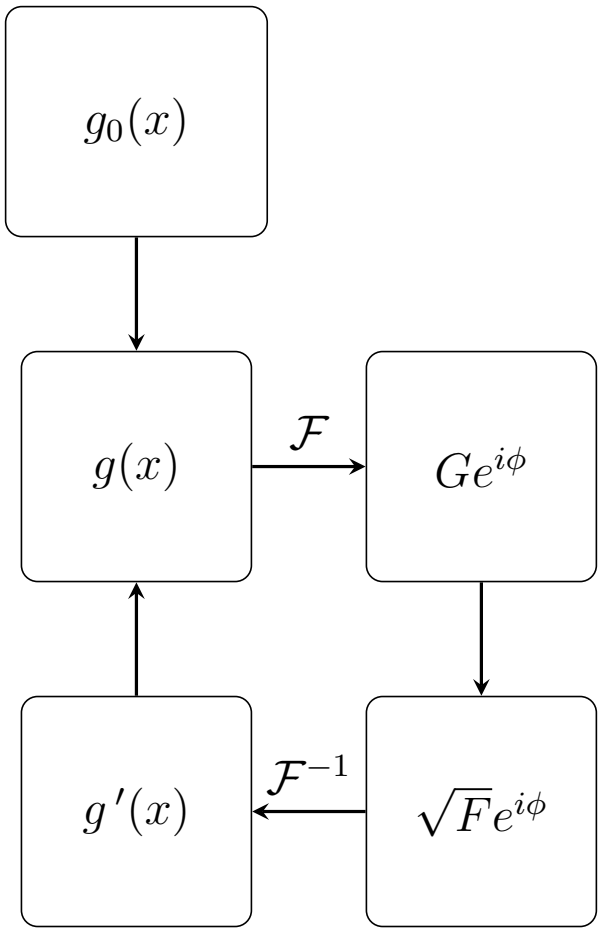

Figure 1.6. The Hybrid Input-Output (HIO) Algorithm for phase retrieval.

The reconstruction is initiated by providing an initial guess of the object, $g_0(x)$. After a Fourier transform, the magnitudes are replaced by those from the measured diffraction pattern, while leaving the phases unchanged

$$G'(k) = \frac{G(k)\sqrt{F(k)}}{|G(k)|} \tag{1.13}$$

where $G(k) = \mathcal{F}\{g(x)\}$ and $F(k)$ is the measured diffraction pattern intensity. The updated Fourier object $G'(k)$ is inverse Fourier transformed to $g'(x)$, after which the support constraint is applied

$$g_{updated} = \begin{cases} g'(x) & x \in \mathcal{S} \\ g(x) - \beta g'(x) & x \notin \mathcal{S} \end{cases}, \tag{1.14}$$

where β is a step size typically between 0.1 and 0.9 and $\mathcal{S}$ is the support. Finally, $g_{updated}$ is used as the input for the next iteration and the algorithm continues to refine $g(x)$ with sequential application of the Fourier- and real- space constraints. An error metric is monitored while the reconstruction iterates

$$Error = \sum_k \frac{|G_{updated} - \sqrt{F}|}{\sqrt{F}}, \tag{1.15}$$

to check for convergence and determine if the stopping condition has been met.

1.2 Conventional ptychography

Until this point, we have considered CDI as a phase retrieval problem consisting of a single measurement. Ptychography is a multi-shot variation of CDI which utilizes data redundancy to produce more robust reconstructions than the classical single-shot method[†]. First demonstrated in the x-ray regime by Rodenburg et al. [9], ptychography requires the collection of many diffraction patterns, as a confined illumination source (the "probe") is scanned over an arbitrarily large object. A crucial criterion is that the probe must partially overlap at adjacent scan positions, thus forming a powerful redundancy constraint on the reconstruction. The formal problem statement can be written as

$$\begin{aligned} &minimize && \sum_{j=1}^{N} \left\| \Psi_j - \sqrt{I_j} \right\|^2 \\ &subject\ to && \psi_j = P(r)\ O(r - r_j) \end{aligned} \tag{1.16}$$

[†] An extensive overview of ptychography can be found in [8]

where j indexes the scan position, I is the measured diffraction pattern, P is the probe, O is the extended object and ψ is the exit wave. The constraint in the second line of eq. 1.16 is the thin object approximation, which assumes that the exit wave may be modeled as the product of the probe and object functions. A solution is reached when a probe and object have been recovered, such that the error is minimized over all N scan positions. Similarly to conventional CDI, ptychography is still an open area of research in physics and applied mathematics, with novel algorithms under continuous development [10]. A simple example is discussed here to illustrate the methodology of ptychographic phase retrieval.

1.2.1 ePIE

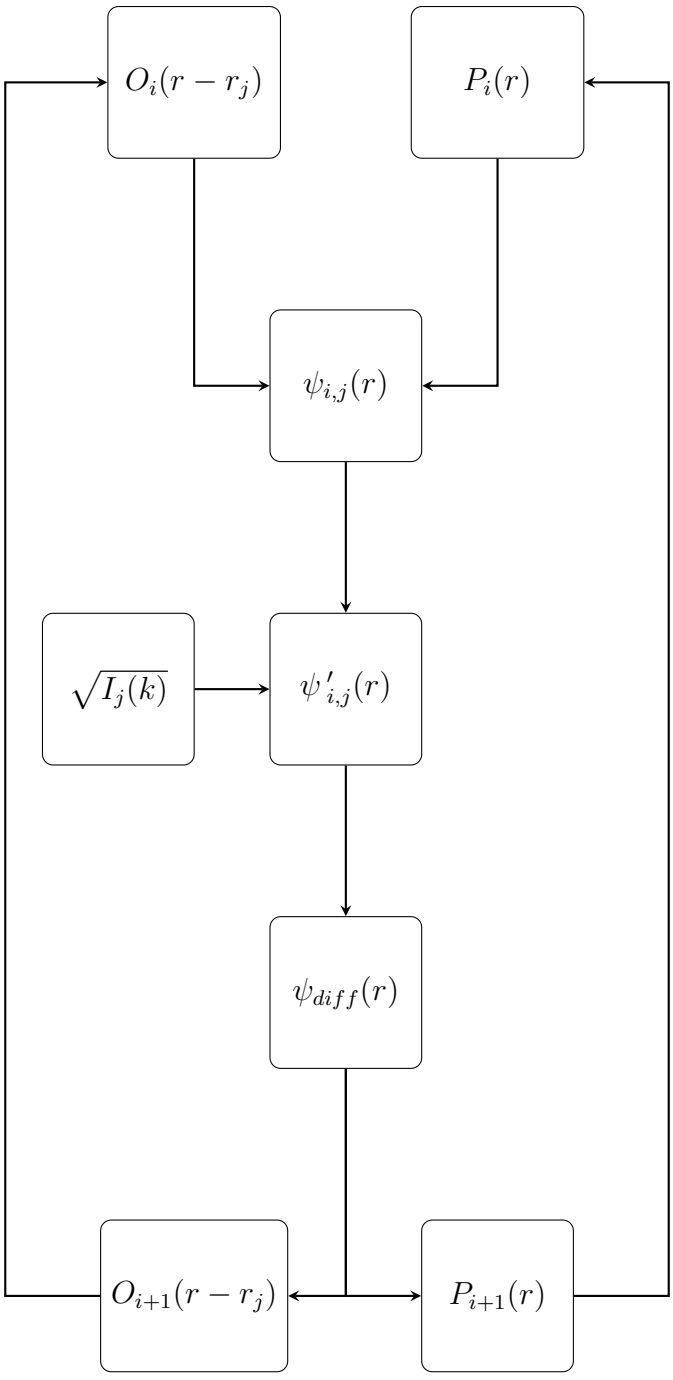

Figure 1.7. A flowchart illustrating a single micro-iteration of the extended Ptychographical Iterative Engine (ePIE).

The extended ptychographical iterative engine (ePIE) shown in the flowchart in fig. 1.7 allows for the simultaneous reconstruction of O and P [11]. In the first step, the shifted object $O_i(r - r_j)$ and probe guess $P_i(r)$ are multiplied to create the exit wave corresponding to scan position j, $\psi_{i,j}(r)$. In the next step, the measured data are enforced by replacing the Fourier magnitudes of $\Psi_{i,j}(k)$ with the measured data

$$\psi'_{i,j}(r) = \mathcal{F}^{-1}\left\{\frac{\Psi_{i,j}(k)\sqrt{I_j(k)}}{|\Psi_{i,j}(k)|}\right\} \tag{1.17}$$

where $\Psi(k)$ is the Fourier transform of $\psi(r)$ and $I(k)$ is the measured diffraction pattern intensity. Now, the differential exit wave, $\psi_{diff} = \psi'_j - \psi_j$ is used to perform the probe and object updates

$$\begin{aligned} O_{i+1}(r - r_j) &= O_i(r - r_j) + \alpha\frac{P_i^*(r)}{|P_i(r)|^2_{max}}\psi_{diff} \\ P_{i+1}(r) &= P_i(r) + \beta\frac{O_i^*(r - r_j)}{|O_i(r - r_j)|^2_{max}}\psi_{diff} \end{aligned} \tag{1.18}$$

where α, β are constants that modulate the step size of the object and probe update, respectively. The update eqs. 1.18 can be derived by taking partial derivatives of the error metric in eq. 1.16 with respect to O and P. One macro-iteration of ePIE consists of performing the aforementioned updates over all scan positions. As the algorithm continues to iterate, the error metric

$$R_{i,j} = \frac{\sum_k |\sqrt{I_j(k)} - \Psi_{i,j}(k)|}{\sum_k \sqrt{I_j(k)}} \tag{1.19}$$

is used to monitor convergence.

1.3 Coherence

Thus far, CDI and ptychography have been discussed under the implicit assumption of coherent illumination[†].

[†] For a thorough treatment of coherence, see: [12, 13]

Here, coherence means the illumination is spatially coherent over the extent of the sample and quasi-monochromatic

$$\begin{matrix} a \ll \Delta l \\ \Delta\lambda/\bar{\lambda} \ll 1 \end{matrix} , \tag{1.20}$$

where a is the spatial extent of the sample and Δl is the coherence width. In reality, all physical sources exhibit some degree of incoherence, making it important to understand and assess the impact of coherence on the feasibility of phase retrieval.

1.3.1 Interference

Fundamentally, coherence arises from interference, and therefore is innately linked to diffraction and CDI. We begin by considering two quasi-monochromatic fluctuating waves originating from two different points in space

$$\begin{aligned} U_1(t) &= A_1 e^{\phi_1(t) - \bar{\omega}t} , \\ U_2(t) &= A_2 e^{\phi_2(t) - \bar{\omega}t} . \end{aligned} \tag{1.21}$$

A detector is placed at a distant point where the two waves interfere, and the resulting wave is a superposition of the two originating waves

$$U(t) = U_1(t) + U_2(t) . \tag{1.22}$$

However, the oscillation period is extremely short compared to the measurement interval T of the detector, so the measured quantity is time averaged intensity $\langle I(t) \rangle_T$ of the wave,

$$\begin{aligned} \langle I(t) \rangle_T &= \left\langle |U(t)|^2 \right\rangle_T \\ &= \left\langle |U_1(t)|^2 \right\rangle_T + \left\langle |U_2(t)|^2 \right\rangle_T + \left\langle |U_{12}(t)|^2 \right\rangle_T \\ &= \langle I_1(t) \rangle_T + \langle I_2(t) \rangle_T + \langle I_{12}(t) \rangle_T \ . \end{aligned} \tag{1.23}$$

When the two waves have no statistical correlation, the cross-term vanishes

$$< I_{12} >_t = \int A e^{\phi_1(t) + \phi_2(t) - \bar{\omega}t} dt = 0 . \tag{1.24}$$

This is also true when the quasi-monochromatic assumption is violated, as in the case of broadband light

$$\left\langle |U_{12}(t)|^2 \right\rangle_T = \left\langle I_{12} \right\rangle_T = \int A e^{\phi_1(t)+\phi_2(t)-\omega_1 t-\omega_2 t} dt = 0 \ . \tag{1.25}$$

In general, the cross term can take values between 0 and 1 corresponding to complete incoherence and complete coherence, respectively. The coherence characteristics of a light source are completely described by γ, the complex degree of coherence

$$\begin{aligned} \gamma(q_1, q_2, \tau) &= \frac{< U^*(q_1, t) U(q_2, t+\tau >}{\sqrt{I(q_1}\sqrt{I(q_2)}} \ , \\ 0 \leq |\gamma| &\leq 1 \ . \end{aligned} \tag{1.26}$$

1.3.2 Spatial and temporal coherence

In order to characterize the coherence of a particular light source, we must consider both temporal and spatial coherence. Temporal coherence is directly related to the bandwidth of the source $\Delta\lambda$, and is a measure of the correlation of between two beams of light from the same source as a function of relative time delay between them. The coherence time can be expressed as a length, given by

$$\Delta l_t = \frac{2\pi c}{\Delta\omega} = \left(\frac{\bar{\lambda}}{\Delta\lambda}\right) \ \bar{\lambda} \ . \tag{1.27}$$

The temporal coherence of a light source can be measured using a Michelson interferometer, as seen in fig. 1.8A. Light emanating from a source $\mathcal{S}$ is incident on a beam splitter $\mathcal{M}_0$. The split beam is reflected from mirrors $\mathcal{M}_1$ and $\mathcal{M}_2$ with differing path lengths. The reflected beams are recombined and the presence of interference fringes is observed on the detector plane $\mathcal{D}$.

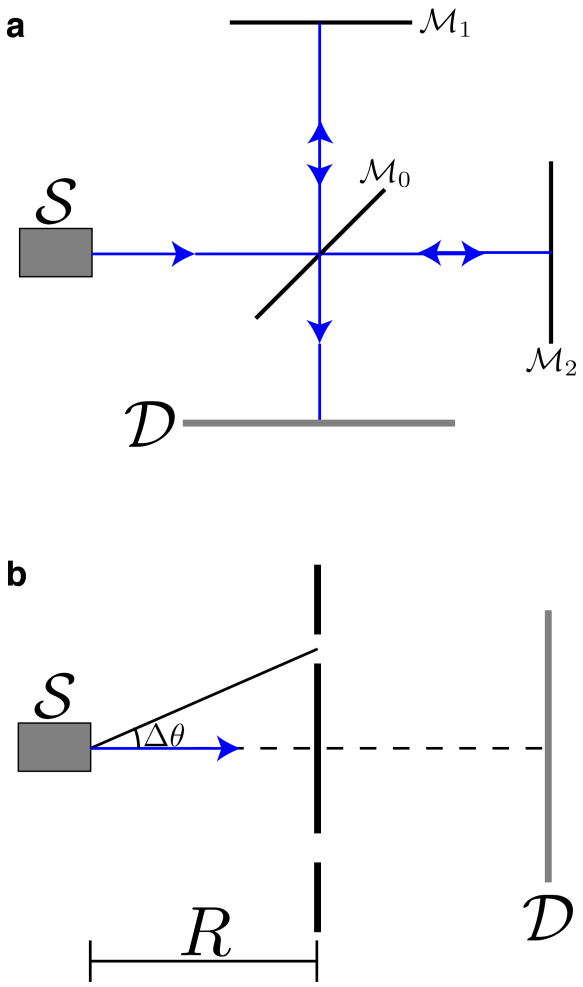

Figure 1.8. Interferometer schematics. **(a)** A Michelson interferometer for measuring temporal coherence. **(b)** A Young's double slit interferometer for measuring spatial coherence.

Spatial coherence is a measure of the correlation between two waves that originate from different points in space, and can be quantified by the spatial coherence length Δl_s. The spatial coherence length can be experimentally determined with a Young's double slit interferometer, as seen in fig. 1.8B in which light is incident on an opaque screen with two pinholes with angular separation $\Delta\theta$ from the optical axis. The maximum effective pinhole separation, $R\Delta\theta$, at which fringes are observed on the detection plane $\mathcal{D}$ determines the degree of spatial coherence of the light source.

1.3.3 Partially coherent ptychography

The ptychography problem statement described in eq. 1.16 assumes perfect coherence as described in the beginning of this section. This implies the measured diffraction pattern intensity at scan position j, corresponds to

$$I_j = |\mathcal{F}\{\psi_j\}|^2 \,. \tag{1.28}$$

However, if the incident light is now broadband, eq. 1.25 implies that the measured diffraction pattern corresponds to an incoherent sum

$$I_j = \sum_{\lambda} |\mathcal{F}_\lambda\{\psi_{j,\lambda}\}|^2 \,, \tag{1.29}$$

where the exit waves ψ_j and the Fourier propagator $\mathcal{F}$ are now functions of the wavelength λ. Chapter 2 pertains to solving the incoherent ptychography problem in the context of attosecond illumination, which is inherently broadband due to the uncertainty principle.

1.4 X-ray magnetic circular dichroism

1.4.1 Background and physical origin

X-ray magnetic circular dichroism (XMCD) is an effect, theoretically investigated by Stern et al. [14, 15] and first experimentally observed by Schütz et al. [16], that describes an absorption contrast dependence on the relative orientation between the helicity of incident circularly polarized x-rays and the local magnetization of the sample[†]. The effect has been shown to be exceptionally pronounced at the L-edges of the $3d$ transition metals, which fall in the soft x-ray regime [19].

The origin of XMCD can be understood by considering photoabsorption of an atomic electron. Using Fermi's golden rule, we can express the transition probability of the electron

[†] A good overview of XMCD can be found in [17] and an in-depth treatment in [18]

from an initial core shell state $|i\rangle$ to an excited valence shell state $|f\rangle$

$$w_{i\to f} \propto \langle f|\mathbf{A}\cdot\mathbf{p}|i\rangle^2\,\delta\left(E_f - E_i\right)g(E_f)\ , \tag{1.30}$$

where $\mathbf{A}$ is the vector potential of the incident electromagnetic wave, $\mathbf{p}$ is the momentum operator and $g(E_f)$ is the density of final states given by the number of holes, N_h, in the valence shell. In the dipole approximation (E1), it is assumed the wavelength of the incident light is much larger than the atomic radius. Therefore, we take the first term in the expansion of the vector potential, $\mathbf{A} \approx 1$, and the transition probability can be re-written[†] as

$$w_{i\to f} \propto \langle f|\hat{\epsilon}\cdot\mathbf{p}|i\rangle^2 \tag{1.31}$$

where $\hat{\epsilon}$ is the photon polarization direction. Since both $\hat{\epsilon}$ and $\mathbf{p}$ can be expressed with spherical harmonics, the Wigner-Eckart theorem allows us to express the transition probability as a product of a purely radial and purely angular term,

$$w_{i\to f} \propto \overbrace{\langle R_f|\mathbf{r}|R_i\rangle}^{\text{radial}}\ \overbrace{\sum_q \langle j_f, m_f|T^{(q)}|j_i, m_i\rangle}^{\text{angular}}\ . \tag{1.32}$$

The transition matrix $T^{(q)}$ can be evaluated using the relevant Clebsch-Gordan coefficients to obtain the dipole selection rules for circularly polarized photons

$$\Delta m = q = \pm\ 1 \text{ (circular polarization)} \tag{1.33}$$

$$\Delta j = \pm\ 1 \tag{1.34}$$

$$|j = 0\rangle \not\to |j = 0\rangle \tag{1.35}$$

which are a statement of total angular momentum conservation. A key component of XMCD is eq. 1.33 which states that the excited photoelectron carries away the angular momentum

[†]see derivation in ch. 5 [20]

imparted by the incident photon through a combination of orbital and spin angular momentum. If we consider the $2p \rightarrow 3d$ transition, as is relevant to ch. 3, the two-step model propsed by Stöhr and Wu [17] reveals another important component of XMCD. Firstly, spin-orbit coupling splits the $2p$ core shell into $2p_{1/2}$ (L_2 edge) and $2p_{3/2}$ (L_3 edge), which are separated by $\sim$ 15 eV. The transition matrix can be evaluated at both edges for $q = +1$ and $q = -1$, revealing unequal excitation probabilities which depend both on the spin of the excited photoelectron and the helicity of the x-ray beam. However, if the hole population of the $3d$ valence shell is spin-symmetric, then any asymmetry of the photoelectron spins would not change the observed absorption contrast. Therefore, a second important criterion is a spin-asymmetry in N_H, the holes in the valence shell. Only then, the valence shell serves as an effective spin detector for the dipole-allowed transitions.

1.4.2 Link between magnetism and XMCD

The exchange interaction requires the inclusion of a spin-dependent term to the Hamiltonian. A simple model for the exchange term is given by the Heisenberg Hamiltonian

$$\mathcal{H}_{spin} = -\sum_{i,j} J_{i,j} \left(\mathbf{s}_i \cdot \mathbf{s}_j \right) \tag{1.36}$$

where the sum is taken over all neighboring spin pairs and J is a coupling constant. In the above example of $2p \rightarrow 3d$ photoexcitation, the exchange interaction splits the $3d$ valence shell into spin-up and spin-down subshells, causing the asymmetry in N_H.

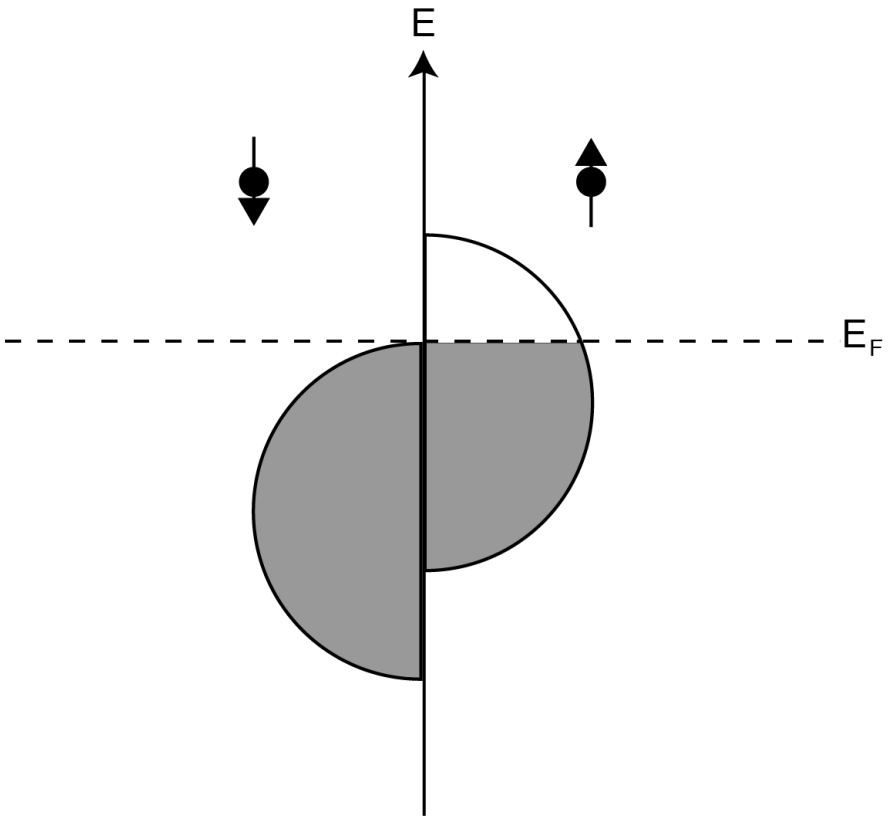

Figure 1.9. Band diagram of a ferromagnetic material according to the Stoner-Wohlfarth model. In this example, the spin-down state is fully occupied and vacancies only exist in the spin-up state.

Exchange splitting can be incorporated into band theory to model ferromagnetism, and a particularly simple example is the Stoner-Wohlfarth (SW) model [21]. In the SW model, the exchange interaction splits the density of states into unequal spin-up and spin-down populations, as seen in fig. 1.9. The magnetic moment is proportional to the difference in occupancy (or number of holes) of spin-up and spin-down states

$$|\mathbf{m}| \propto |N_h^{\uparrow} - N_h^{\downarrow}| \ . \tag{1.37}$$

Now we can see how the XMCD signal relates to the magnetization. A spin-polarizing interaction must exist to observe dichroism, which is precisely the quantum mechanical origin

of ferromagnetism in the SW model. The measured XMCD contrast is proportional to the relative angle between the incident beam polarization direction and the local magnetization of the sample,

$$I_{XMCD} \propto \hat{\mathbf{q}} \cdot \mathbf{m} \ . \tag{1.38}$$

The dichroism is the observed difference in I_{XMCD} when the relative orientation of $\hat{\mathbf{q}}$ and $\mathbf{m}$ is reversed, either by flipping the beam helicity or the magnetization of the sample,

$$\Delta I_{XMCD} = I^{\uparrow\uparrow} - I^{\uparrow\downarrow} \ , \tag{1.39}$$

where the arrows indicate the orientation of the x-ray helicity and the sample magnetization, respectively. XMCD contrast is utilized in the vector ptychography work discussed in ch. 3.

CHAPTER 2

Potential of attosecond coherent diffractive imaging

Attosecond science has been transforming our understanding of electron dynamics in atoms, molecules, and solids. However, to date almost all of the attoscience experiments have been based on spectroscopic measurements because attosecond pulses have intrinsically very broad spectra due to the uncertainty principle and are incompatible with conventional imaging systems. Here we report an important advance towards achieving attosecond coherent diffractive imaging. Using simulated attosecond pulses, we simultaneously reconstruct the spectrum, 17 probes, and 17 spectral images of extended objects from a set of ptychographic diffraction patterns. We further confirm the principle and feasibility of this method by successfully performing a ptychographic coherent diffractive imaging experiment using a light-emitting diode with a broad spectrum. We believe this work clears the way to an unexplored domain of attosecond imaging science, which could have a far-reaching impact across different disciplines.

2.1 Introduction

The first demonstration of attosecond pulses in 2001 opened a new window to probe electron dynamics in atoms and molecules with unprecedented time resolution [22–30]. With the continuing decrease of the temporal pulse duration and the increase of the photon energy range to the x-ray regime [31–34], the potential applications of attoscience could be even broader. However, attoscience experiments have been mostly limited to spectroscopic techniques due to the broad spectrum of the attosecond source [24–26]. For an attosec-

ond pulse, its energy bandwidth (ΔE) and temporal pulse duration (Δt) are fundamentally set by the uncertainty principle ($\Delta E \Delta t \geq h = 2$). For example, the recent experimental demonstration of 53 asec soft x-ray pulses reaches the carbon K-absorption edge (284 eV) with $\Delta E/E \approx 100\%$ [34]. Such broad spectrum pulses cause severe chromatic aberration for any lens-based imaging systems. Chromatic aberration, first discovered by Newton more than 300 years ago [35], is a failure of a lens to focus all colors to the same focal spot due to the change of the refractive index of the lens with the wavelength of light. A classical method to overcome chromatic aberration is the use of achromatic lenses [36]. But this method does not work for the full spectrum of electromagnetic radiation. For example, design and manufacture of achromatic lenses are extremely challenging in the x-ray regime, where lens design is difficult even in the monochromatic case [37]. Here we introduce a novel method based on coherent diffractive imaging (CDI), which can not only eliminate chromatic aberration associated with optical lenses, but also take advantage of the broad spectrum to simultaneously reconstruct the spectrum, probes, and images at 17 different wavelengths. CDI is a lensless imaging or computational microscopy method, where the diffraction patterns of an object are first measured and then directly phased to obtain high-resolution images [38]. Since the first experimental demonstration in 1999 [5], various forms of CDI such as plane-wave CDI, ptychography, and Bragg CDI have been developed and applied to a broad range of samples in the physical and biological sciences using synchrotron radiation, x-ray free electron lasers, high harmonic generation, optical lasers, and electrons [5, 9, 38–49]. With advanced computational algorithms, broadband CDI has also been developed to deal with the low temporal coherence of the illumination source [50–54]. Ptychography, a powerful scanning CDI method, is particularly suitable for broadband imaging, which collects a series of diffraction patterns by scanning a spatially confined probe across an extended sample [9, 49]. By partially overlapping the probe between adjacent scan positions, advanced algorithms can be used to reconstruct both the probe and the complex exit wave of the sample [41]. More recently, multimode and multiplex ptychographic methods have been developed to deal with

broadband data [55–60]. In this Letter, we make an important advance to merge CDI with attosecond science, allowing the simultaneous reconstruction of the spectrum, probes, and images at multiple wavelengths.

2.2 Methods

For attosecond light with a broad bandwidth, its diffraction pattern is composed of an incoherent sum of diffracted intensity from all wavelengths, producing a blurred pattern [Fig. 2.1(a)]. Phase retrieval of such blurred diffraction patterns is a challenging process as they are mixed with both coherent and incoherent scattering. Here we develop an advanced algorithm, called Spectrum, Probe, and Image REconstruction (SPIRE), to simultaneously reconstruct the spectrum, probes, and spectral images at multiple wavelengths. SPIRE requires the collection of a set of diffraction patterns by performing a 2D scan of a confined probe across a sample, where the probe at each scan position is overlapped with its adjacent ones [Fig. 2.1(a)]. To meet the criterion that the number of the equations of measured intensity points is more than the number of unknown variables of the sample [3], a large overlap between adjacent scan positions is needed. The algorithm then iterates between real and reciprocal space [Fig. 2.1(b)]. In real space, we introduce the concept of real and ghost modes, where the real modes reconstruct the spectrum, probes, and spectral images, and the ghost modes accommodate unwanted information such as errors and noise (Supplemental material). The exit wave of the real and ghost modes at different wavelengths is obtained by multiplying probes by the object functions of the sample. Taking the Fourier transform of the exit wave generates the diffracted wave of real and ghost modes. An updated diffracted wave is obtained by constraining it to the diffraction patterns. Applying the inverse Fourier transform to the diffracted wave produces a new exit wave, which is used to create the next-iteration probes and object functions of the real and ghost modes. In each iteration, we also enforce the probe replacement constraint to the real modes.

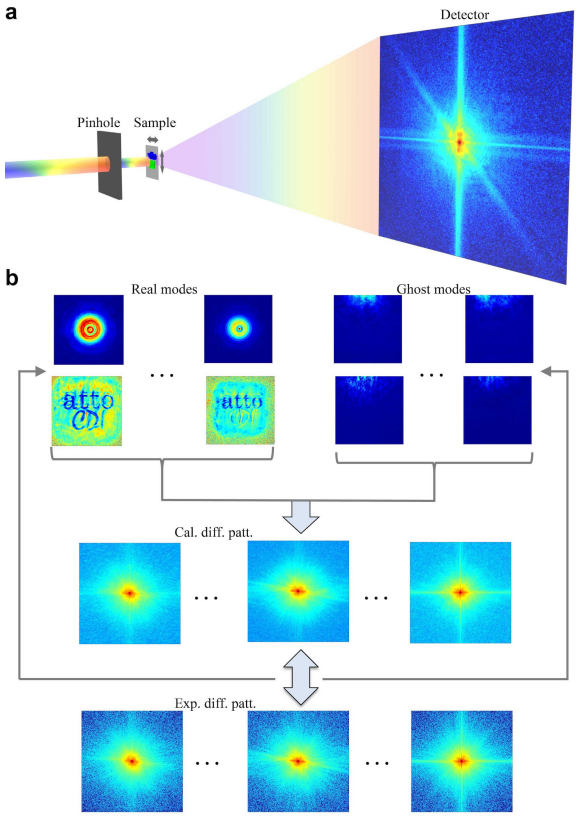

Figure 2.1. Schematic of the broadband CDI data acquisition and SPIRE algorithm. (a) A probe with a very broad spectrum is defined by a pinhole and scanned across a sample. At each scan position, a diffraction pattern is recorded by a detector. (b) SPIRE iterates between real and reciprocal space. In real space, the exit wave of the real and ghost modes at different wavelengths is obtained by multiplying probes by the object functions of the sample. In reciprocal space, the calculated diffraction patterns at different scan positions are compared with the corresponding experimental diffraction patterns, which is used to update the real and ghost modes of the next iteration. A detailed description of SPIRE is provided in the Supplemental material. *(Figure reprinted from [61])*

The best probe is identified among all the wavelengths and is propagated back to construct the probes of other wavelengths. By incorporating the real, ghost modes, and probe replacement, SPIRE enables us to simultaneously reconstruct the spectrum, probes, and spectral images from a very broadband illumination. The algorithm is robust as it is not sensitive to the initial input and converges after several hundreds of iterations.

To validate the SPIRE algorithm, we first performed numerical simulations using attosecond pulses with a spectrum ranging from 4.1 to 12.4 nm [34]. The probe was confined by a $3-\mu$m-diameter pinhole that was placed 100 μm upstream of the sample and Fresnel propagated to the sample plane. Two samples were used in the simulations. The first is a resolution pattern, composed of 200-nm-thick aluminum structure with bar widths ranging from 30 nm to 1.2 μm. The second sample is a letter pattern with "atto" made of 200-nm-thick aluminum and "CDI" of 200-nm-thick boron. Boron was chosen because its K-absorption edge (6.6 nm) is within the simulated spectrum, providing a contrast difference to assess the reconstruction quality of the spectrum and spectral images. Each sample was scanned in a randomly perturbed 2D raster grid scheme with a 94% overlap between adjacent scan positions. The resolution pattern dataset consists of 1456 scan points and the letter pattern dataset consists of 676 scan points. A flux of 1×10^7 photons per scan position was used in the simulation and Poisson noise was added to the diffraction intensity. Each diffraction pattern was collected by a detector positioned 10 cm downstream of the sample to satisfy the oversampling requirement for all wavelengths [3]. The quantum efficiency of the detector as a function of the spectrum was taken into account in each diffraction pattern. Figures 2.2(a) and 2.2(b) show a representative diffraction pattern from the resolution and letter pattern, respectively. The most noticeable feature of these broadband diffraction patterns is the absence of strong speckles that are presented in monochromatic diffraction patterns.

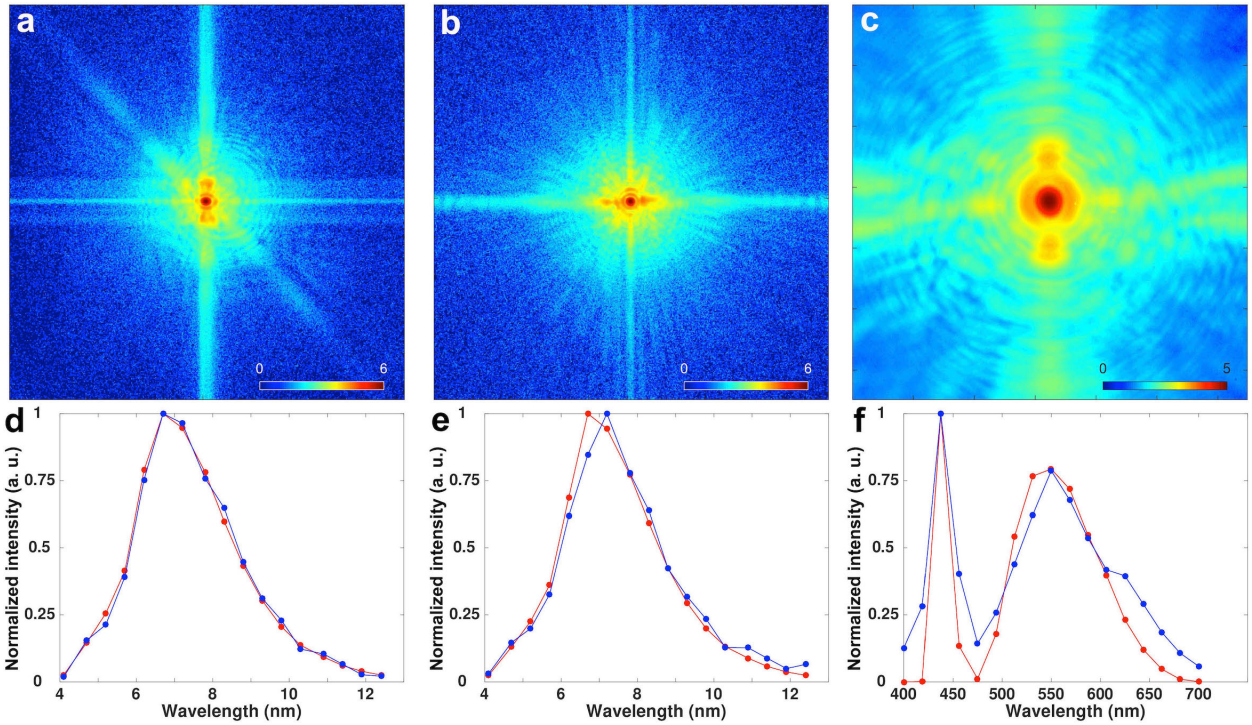

Figure 2.2. Representative diffraction patterns and reconstructed spectra by SPIRE. (a) and (b) Representative diffraction patterns measured from a resolution and letter pattern, respectively, using simulated attosecond pulses. (c) Representative diffraction pattern of a test pattern using an LED. (d)–(f) Reconstructed spectra (in blue) of the resolution and letter pattern with simulated attosecond pulses and of the test pattern with the LED, respectively, where the true spectra are in red. The true spectrum of the LED in (f) was measured by a spectrometer. *(Figure reprinted from [61])*

2.3 Results & discussion

From the diffraction patterns, we used the SPIRE algorithm to reconstruct the spectrum, probes, and spectral images. All reconstructions consist of two runs of 250 iterations each. In the first run, the initial guesses of the probes and spectral images were binary masks and random arrays, respectively. The second run was initialized with new random arrays of the images while retaining the reconstructed probes from the first run. In the second run, only the images were allowed to update while the probes are fixed. In all reconstructions, we chose 17 probes and 17 spectral images that span the simulated spectrum in equal wavelength intervals. The number of probes and spectral images was heuristically chosen in a manner to reconstruct the spectrum with high accuracy while also minimizing the crosstalk between adjacent images. Figures 2.2(d)–2.2(e) show the reconstructed spectra (blue) of the resolution and letter pattern, which are in good agreement with the true ones (red). In comparison, a state-of-the-art broadband algorithm known as ptychographic information multiplexing (PIM) [56] failed to reconstruct the spectra in both cases (Supplemental material, Fig. 2.S1).

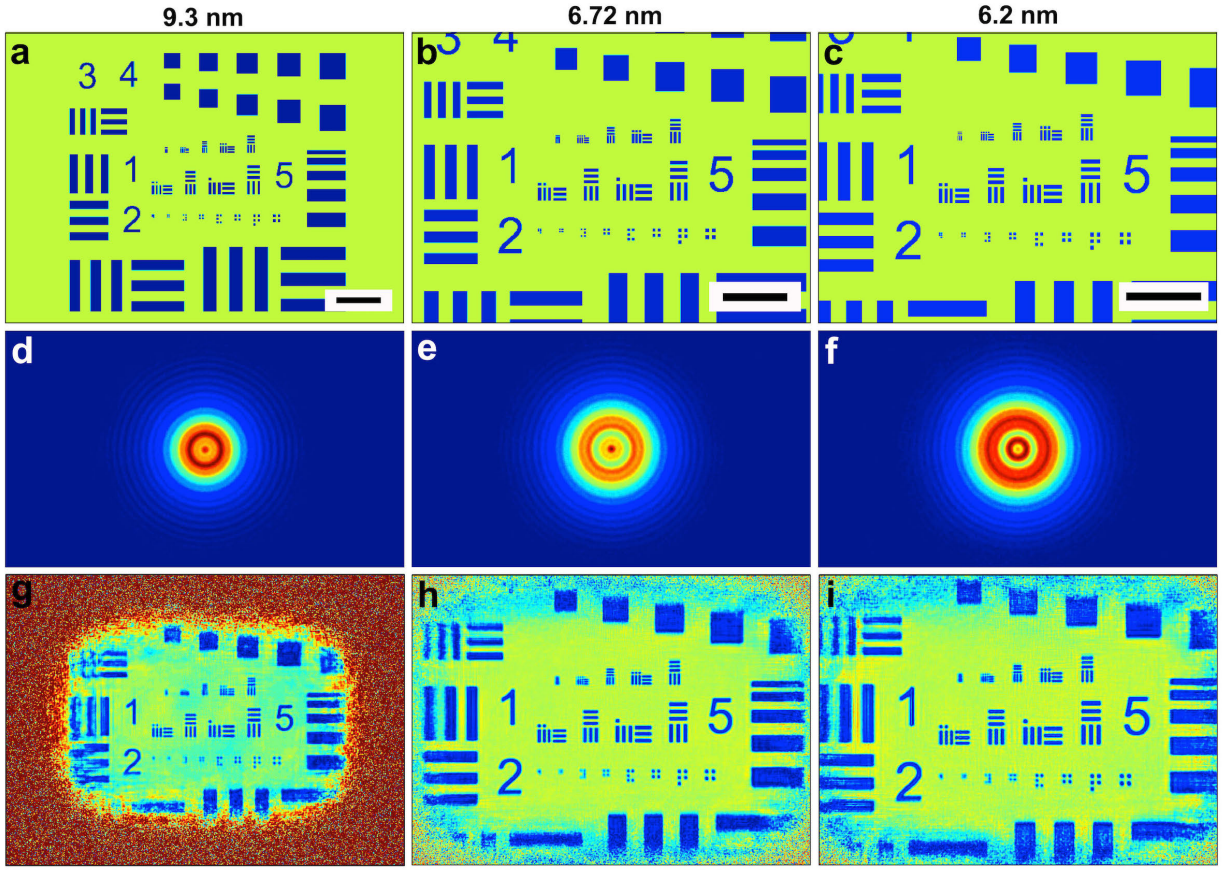

Figure 2.3. Probe and spectral image reconstructions of a resolution pattern with simulated attosecond pulses. (a)–(c) The structure of the resolution pattern at 9.3, 6.72, and 6.2 nm, respectively. (d)–(i) Three representative probes and spectral images at different wavelengths reconstructed by SPIRE, respectively, where the spatial resolution is increased with the decrease of the wavelength. The full 17 probes and 17 spectral images are shown in Supplemental material, Figs. 2.S2(a) and 2.S3(a), respectively. Scale bars, 2 μm. *(Figure reprinted from [61])*

Figure 2.3 shows the SPIRE reconstruction of the probes and spectral images of the resolution pattern at three representative wavelengths (9.3, 6.72, 6.2 nm), in which the spatial resolution is increased with the decrease of the wavelength. The full reconstructions of 17 probes and 17 spectral images are shown in the Supplemental material, Figs. 2.S2(a) and 2.S3(a), respectively. SPIRE faithfully reconstructed all the probes and spectral images except the first and last image due to the low incident flux at these two wavelengths [Fig 2.S3(a), frame 1 and 17]. Figure 2.4 and Figs. 2.S4(a) and 2.S5(a) in the Supplemental material show the reconstructed probes and spectral images of the letter pattern. While the absorption of aluminum is relatively flat across the spectrum, the K edge of boron at 6.6 nm causes a jump in the absorption contrast of the "CDI" letters (Fig. 2.4). In comparison, PIM failed to reconstruct several probes and spectral images of both the resolution and letter patterns [Supplemental material, Figs. 2.S2(b), 2.S3(b), 2.S4(b), and 2.S5(b)]. To account for the spectral instability of attosecond pulses, we conducted another simulation with a shot-to-shot spectral fluctuation of 10%. With all the other parameters kept the same, SPIRE successfully reconstructed the average spectrum, probes, and spectral images at 17 different wavelengths (Supplemental material, Figs. 2.S6 and 2.S7).

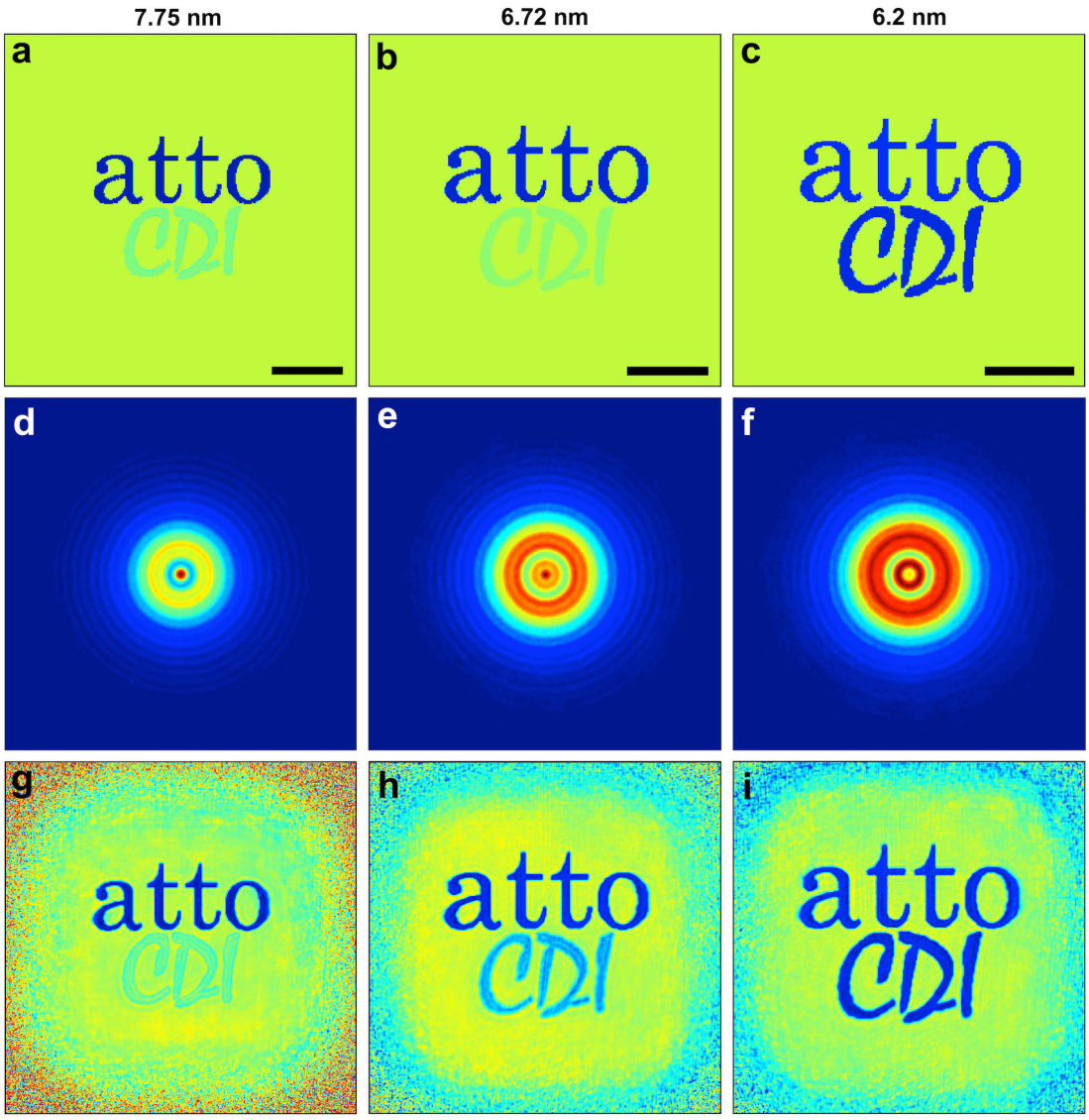

Figure 2.4. Probe and spectral image reconstructions of a letter pattern with simulated attosecond pulses. (a)–(c) Absorption contrast images of the letter pattern at 7.75, 6.72, and 6.2 nm, respectively, where the K edge of boron is at 6.6 nm. (d)–(i) Three representative probes and spectral images at different wavelengths reconstructed by SPIRE, respectively, where the image contrast of the "CDI" letters changes across the absorption edge. The full 17 probes and 17 spectral images are shown in the Supplemental material, Figs. 2.S4(a) and 2.S5(a), respectively. Scale bars, 2 μm. *(Figure reprinted from [61])*

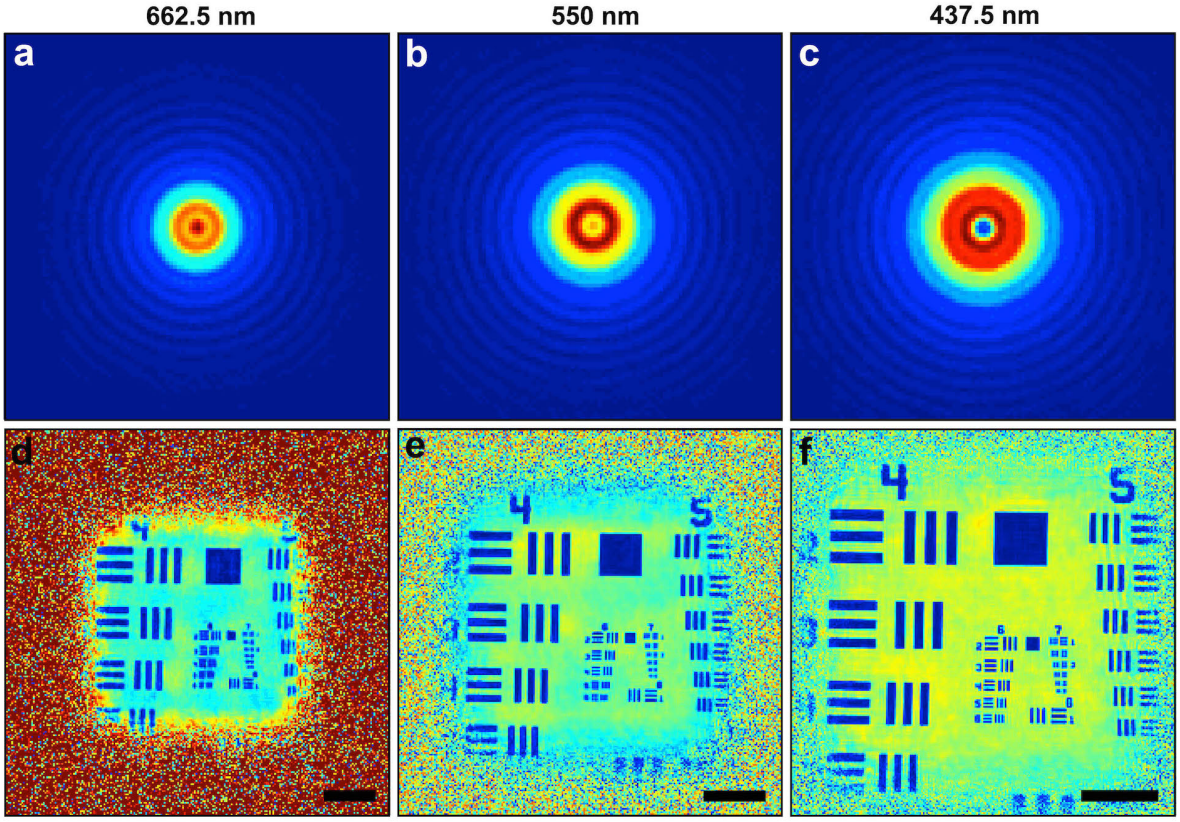

Figure 2.5. Probe and spectral image reconstructions of a test pattern from broadband LED diffraction patterns. (a)–(f) Three representative probes and spectral images reconstructed by SPIRE at 662.5, 550, and 437.5 nm, respectively. The full 17 probes and 17 spectral images are shown in Supplemental material, Fig. 2.S8. Scale bars, 200 μm *(Figure reprinted from [61])*

Next, we performed a broadband light-emitting diode (LED) experiment to validate the method. A collimated white LED was used to illuminate a test pattern with a 200 μm pinhole placed approximately 6 mm upstream of the sample to confine the probe. A CCD camera from Princeton Instruments was placed 26 cm downstream of the sample to collect diffraction patterns while fulfilling the oversampling requirement for all wavelengths of the LED [3]. A field of view approximately 600 $\times$ 600 μm was scanned using a 2D raster grid consisting of 950 points with a 94% overlap between adjacent probe positions. A small random offset was applied to the scan positions to avoid gridding artifacts in the reconstructions. Three exposures of different duration were collected at each scan position and merged to improve the dynamic range of the diffraction patterns. Diffraction patterns were cropped to be square and binned by a factor of 2 in each dimension to increase the signal-to-noise ratio and reduce the computation time. After two runs of 250 iterations each, we reconstructed the spectrum, 17 probes, and 17 spectral images from the diffraction patterns. The reconstructed spectrum agrees with that measured by a spectrometer [Fig. 2.2(f)]. Figure 2.5 shows three representative probes and spectral images at 662.5, 550, and 437.5 nm. All 17 probes and images are shown in the Supplemental material, Fig. 2.S8. The successful reconstruction of the spectrum, probes, and spectral images from the experimental diffraction patterns further corroborated the feasibility of the method.

2.4 Conclusion

In conclusion, we have developed a powerful algorithm (SPIRE) by incorporating new constraints—real, ghost modes, and probe replacement. Our simulation and experimental results demonstrate that SPIRE can simultaneously reconstruct the spectrum, probes, and spectral images at 17 wavelengths from very broadband light sources with $\Delta E/E \approx 100\%$, which (to our knowledge) cannot currently be accomplished by any other broadband CDI algorithms [50–60]. Looking forward, we anticipate that SPIRE is in principle applicable to

both coherent photon and electron sources with broad spectra, such as synchrotron radiation pink beams and HHG, allowing chemically specific imaging without the need of monochromatic optics. By avoiding the use of focusing optics, the spatial resolution of this method is limited only by the spatial frequency of the diffracted intensity. Furthermore, by harnessing all the flux from a broadband light source, this method can significantly reduce the data acquisition time in performing spectroptychography experiments, whereas the conventional method requires serial repetition of ptychographic scans as a function of the energy. Finally, this work potentially unifies two important fields—attosecond science and CDI—into a single frame. As the spectrum of the current state-of-the-art attosecond sources extends to the x-ray regime [34, 62], the ability to simultaneously reconstruct the spectrum, probes, and images at multiple wavelengths could find application ranging from visualizing attosecond electron dynamics to imaging materials and biological samples at the nanometer scale with attosecond x-ray pulses.

Acknowledgements

We thank Z. Chang, P.B. Corkum, M.M. Murnane, H.C. Kapteyn, Y. Wu, X. Ren, and J. Li for stimulating discussions. This work was primarily supported by STROBE: A National Science Foundation Science & Technology Center under Grant No. DMR 1548924. We also acknowledge partial support by the US Department of Energy, Office of Science, Basic Energy Sciences, Division of Materials Sciences and Engineering under Award No. DE-SC0010378.

2.5 Supplemental material

2.5.1 The SPIRE algorithm

SPIRE iterates between real and reciprocal space. The i^{th} iteration exit wave of the real and ghost modes, $\psi^i_{\lambda,j,e}(\vec{r})$ and $\psi^i_{\lambda,j,g}(\vec{r})$, is calculated by

$$\begin{pmatrix}\psi^i_{\lambda,j,e}(\vec{r})\\ \psi^i_{\lambda,j,g}(\vec{r})\end{pmatrix} = \begin{pmatrix}P^i_{\lambda,e}(\vec{r})\cdot O^i_{\lambda,j,e}(\vec{r})\\ P^i_{\lambda,g}(\vec{r})\cdot O^i_{\lambda,j,g}(T\vec{r})\end{pmatrix}, \tag{2.1}$$

where i and j index the i^{th} iteration and j^{th} scan position, $P^i_{\lambda,e}(\vec{r})$ and $P^i_{\lambda,g}(\vec{r})$ are the probes, $O^i_{\lambda,j,e}(\vec{r})$ and $O^i_{\lambda,j,g}(T\vec{r})$ are the object function of the sample with the subscripts e and g representing the real and ghost modes, respectively, and T is a transformation matrix. After testing several different types of the transformation matrix, we found a $2D$ coordinate reflection matrix works the best in this work. By taking the Fourier transform ($\mathcal{F}$) of the exit wave, we obtain the diffracted wave of the real and ghost modes,

$$\begin{pmatrix}\Psi^i_{\lambda,j,e}(\vec{k})\\ \Psi^i_{\lambda,j,g}(\vec{k})\end{pmatrix} = \mathcal{F}\begin{pmatrix}\psi^i_{\lambda,j,e}(\vec{r})\\ \psi^i_{\lambda,j,g}(\vec{r})\end{pmatrix}. \tag{2.2}$$

The diffracted wave is updated by being constrained to the measured intensity, $I_j(\vec{k})$,

$$\begin{pmatrix}\Psi'^i_{\lambda,j,e}(\vec{k})\\ \Psi'^i_{\lambda,j,g}(\vec{k})\end{pmatrix} = \frac{\sqrt{I_j(\vec{k})}}{\sum_{\lambda=1}^{M}[|\Psi^i_{\lambda,j,e}(\vec{k})|^2+|\Psi^i_{\lambda,j,g}(\vec{k})|^2]}\begin{pmatrix}\Psi^i_{\lambda,j,e}(\vec{k})\\ \Psi^i_{\lambda,j,g}(\vec{k})\end{pmatrix}. \tag{2.3}$$

The corresponding exit wave of the real and ghost modes is calculated by

$$\begin{pmatrix}\psi'^i_{\lambda,j,e}(\vec{r})\\ \psi'^i_{\lambda,j,g}(\vec{r})\end{pmatrix} = \mathcal{F}^{-1}\begin{pmatrix}\Psi'^i_{\lambda,j,e}(\vec{k})\\ \Psi'^i_{\lambda,j,g}(\vec{k})\end{pmatrix}, \tag{2.4}$$

where $\mathcal{F}^{-1}$ is the inverse Fourier transform. The probe and object function of the $(i+1)^{th}$ iteration are updated by [11],

$$P'^{i+1}_{\lambda,e}(\vec{r}) = P^i_{\lambda,e}(\vec{r}) + \beta_1\frac{O^{*i}_{\lambda,j,e}(\vec{r})}{|O^i_{\lambda,j,e}(\vec{r})|^2_{max}}[\psi'^i_{\lambda,j,e}(\vec{r})-\psi^i_{\lambda,j,e}(\vec{r})] \tag{2.5}$$

$$O^{i+1}_{\lambda,e}(\vec{r}) = O^i_{\lambda,e}(\vec{r}) + \beta_1\frac{P^{*i}_{\lambda,j,e}(\vec{r})}{|P^i_{\lambda,j,e}(\vec{r})|^2_{max}}[\psi'^i_{\lambda,j,e}(\vec{r})-\psi^i_{\lambda,j,e}(\vec{r})] \tag{2.6}$$

where β_1 is set to 0.9. Equations 2.5 and 2.6 are also used to calculate the $(i+1)^{th}$ iteration probe and object function of the ghost modes by replacing the subscript e with g.

Next we implement the probe replacement constraint for the real modes, which takes into account the wavelength-dependent propagation of the probe. In the i^{th} iteration, we first locate the best probe, $P'^{i+1}_{\lambda^*,e}(\vec{r})$, among all the reconstructed probes, where λ^* represents the wavelength of the best probe. This probe, which corresponds to the highest intensity mode, is Fresnel propagated back to the pinhole plane. The best probe in the pinhole plane is then Fresnel propagated to the sample plane at other wavelengths (λ'), defined as $P''^{i+1}_{\lambda',e}(\vec{r})$. The $(i+1)^{th}$ iteration probe is further updated by

$$P^{i+1}_{\lambda,e}(\vec{r}) = \begin{cases} P'^{i+1}_{\lambda',e}(\vec{r}) + \beta_2(P''^{i+1}_{\lambda',e}(\vec{r}) - P'^{i+1}_{\lambda',e}(\vec{r})) & \lambda = \lambda' \\ P'^{i+1}_{\lambda^*,e}(\vec{r}) & \lambda = \lambda^* \end{cases}, \tag{2.7}$$

where β_2 is set to 0.1.

2.5.2 Spectrum recovery

We recover the spectrum from the exit wave of the real modes,

$$\psi_{\lambda,j,e}(\vec{r}) = O_{\lambda,j,e}(\vec{r})P_{\lambda,e}(\vec{r}) = [\frac{1}{c_\lambda}O_{\lambda,j,e}(\vec{r})][c_\lambda P_{\lambda,e}(\vec{r})] \tag{2.8}$$

where $\psi_{\lambda,j,e}(\vec{r})$ and $O_{\lambda,j,e}(\vec{r})$ are reconstructed exit wave and object function of the sample, $P_{\lambda,e}(\vec{r})$ is the reconstructed probe at wavelength λ and c_λ is a wavelength-dependent constant. As the exit wave is constrained to the measured intensity by Eq. 2.3, it can be uniquely reconstructed by SPIRE, but the probe and object function are not unique up to a multiplicative constant (Eq. 2.8). Thus we use the reconstructed exit wave instead of the probe to recover the spectrum,

$$S_{\lambda,j} = \sum_{x,y} |O_{\lambda,j,e}(x,y)P_{\lambda,e}(x,y)|^2 \tag{2.9}$$

where $S_{\lambda,j}$ is the spectrum of the j^{th} scan position and $\vec{r} = (x,y)$. By choosing an empty region in the sample and averaging the spectra of all the scan positions in the region, we

obtain the final recovered spectrum, S_λ, which removes the effect of object function on the spectrum recovery. By incorporating the ghost mode and probe replacement constraint, SPIRE reconstructs more accurate probes across the entire spectrum than other algorithms [55–60], which leads to more accurate spectrum recovery.

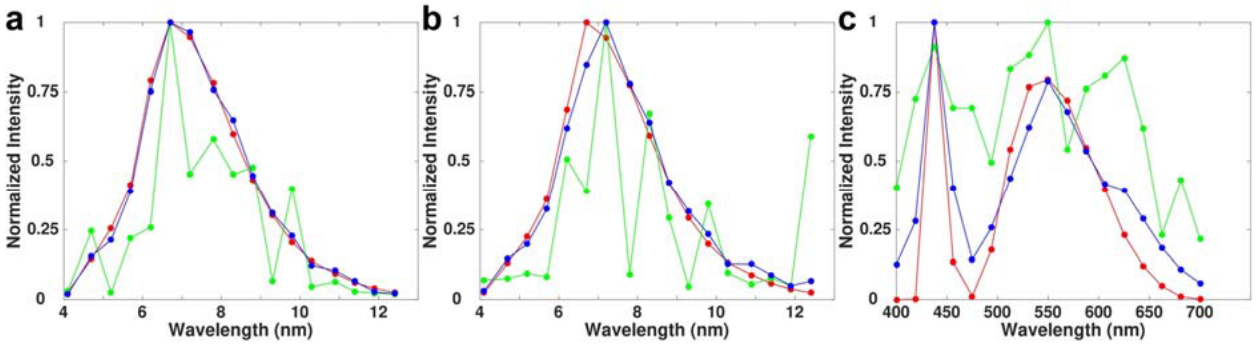

Figure 2.S1. Reconstructed spectra of the resolution (a) and letter pattern (b) with simulated attosecond pulses and of the test pattern with a LED experiment (c). The true spectrum is in red and the spectra reconstructed by PIM and SPIRE are in blue and green, respectively. The true spectrum of the LED was measured by a spectrometer. *(Figure reprinted from [61])*

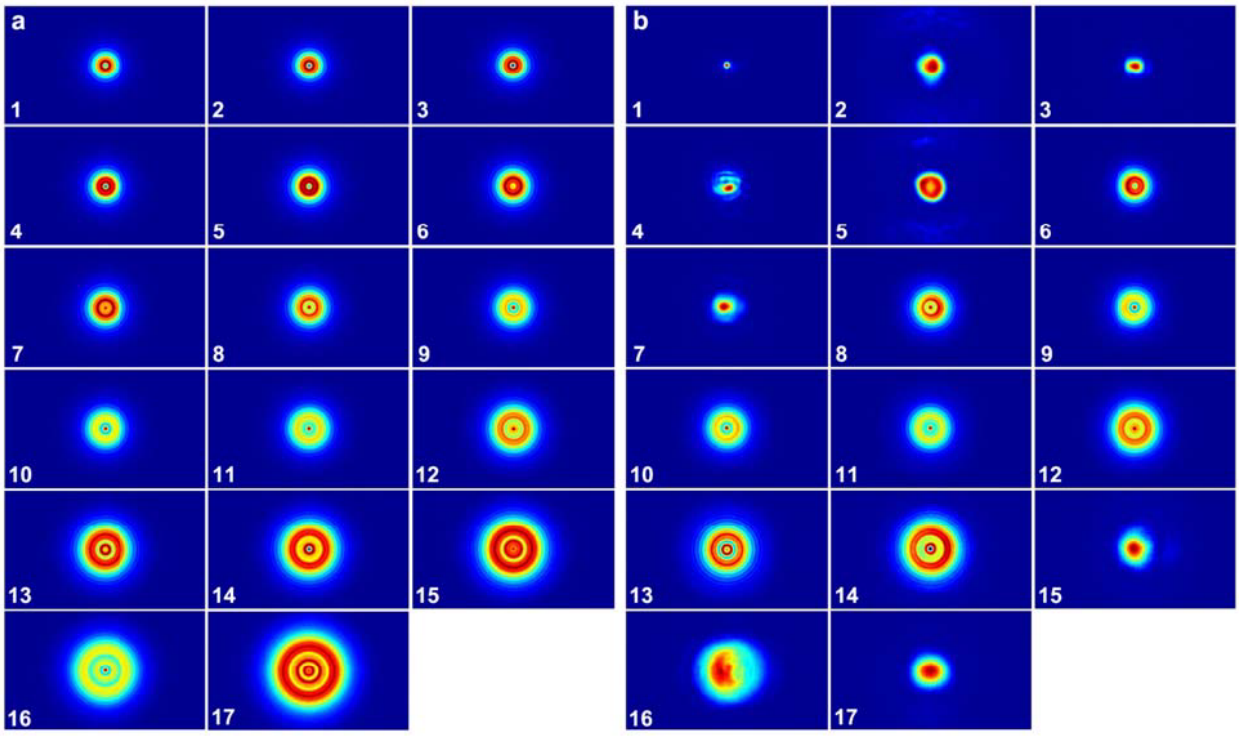

Figure 2.S2. SPIRE and PIM reconstruction of the probes for the resolution pattern using simulated attosecond pulses. (a) 17 probes reconstructed by SPIRE that span the simulated spectrum in equal wavelength intervals, with good recovery across the whole spectrum. (b) 17 probes reconstructed by PIM, exhibiting artifacts in the reconstruction at several wavelengths. *(Figure reprinted from [61])*

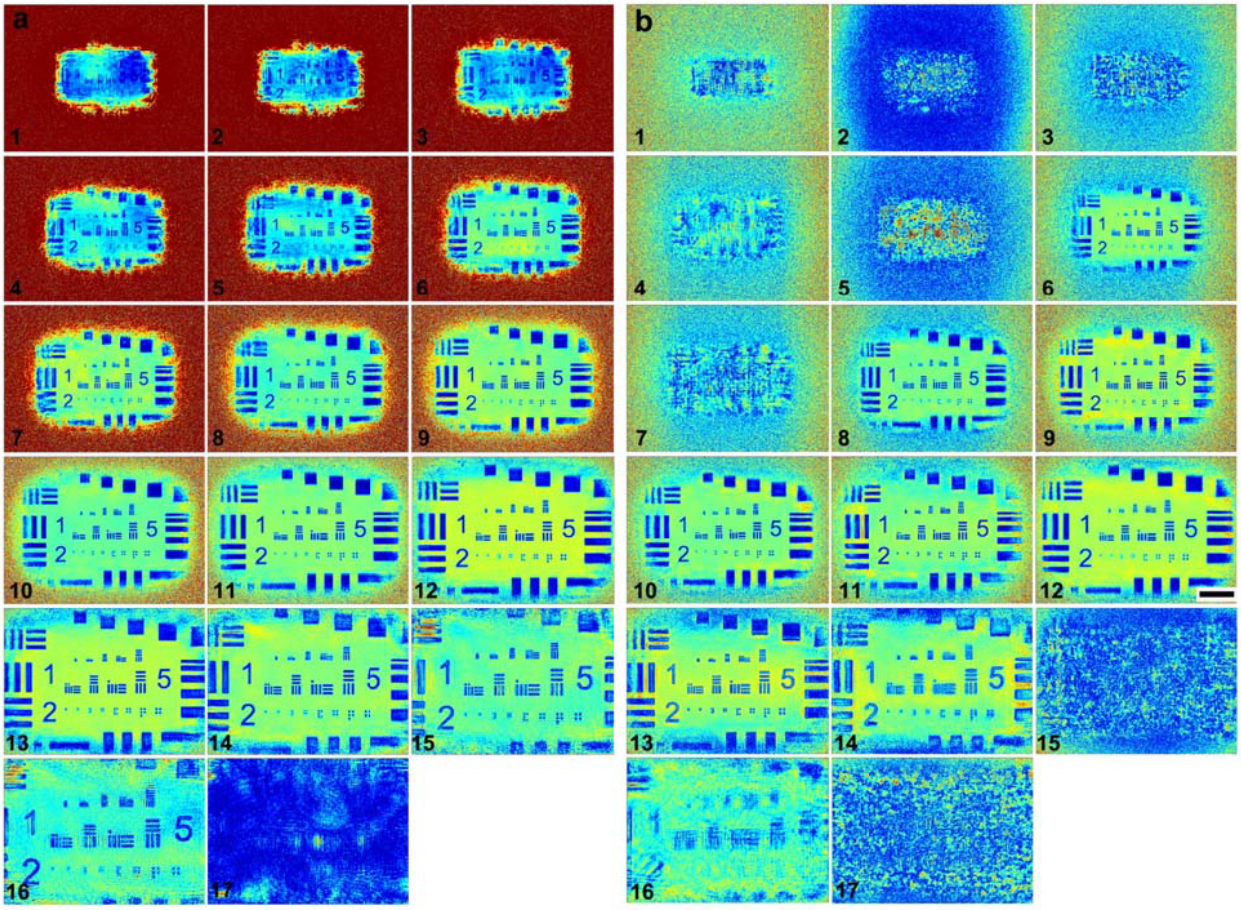

Figure 2.S3. SPIRE and PIM reconstruction of the spectral images of the resolution pattern using simulated attosecond pulses. (a) 17 spectral images reconstructed by SPIRE. The first and last images were not successfully reconstructed due to the low incident flux at these two wavelengths. (b) 17 spectral images reconstructed by PIM, where the poorly reconstructed images are innately linked to the poorly reconstructed probes (Supplemental Fig. 2.S2b). Scale bar, 2 μm.*(Figure reprinted from [61])*

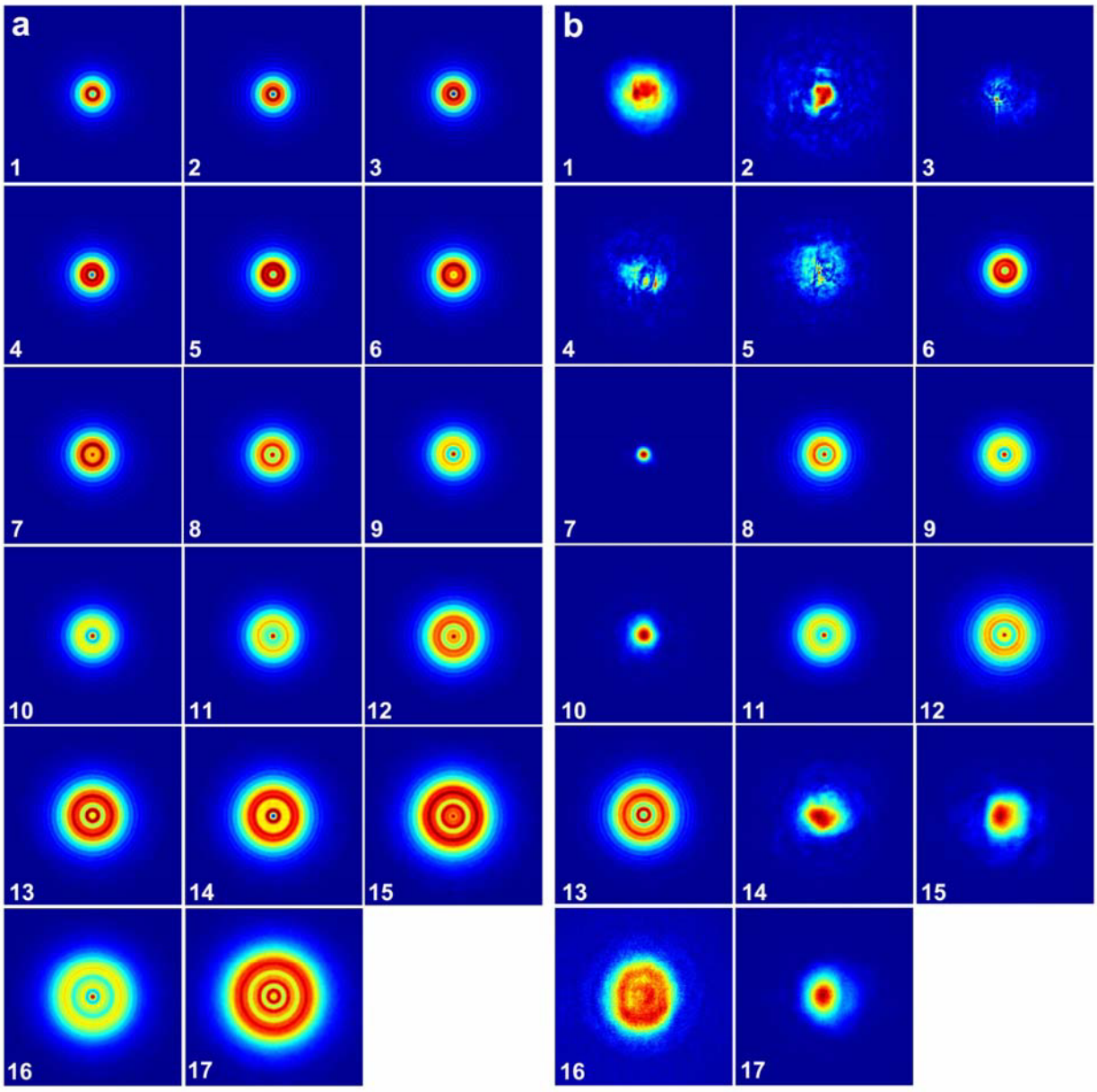

Figure 2.S4. SPIRE and PIM reconstruction of the probes for the letter pattern using simulated attosecond pulses. (a) 17 probes reconstructed by SPIRE that span the simulated spectrum in equal wavelength intervals. (b) 17 probes reconstructed by PIM, exhibiting significant artifacts in the reconstruction. *(Figure reprinted from [61])*

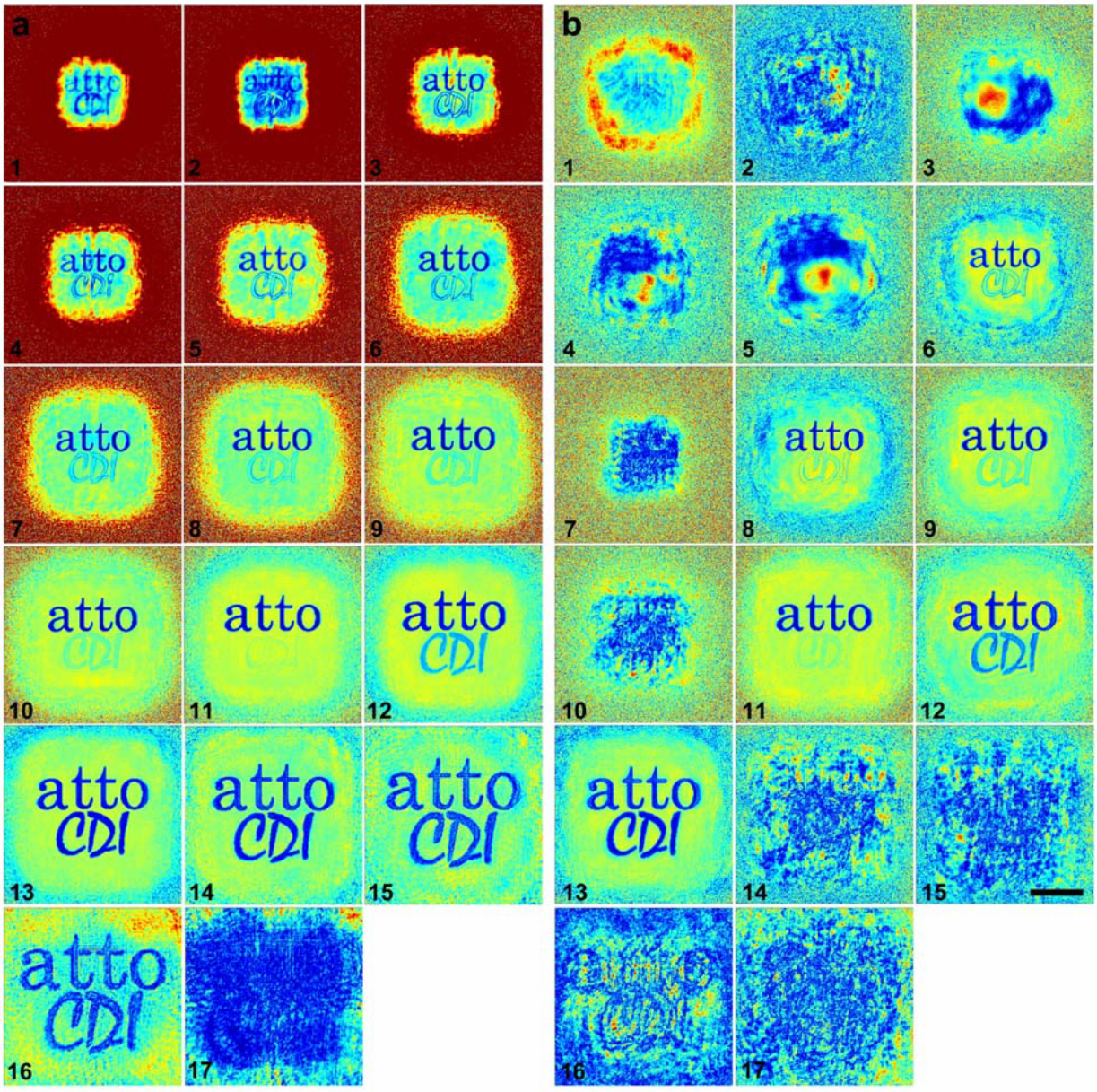

Figure 2.S5. SPIRE and PIM reconstruction of the spectral images of the letter pattern using simulated attosecond pulses. (a) 17 spectral images reconstructed by SPIRE, where the boron K-absorption edge is at 6.6 nm (between modes 12 and 13). (b) 17 spectral images reconstructed by PIM, in which 10 out of 17 modes were poorly reconstructed. Scale bar, 2 μm. *(Figure reprinted from [61])*

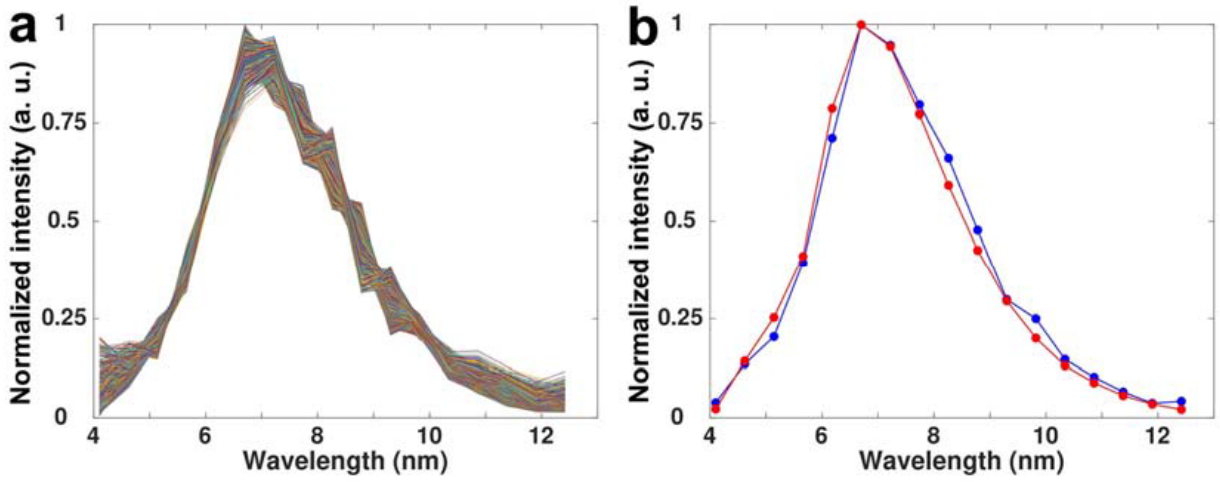

Figure 2.S6. SPIRE reconstruction of the spectra with a shot-to-shot spectral fluctuation of 10%. (a) Reconstructed spectra from all the scan positions for the resolution pattern. The fluctuation of the reconstructed spectra is consistent with that used to calculate the ptychographic diffraction patterns. (b) Reconstructed spectrum (blue) by averaging all the spectra in (a), which is in good agreement with the average true spectrum (red). *(Figure reprinted from [61])*

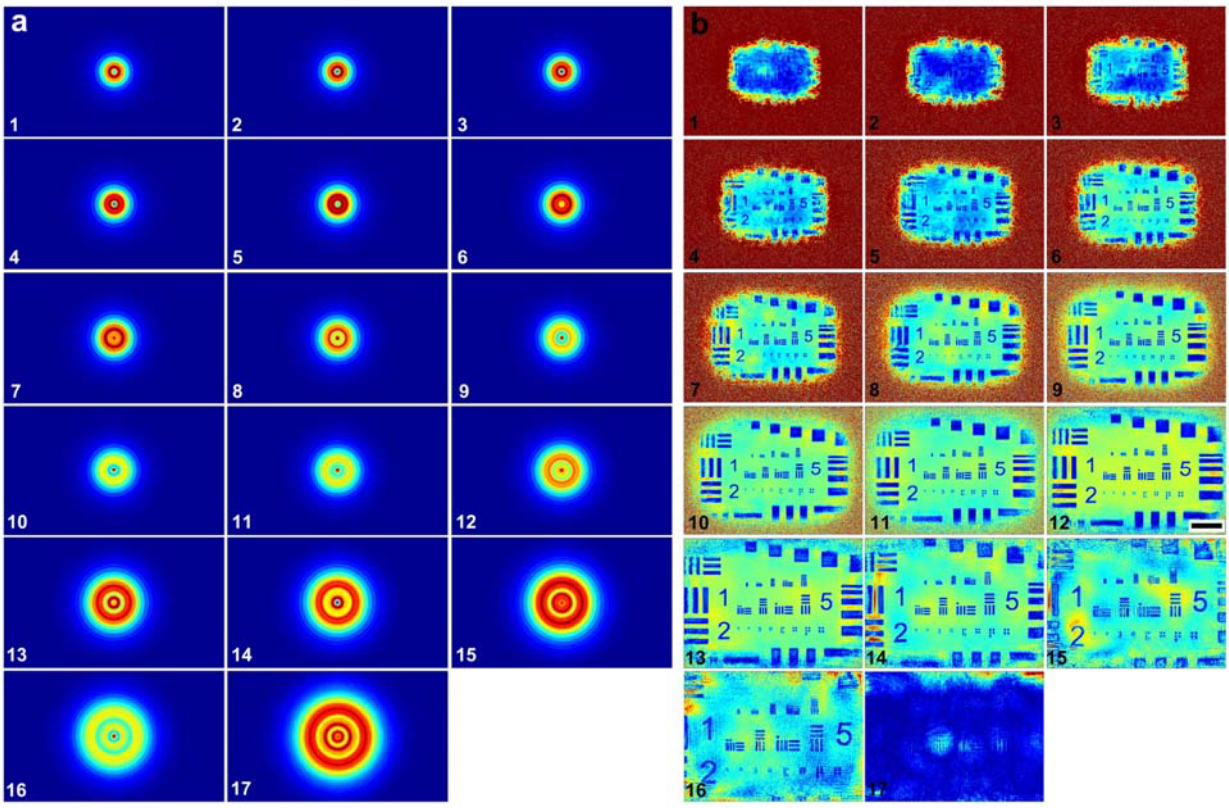

Figure 2.S7. SPIRE probe and spectral image reconstruction of the resolution pattern with a shot-to-shot spectral fluctuation of 10%. The reconstructed probes (a) and spectral images (b) at 17 different wavelengths. *(Figure reprinted from [61])*

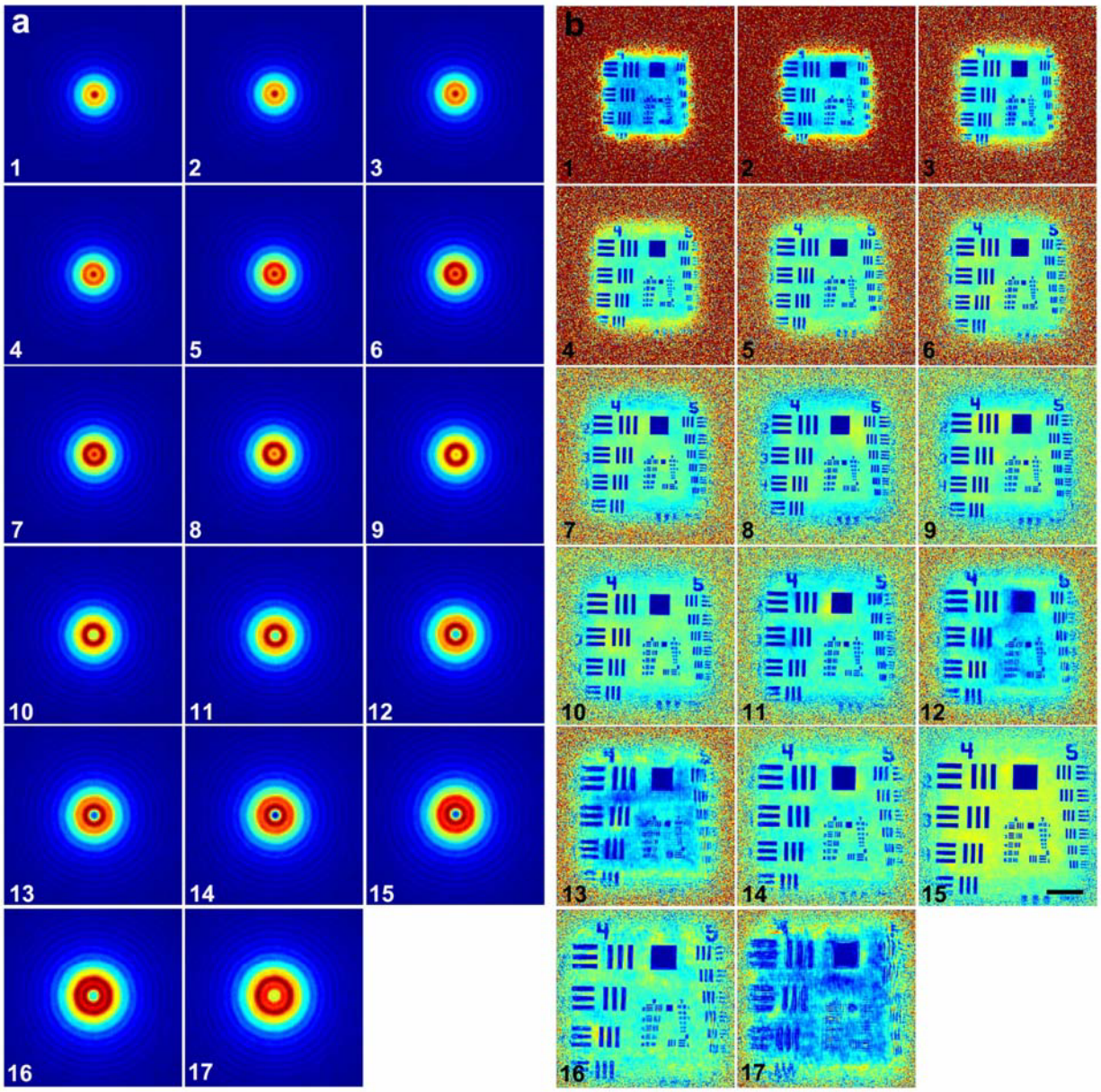

Figure 2.S8. SPIRE reconstruction of 17 probes (a) and spectral images (b) of a test pattern from a broadband LED experiment. Scale bar, 200 μm. *(Figure reprinted from [61])*

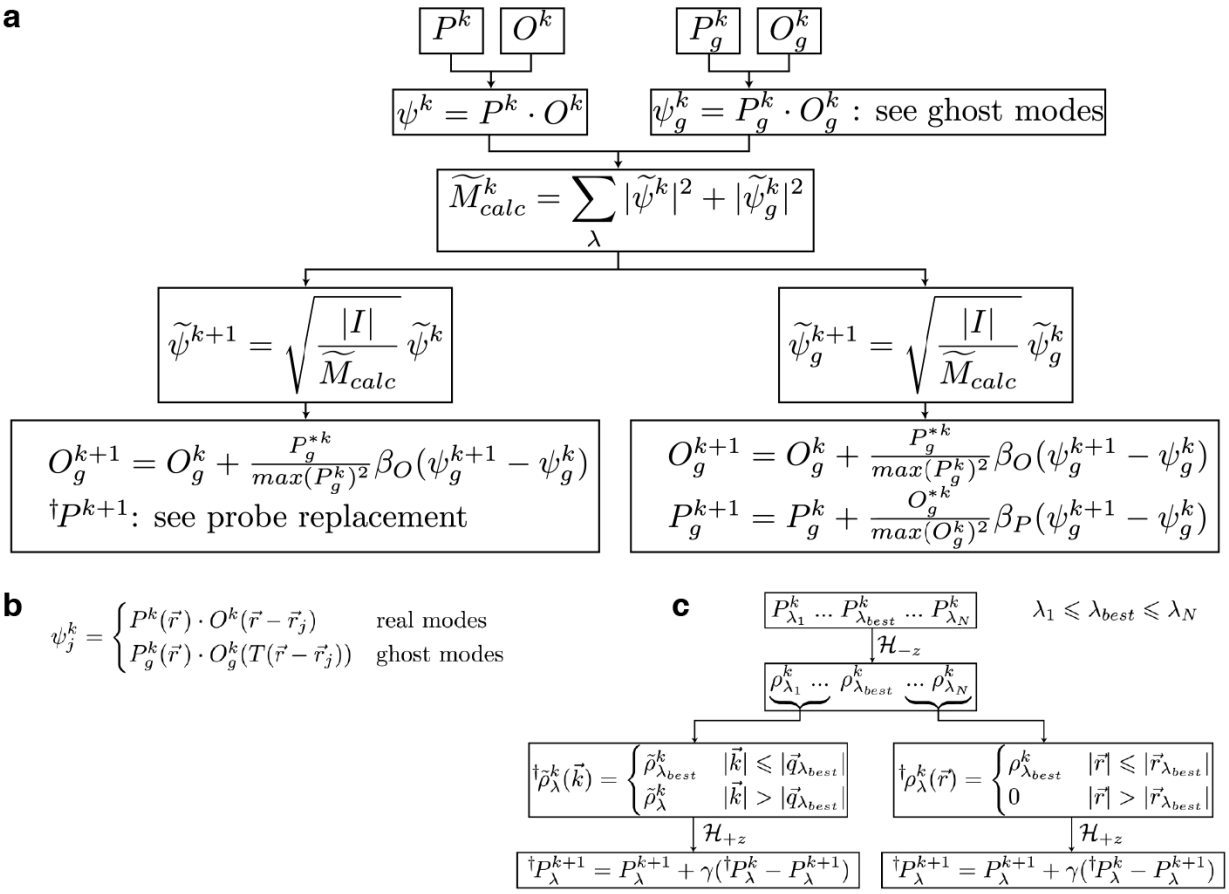

Figure 2.S9. (a) A flowchart illustrating one micro-iteration of SPIRE. For clarity, λ indexing is implied but omitted for all variables except M and I. Tildes are used to mark Fourier space variables. (b) The relationship between real modes and ghost modes, which differ by the transformation matrix T applied to the scan coordinates. (c) The probe replacement constraint. The Fresnel propagator between the sample and pinhole plane is given by $\mathcal{H}$ and γ is a constant to modulate the step size of the update.

CHAPTER 3

Direct observation of geometry-confined 3D topological spin textures

Topological magnetic defects are energetically stable spin configurations categorized by broken symmetry in parameter space. Vortices and skyrmions are well-known examples of two-dimensional textures that have been investigated for spintronic applications. However, experimental evidence of three-dimensional textures remains largely indirect because of the extremely small volumes occupied by these textures, despite theoretical predictions of their existence. Here, we develop soft x-ray vector ptychography and directly image the magnetization vector field of a three-dimensional frustrated metalattice at a resolution of 10 nm, similar to the exchange length of transition metals. Further, we employ homotopy theory analysis on the experimental data and quantify the topological charge of hedgehog defects. The imaging technique developed here opens the possibility to study three-dimensional defects in a variety of magnetic materials on their natural length scale.

3.1 Introduction

Since the first experimental demonstration of coherent diffractive imaging (CDI) in 1999, lensless x-ray imaging has undergone a rapid evolution to allow for the study of non-crystalline materials on the nanoscale across a variety of disciplines [5, 38, 63]. Ptychography has been demonstrated as a powerful CDI method to recover the 3-D structure of extended objects with chemical specificity, across a wide range of disciplines [9, 47, 64–67]. More re-

cently, the scope of x-ray ptychography has been extended to probe local crystal orientation and magnetic structure by means of dichroic absorption of circularly polarized x-rays [68–71]. Advances in dichroic ptychographic tomography by Donnelly et al. [72] enabled a direct imaging of the three-dimensional (3-D) magnetization of a $GdCo_2$ pillar using circularly polarized hard x-rays with a resolution of 100 nm. However, soft x-rays are desirable to use for magnetic CDI due to the optimal magnetic contrast accessible from the L-edge resonance of transition metals, as demonstrated in two-dimensional studies [73–75]. Here, we develop a 3-D soft x-ray vector tomography (SXVP) technique that allows for the simultaneous reconstruction of the electron density and the magnetization vector field taking advantage of the L-edge magnetic contrast and achieving an unprecedented spatial resolution of 10 nm.

3.2 Results & discussion

The full 3-D reconstruction and 10 nm resolution achieved with SXVP permits us to invoke homotopy theory [76] and quantify the topological charge of 3-D spin textures directly from experimental data. This represents a significant advantage over methods relying on a combination of hysteresis measurement and micromagnetic simulation to infer the existence and topological charge of 3-D magnetic defects. [77–80].We utilize SXVP to image and quantitatively study the 3-D magnetization of a nickel inverse metalattice [81–83]. This interconnected ferromagnetic network at the nanoscale imposes geometric constraints that compete with the exchange stiffness and magnetostatic energy to produce a magnetically frustrated configuration that can harbor non-trivial magnetization textures. We identify 3-D magnetic defects and directly quantify their topological charge as hedgehogs and anti-hedgehogs [84]. Moreover, we are able to discern between hedgehogs stabilized within the magnetic material and "virtual" hedgehogs located in non-magnetic regions of the sample that induce topologically non-trivial surface magnetization textures.

The existence of topological defects in a system comprised only of nickel can be surprising,

as it is does not possess strong anisotropy or Dzyaloshinskii-Moriya interaction (DMI) as seen in other materials that usually support topological defects, e.g., non-centrosymmetric lattices or magnetic / heavy-metal multilayers [85–87]. However, a large body of work suggests that surface curvature can stabilize magnetic solitons through an effective DMI [88–93]. SXVP gives direct evidence that the competing energies in a nanosized 3-D frustrated magnetic lattice can unlock a richness and functionality of Nickel that was previously unseen.

SXVP operates similar to conventional ptychographic tomography (cPT), whereby a spatially confined x-ray beam is scanned over the sample with partial overlap between adjacent scan points, as depicted in figure 3.1.

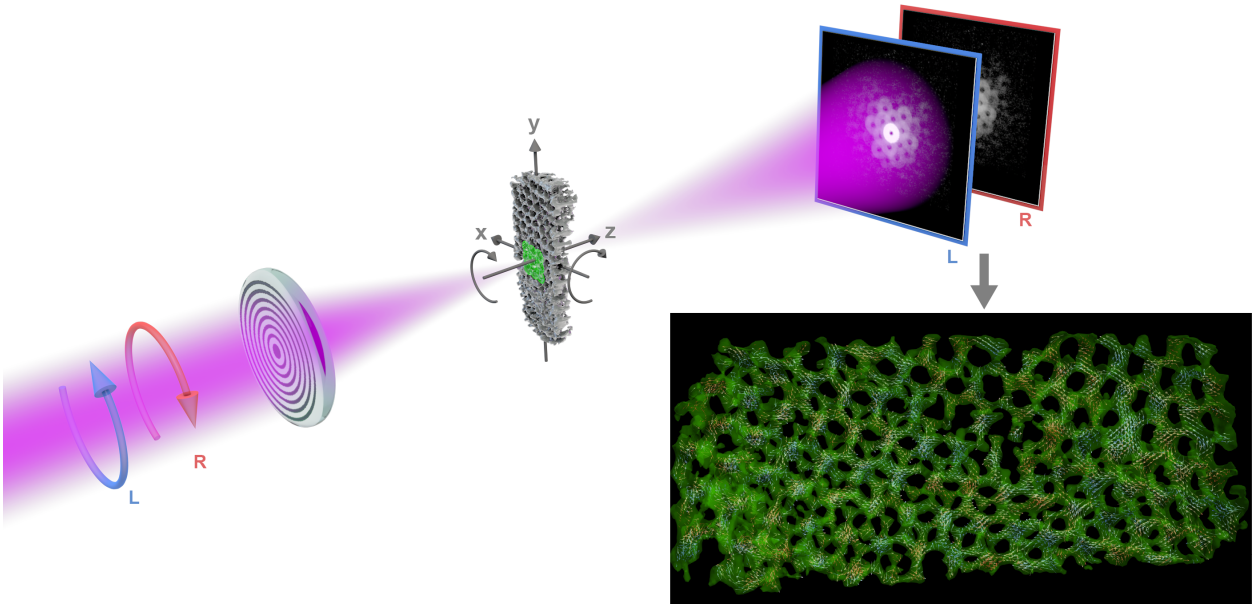

Figure 3.1. Experimental schematic and full field reconstruction. Circularly polarized x-rays (pink) are incident on a Fresnel zone plate and focused onto the sample (center). Green circles on the sample indicate the partially overlapping ptychography scan positions. Curved arrows indicate the two tilt axes required for vector tomography. Diffraction patterns are collected in the far field with both left- and right- circularly polarized incident illumination. The lower inset shows the full density (green) and magnetization (blue-red colormap corresponding to z component) reconstruction.

The x-ray beam is focused by a Fresnel zone plate with an outer width of approximately 45 nm. At each scan point, the scattered x-ray intensity is recorded by a CCD camera placed in the far field. Using iterative reconstruction algorithms in lieu of an objective lens, the set of diffraction patterns produces an image corresponding to a projection of the sample along the beam's propagation direction. To achieve a 3-D reconstruction, the ptychography process is repeated as the sample is tilted about the x-axis and a tomography reconstruction algorithm [94] is applied to the projection images to reconstruct a 3-D volume of the sample.

To image the magnetization vector field, we gain magnetic contrast by utilizing x-ray magnetic circular dichroism (XMCD) [18]. For nickel, we tune the x-ray energy to the L-edge that provides optimal magnetic contrast. In order to decouple the charge density and magnetic components of the measured absorption contrast, as is required when imaging samples with non-trivial structure, a differential measurement is made by changing the incident beam helicity with respect to the sample by 180 degrees. In addition, the reconstruction of the full magnetization vector field without a priori assumptions about its configuration [95] or the use of Maxwell's equations [96, 97] necessitates at least one additional in-plane rotation of the sample. Guided by numerical simulation, we found that three equally spaced 120 degrees in-plane rotations achieved the best reconstruction quality.

SXVP is used to image the magnetization of a magnetic inverse metalattice. This structure is fabricated by infiltrating ferromagnetic nickel into a self-assembled close-packed array of silica nanospheres of an average diameter of 60 nm. The resulting metamaterial consists of an intricate ferromagnetic network where the more capacious regions located at the octahedral and tetrahedral sites are referred to as meta-atoms. The diameter of meta-atoms is approximately 25 nm in octehedral sites and 13 nm in tetrahedral sites. The meta-atom network is connected by thin filaments (< 10 nm) known as meta-bonds.

Our total data acquisition in this case consisted of a tilt series spanning -60 to $+60$ degrees in 4 degree increments, for each in-plane sample rotation. At each tilt position, we acquired ptychography scans. This resulted in a reconstructed field of view approximately

1×0.5 μm at a spatial resolution of 10 nm (see Supplemental material: resolution quantification). The high spatial resolution combined with the large field of view results in the highly detailed magnetization vector field shown in figure 3.1 (inset). We stress that the magnetization vector field imaged by the presented SXVP technique is fully 3-D and self-consistent, i.e., no supporting assumptions are made to allow for its reconstruction. Therefore, the magnetization vector field shown in figure 3.1 (inset) is an unambiguous, quantitative measurement.

We analyze the reconstructed magnetization vector field by means of homotopy theory [76] with the goal of identifying and classifying non-collinear spin textures. In 3-D magnetic systems, the topological point defect and surrounding magnetization texture is colloquially referred to as a "hedgehog". The topological charge, or hedgehog number within a bulk Ω, follows the bulk-surface relationship [98]

$$\mathcal{Q} = \int_{\Omega} dxdydz\, \rho = \frac{1}{8\pi} \int_{\partial\Omega} dx^j \wedge dx^k\, \mathbf{n} \cdot (\partial_j \mathbf{n} \times \partial_k \mathbf{n}) \tag{3.1}$$

where $\rho = \epsilon^{ijk} \partial_i \mathbf{n} \cdot (\partial_j \mathbf{n} \times \partial_k \mathbf{n})/8\pi$ is the hedgehog density, $\partial\Omega$ is the bounding surface, and $\mathbf{n}$ is a normalized vector field. Here, ϵ^{ijk} is the Levi-Civita symbol and the Einstein summation is implied over the indices: $i = 1, 2, 3 \leftrightarrow x, y, z$. The right-hand-side of Eq. (3.1) is the skyrmion number on the boundary $\partial\Omega$. This expression is commonly used to evaluate skyrmions on 2-D planes [99], but can be generally applied to any curvilinear coordinate system [100]. When the surface magnetization of a sphere enclosing a volume covers the parameter space $\mathbb{S}^2$ exactly once, we have hedgehog number $\mathcal{Q} = \pm 1$, which are topologically nontrivial sectors with the lowest energy [101, 102]. Conventionally, $\mathcal{Q} = +1$ is referred to as a hedgehog and $\mathcal{Q} = -1$ as an anti-hedgehog.

To locate hedgehogs from the experimentally reconstructed magnetization vector field, we systematically search for local maxima in the absolute hedgehog density. An enclosed surface with one voxel radius is then defined around each identified maximum to unambiguously determine the hedgehog number, via Eq. (3.1) (see Supplemental material for details of the calculation).

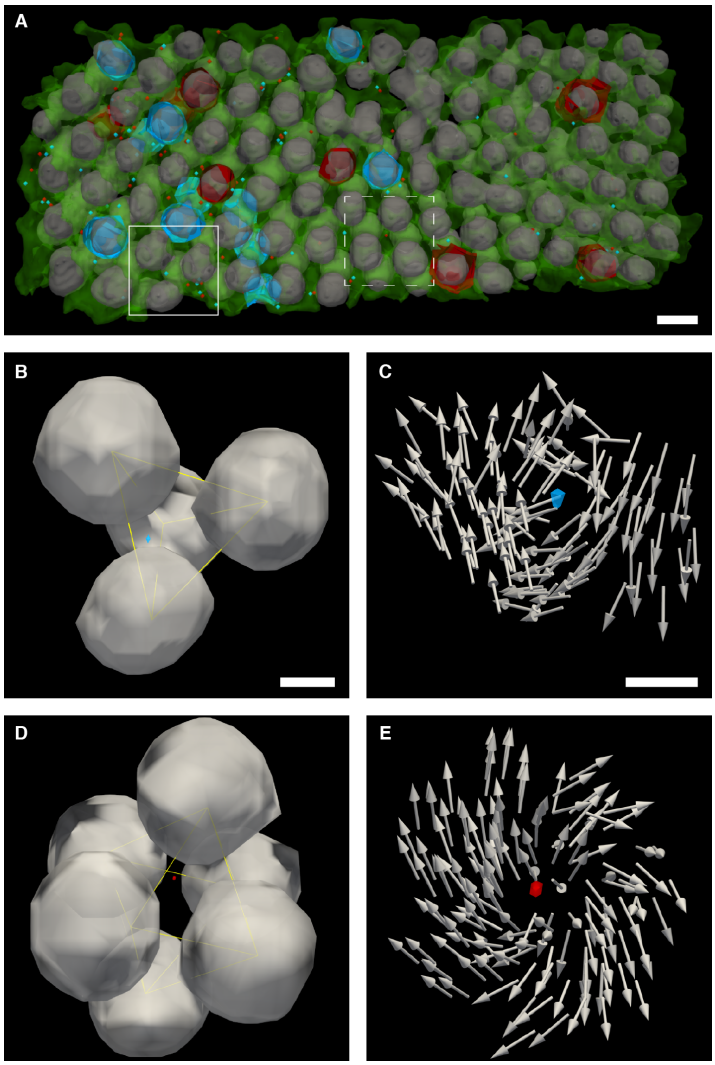

Figure 3.2. Full field reconstruction and hedgehogs in bulk. (A) The full density (green) reconstruction with marked locations of $\mathcal{Q} = +1$ and $\mathcal{Q} = -1$ hedgehogs in bulk (red and blue points, respectively), and internal void surfaces with $|\mathcal{Q}| > 0.9$ (red positive, blue negative). Void surfaces are indicated by a gray isosurface. The solid and dashed white boundaries mark regions of interest shown in (B-C) and (D-E), respectively. **(B** and **C)** The location and magnetization texture of an antihedgehog ($\mathcal{Q} = -1$) in bulk within a tetrahedral meta-atom site. **(D** and **E)** The location and magnetization texture of a hedgehog ($\mathcal{Q} = +1$) in bulk within an octahedral meta-atom site. Scale bars in (A-C) are 60, 25, 10 nm respectively.

The 3-D spatial distribution of hedgehogs is shown in figure 3.2. A total of 68 hedgehogs (red dots) and 70 anti-hedgehogs (blue dots) were found in the bulk of the vector field. Moreover, we correlate the location of each hedgehog with a meta-atom type to assess the role of geometric confinement in the stabilization of hedgehogs (see table 3.S1). Figure 3.2B shows an anti-hedgehog ($\mathcal{Q} = -1$) located in the tetrahedral meta-atom indicated in panel A with a solid white box. A hedgehog ($\mathcal{Q} = +1$) is shown in figure 3.2C, located in the octahedral meta-atom indicated by a dashed white box in panel 3.2A. The magnetization vector field of the two example hedgehogs are shown in figures 3.2C and 3.2E, respectively. The sign of the hedgehog number is not apparent from the magnetization vector field, but can be unambiguously seen by computing $\mathbf{B}_\mathrm{e}$ (see Supplemental material: "Emergent B field"). We find that the ratio of hedgehogs in octahedral meta-atoms to tetrahedral meta-atoms is approximately 2:1, despite tetrahedral meta-atoms outnumbering their octahedral counterparts by a factor of 2. Furthermore, an octahedral meta-atom is ~ 6 times larger by volume than its tetrahedral counterpart. Our findings are consistent with the prediction that octahedral meta-atoms would more readily host defects due to their larger size [82].

In addition to studying the influence of meta-atom confinement on hedgehog abundance, the high resolution 3-D spatial information recovered by SXVP allows us to perform statistics on hedgehog pairing and separation distance. Current theory on hedgehog confinement states that the potential energy of a hedgehog-anti-hedgehog pair grows linearly with separation distance when the exchange energy dominates, implying all flux ($\mathbf{B}_\mathrm{e}$ streamlines) from the hedgehog must end at the anti-hedgehog, forming a flux tube to minimize the energy [103].

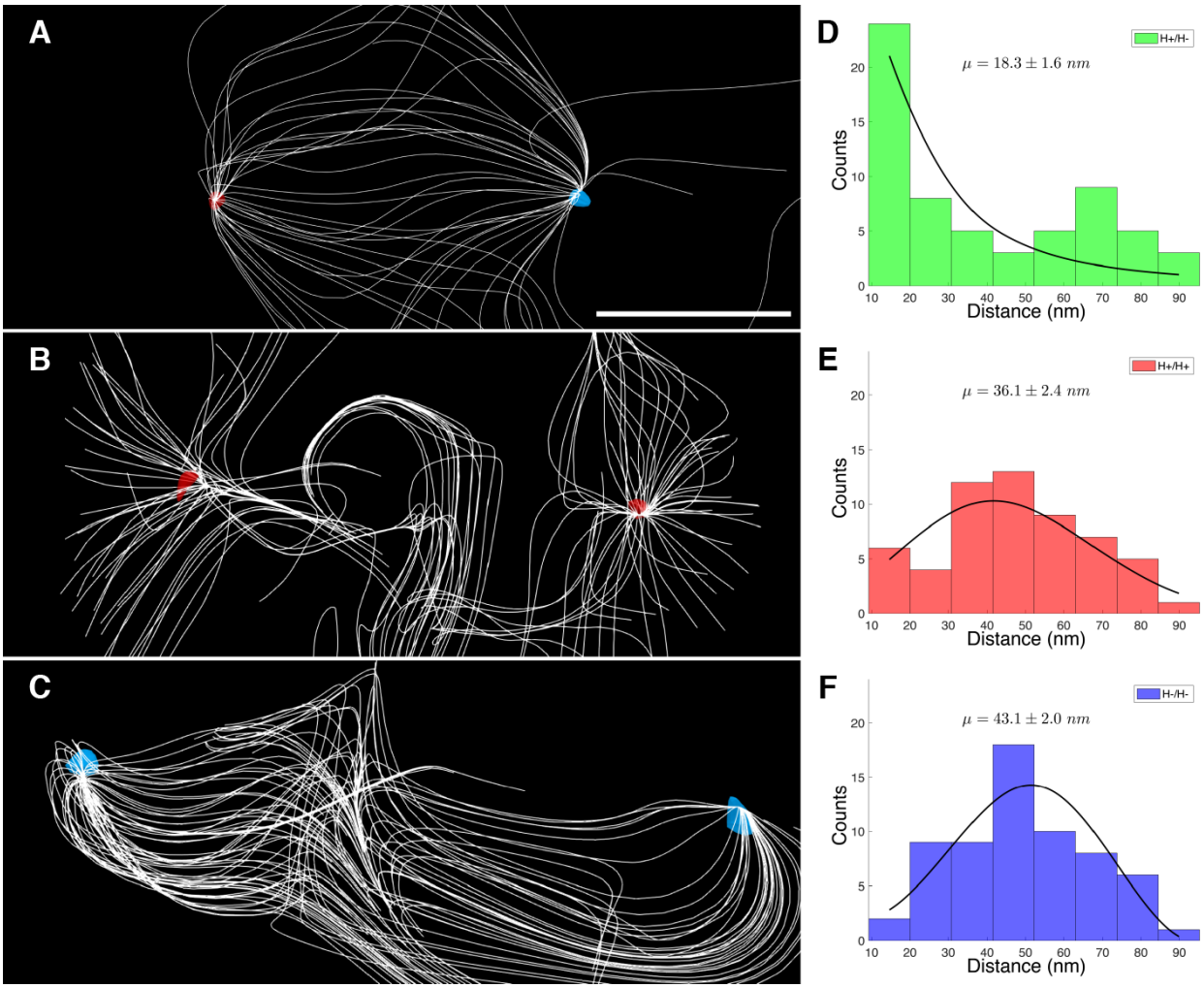

Figure 3.3. Hedgehog pairs in bulk with emergent field and nearest-neighbor distance statistics. **(A-C)** Hedgehog pairs in bulk, with emergent B field streamlines. The positions of $\mathcal{Q} = +1$ and $\mathcal{Q} = -1$ hedgehogs are marked with red and blue isosurfaces, respectively. **(D-F)** Histograms of nearest-neighbor distance for all three combinations of hedgehog charge accompanied by lines of best fit. Mean distances are reported for each case. Scale bar, 10 nm.

A non-negligible pair separation is an indication that competing interactions are driving the system into a frustrated state. Figure 3.3 summarizes our findings, alongside three examples of hedgehog pairing observed in the metalattice. Arrows indicate the magnetization

texture of the hedgehog, surrounded by a core indicating the location and polarity of the hedgehog. Streamlines follow the emergent $\mathbf{B}_e$ field generated by the magnetization. We observe that only part of flux emanating from the hedgehog terminates at the anti-hedgehog in fig. 3.3A, i.e. the $\mathbf{B}_e$ streamlines are not completely confined. For completeness, we show pairs of similarly charged hedgehogs in fig. 3.3(B-C), in which the $\mathbf{B}_e$ streamlines exhibit no confinement. The partial confinement shown in fig. 3.3A along with the observed hedgehog - antihedgehog pair distance suggests that additional factors compete with the linear exchange energy to stabilize topological defects in the metalattice.

We observe a mean hedgehog-antihedgehog nearest neighbor distance of approximately 18 nm, while hedgehog-hedgehog and antihedgehog-antihedgehog pairs are stabilized at comparatively larger distances of 36 nm and 43 nm, respectively. The observed non-negible pair separation distance provides insight into understanding the metalattice as a magnetically frustrated system. Further, the statistically significant difference in nearest-neighbor distance between oppositely charged hedgehogs and similarly charged hedgehogs is physically consistent with theory and serves as a reconstruction validation.

In general, the bulk-edge correspondence defined in Eq. (3.1) implies that $\mathcal{Q}$ can be computed on an arbitrary surface. In an inverted metalattice, the silica nanospheres compose magnetically inert voids that naturally define magnetic surfaces within the metamaterial. A finite hedgehog number obtained from such surfaces is indicative of an emergent field originating from the magnetic void, a situation we refer to as "virtual" hedgehog. To investigate this scenario, we first perform a non-convex triangulation of the nickel structure shown in fig. 3.2A. The resulting facets are grouped into individual void surfaces using community-clustering techniques commonly found in network analysis [104]. Due to the thinness of the sample, the majority of voids are not closed, implying that they do not possess integer hedgehog number. In these cases, we consider any void surface with $|\mathcal{Q}| \geq 0.9$ as non-trivial, in accordance with micromagnetics literature [105].

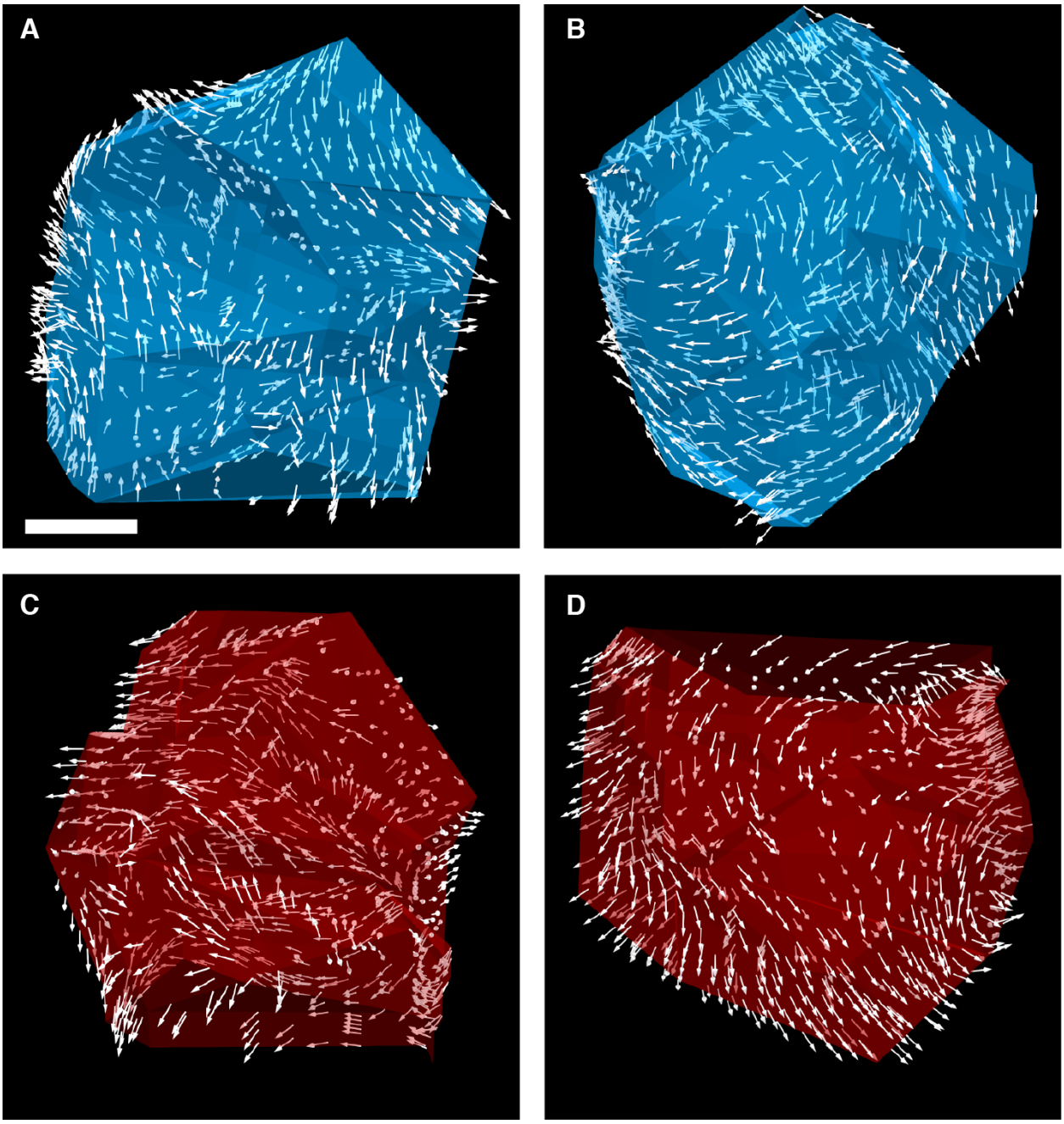

Figure 3.4. Topologically non-trivial void surfaces. **(A)** A partially open void surface laying on the metalattice sample boundary with hedgehog charge $\mathcal{Q} = -0.99$. **(B)** A closed internal void surface with hedgehog charge $\mathcal{Q} = -1$. **(C)** and **(D)** Two partially open voids with hedgehog charge $\mathcal{Q} = +0.96$ and $\mathcal{Q} = +1.01$, respectively. Scale bar, 15 nm.

Our analysis of the internal voids reveals a network of "virtual" hedgehogs whose distribution is displayed in fig. 3.2A by colored spherical surfaces where blue and red represent virtual antihedgehogs and hedgehogs, respectively. Specific examples are shown in fig. 3.4, including the surface magnetization texture. Equivalently, topological defects can be represented by their coverage of order parameter space [102]. In the case of 3-D magnetization defects, this corresponds to mapping $\mathbb{R}^3 \rightarrow \mathbb{S}^2$, after which the surface coverage of $\mathbb{S}^2$ is evaluated. We perform this mapping to independently check the hedgehog number calculations for the observed virtual hedgehogs (for details, see: fig. 3.S5).

3.3 Conclusion

We demonstrate the technique of soft x-ray 3-D vector ptychography, which is applied to image the structure and magnetization vector field of a 3-D frustrated ferromagnetic metalattice. The resolution comparable to the magnetic exchange length achieved by SXVP, allows us to quantitatively examine the distribution of hedgehog magnetic defects within the metalattice bulk as well as on the internal voids. This work sets the foundation for further study of metalattice systems as a candidate for spin transport applications, as well as the fundamental study of hedgehog dynamics. We envision this technique can be combined with other magnetic imaging techniques such as electron holography, to gain further material insight via multi-modal imaging at a variety of length scales.

3.4 Supplemental material

3.4.1 XMCD

On resonance, magnetic materials exhibit absorption of circularly polarized x-rays that is proportional to the degree of alignment between the angular momentum of the incident beam and the local magnetization under illumination XMCD $\propto \mathbf{m} \cdot \sigma$. In $3d$ transition

metals, this is due to the spin sensitive $1s \rightarrow 2p$ (K) and $2p \rightarrow 3d$ (L) dipole-permitted photoexcitations, with the latter being approximately 3 orders of magnitude stronger than the former [18].

3.4.2 Experiment

The x-ray ptychography experiment was conducted at the COSMIC beam line at the Advanced Light Source (ALS) in Lawrence Berkeley National Lab (LBNL) [106]. The incident photon energy was tuned to 856 eV, slightly above the Nickel L_3 edge, to maximize absorption contrast. An elliptical polarization undulator allowed us to generate circularly polarized x-rays of either helicity and achieve differential contrast enhancement of the magnetic signal, after which the polarized beam was incident on a bespoke Fresnel zone plate with an outer width of approximately 45 nm and focused onto the sample. The vector tomography dataset consisted of three equally-spaced in-plane rotations of the sample. At each in-plane rotation angle, the sample was tilted from -62 degrees to +62 degrees in 4 degrees steps. At each tilt angle, the focused beam was raster-scanned across the sample in 40 nm steps. Diffraction patterns were collected using both left and right circularly polarized x-rays. A far-field CCD camera was used to record diffraction patterns at each scan position. Initial reconstructions were performed on-site in real time with a GPU cluster at the National Energy Research Scientific Computing Center (NERSC), using the SHARP ptychography reconstruction algorithm [107].

3.4.3 Sample fabrication

We developed a method for fabricating inverse metal metalattices consisting of sub-100 nm spheres (for full details, see [83]). Briefly, monodisperse silica nanospheres are first synthesized in a colloidal solution and assembled into a close-packed colloidal crystal with FCC order. The assembly used the vertical deposition method described in the literature,

but with refinements in which the diluted aqueous colloidal solution was evaporated onto a tilted vertical silicon wafer in plastic vials. This base template structure can be tuned from monolayer to microns in thickness, with sphere sizes from the nanometer to microns. We then used confined supercritical fluid chemical deposition of metals because conventional chemical vapor deposition is typically not suitable for deposition of interconnected metal inverse nanostructures with sub-100 nm nanospheres. The interstitial space between the nanospheres of the colloidal crystal is then infiltrated with nickel, forming a metal inverse metalattice structure. It is very important to prepare the sample at the correct geometry so we can perform vector tomography with three in-plate rotations successfully without shadowing and strong x-ray attenuation from the thickness that reduces the image contrast. The bulk (a few mm in size) metalattice was sitting on a silicon substrate and lifted off using a focused ion beam (FIB, FEI Nova 600 NanoLab DualBeam) milling, which is equipped with a field emission scanning electron microscope (SEM) and a scanning Gallium ion beam. The FIB prepared sample is first mounted on a 3-mm TEM grid (Omniprobe, 3 posts copper lift-out grid), where the central post was also trimmed by FIB milling to reduce the potential shadowing for x-ray imaging. The grid-mounted sample was examined by the SEM and an optical microscope, and then manually glued on a 3-mm copper ring using a silver paste, as shown in figure 3.S1. In this case, the sample can be manually rotated in-plane for vector tomography. The sample studied here consists of 1-2 layers of nanospheres.

3.4.4 Data processing and ptychographic reconstruction

The final ptychography reconstructions were performed using the regularized ptychographic iterative engine (rPIE) [108] with a modification to address defocus at high tilt, discussed below in further detail. A small number of corrupt diffraction patterns, most commonly caused by detector readout malfunction or unstable beamline flux, can cause a global degradation of the reconstructed object wave-front through the innate coupling of the probe and object. Therefore, we used the following procedure to automatically detect and remove

corrupt diffraction patterns to achieve the highest quality reconstructions possible. The high-angle diffraction intensity at each scan position was integrated to produce a low-resolution map of every ptychography scan. Local maxima in the magnitude of the gradient of this map were used to identify and remove bad frames as a pre-reconstruction data processing step, as determined by an ad-hoc threshold. In addition, a phase unwrapping constraint was enforced on the probe as part of each macro-iteration of the reconstruction to deal with defocus at high tilt angles. From the reconstructed complex-valued exit wave, we used the absorption component to utilize the strongest possible magnetic contrast [72].

After high quality projections were reconstructed, the two oppositely-polarized projections at each tilt angle were aligned using a feature-based image registration package in MATLAB. The projections were converted to optical density to normalize any small temporal and polarization-based fluctuations of the beam intensity. In each projection, background subtraction was performed by numerically evaluating Laplace's equation, using the region exterior to the sample as the boundary condition. We found that this method outperforms simple constant background subtraction, as it can accommodate local variations.

3.4.5 Scalar and vector tomography

The relationship between charge and magnetic scattering [109, 110]:

$$f = f^{(c)} \pm i f^{(\mathrm{mag})} \hat{\mathbf{z}} \cdot \mathbf{m} \tag{3.2}$$

was used to generate a set of pure scalar and vector projections corresponding to the charge scattering and magnetic scattering respectively, where $f^{(c)}$ is the charge scattering factor, $f^{(\mathrm{mag})}$ is the magnetic scattering factor, $\hat{\mathbf{z}}$ is the x-ray propagation direction and $\mathbf{m}$ is the magnetization. The scalar projections were reconstructed in three independent subsets, each corresponding to the tilt series of one in-plane rotation. The projections were first roughly aligned with cross-correlation, then more accurately aligned using center of mass and common line alignment. After each subset was reconstructed, we performed iterative

angular and spatial refinement to adjust any remaining small alignment errors. Gradient descent volume registration was performed among the three subset reconstructions and the resulting transform matrices were applied to align the projections to a global coordinate system. The combined scalar dataset was reconstructed and the same angular and spatial refinement procedure was performed again. The transformations applied to align the scalar projections were then applied to the vector projections.

3.4.6 Vector tomography reconstruction algorithm

The reconstruction of a vector field caused by magnetic material is modeled as a least squares optimization problem and can be solved directly by gradient descent. The least squares problem is given as

$$\begin{aligned} min_{O_1,O_2,O_3} f(O_1,O_2,O_3) &= \sum_{i=1}^{N} \|\alpha_i \Pi_i O_1 + \beta_i \Pi_i O_2 + \gamma_i \Pi_i O_3 - b_i\|^2 \\ &= \sum_{i=1}^{N} \|\Pi_i(\alpha_i O_1 + \beta_i O_2 + \gamma_i O_3) - b_i\|^2 \end{aligned} \tag{3.3}$$

The squared sum is taken over the N projection tilt series where O_1, O_2, O_3 are the three components of the vector field to be reconstructed, Π_i is the projection operator with respect to tilt Euler angle set $\{\phi_i, \theta_i, \psi_i\}$, and b_i is the corresponding measured projection. $\{\alpha_i, \beta i, \gamma_i\}$ is the coefficient set with respect to projection operator and these coefficients can be computed from formulas related to the corresponding Euler angle set. Specifically, the formula is given by

$$\alpha_i = \sin\theta_i \cos\phi_i, \quad \beta_i = \sin\theta_i \sin\phi_i, \quad \gamma_i = \cos\theta_i \tag{3.4}$$

The least square problem can be solved via gradient descent. The gradients are computed component-wise as follows

$$\nabla_{O_1} f(O_1, O_2, O_3) = \sum_{i=1}^{N} \alpha_i \Pi_i^T \Pi_i (\alpha_i O_1 + \beta_i O_2 + \gamma_i O_3)$$
$$\nabla_{O_2} f(O_1, O_2, O_3) = \sum_{i=1}^{N} \beta_i \Pi_i^T \Pi_i (\alpha_i O_1 + \beta_i O_2 + \gamma_i O_3) \tag{3.5}$$
$$\nabla_{O_3} f(O_1, O_2, O_3) = \sum_{i=1}^{N} \gamma_i \Pi_i^T \Pi_i (\alpha_i O_1 + \beta_i O_2 + \gamma_i O_3)$$

The update reads

$$O_1^{k+1} = O_1^k - t\nabla_{O_1} f(O_1, O_2, O_3) = O_1^k - t \sum_{i=1}^{N} \alpha_i \Pi_i^T \Pi_i (\alpha_i O_1^k + \beta_i O_2^k + \gamma_i O_3^k)$$
$$O_2^{k+1} = O_2^k - t\nabla_{O_2} f(O_1, O_2, O_3) = O_2^k - t \sum_{i=1}^{N} \beta_i \Pi_i^T \Pi_i (\alpha_i O_1^k + \beta_i O_2^k + \gamma_i O_3^k) \tag{3.6}$$
$$O_3^{k+1} = O_3^k - t\nabla_{O_3} f(O_1, O_2, O_3) = O_3^k - t \sum_{i=1}^{N} \gamma_i \Pi_i^T \Pi_i (\alpha_i O_1^k + \beta_i O_2^k + \gamma_i O_3^k)$$

for an appropriate step size t. For a given tilt angle set $\{\phi_i, \theta_i, \psi_i\}$, we compute the (forward) projection of a 3D object by using the Fourier slice theorem. The back-projection is carried out by linear interpolation. An alternative approach to compute forward and back projections is using the Radon transform.

3.4.7 Micromagnetic simulations

The energetically favorable magnetic states in the material were numerically modeled by micromagnetic simulations. We used the GPU-accelerated package Mumax3 [111] installed on UCLA's Hoffman2 cluster. The experimentally reconstructed scalar image was used to define the magnetic region, discretized in cells of 5 nm×5 nm×5 nm.

The magnetic ground state is obtained by minimizing the magnetic energy from a uniform random initial condition. For this, we utilize the built-in function `relax` that evolves only

the dissipative term in the Landau-Lifshitz equation

$$\frac{\partial \mathbf{m}}{\partial t} = \gamma \mu_0 \alpha \mathbf{m} \times (\mathbf{m} \times \mathbf{H}_{\text{eff}}) \,, \tag{3.7}$$

where the dissipation is scaled by the Gilbert damping parameter α, $\gamma = 28$ GHz/T is the gyromagnetic ratio, μ_0 is the vacuum permeability, M_s is the saturation magnetization, and $\mathbf{H}_{\text{eff}}$ is the effective field that includes exchange and non-local dipole fields.

The relevant magnetic parameters for our simulation are the saturation magnetization and the exchange constant. From Ref. [83], we set $M_s = 350$ kA/m. This value is consistent with those reported for Ni nanoparticles [112] and nanocubes [113]. The exchange constant A is not expected to change drastically in the hundred of nanometers range, and we use the value $A = 3.4$ pJ/m reported in Ref. [114], similar to that reported for Ni nanocubes [113]. This exchange stiffness results in an exchange length of 6 nm. Our cell sizes are smaller than the exchange length, ensuring proper convergence of small magnetic features.

Because the material has a curved geometry, shape anisotropy originating from non-local dipole fields will dominate over any intrinsic sources of anisotropy. Therefore, we do not include magnetocrystalline nor uniaxial anistropy. In addition, grain structure is not considered in the magnetic region.

3.4.8 Hedgehog number

Hedgehogs follow a topological conservation law

$$\partial_t \rho + \nabla \cdot \mathbf{j} = 0 \,. \tag{3.8}$$

Here, the hedgehog four-current [98] is

$$j^\mu \equiv (\rho, \mathbf{j}) = \frac{1}{8\pi} \epsilon^{\mu\nu\alpha\beta} \partial_\mu \mathbf{n} \cdot (\partial_\alpha \mathbf{n} \times \partial_\beta \mathbf{n}) \,, \tag{3.9}$$

where the Einstein summation is implied over the indices: $\mu \in \{t, x, y, z\}$ and $\epsilon^{\mu\nu\alpha\beta}$ is the Levi-Civita symbol. The conservation law of hedgehogs holds regardless of the fluctuation

of the magnitude of $\mathbf{n}$. The hedgehog number $\mathcal{Q}$, which is the volume integration of the hedgehog density ρ, is integer-valued when $\mathbf{n}$ is a normalized vector field, corresponding to the nontrivial second homotopy group of the order parameter space $\pi_2(S^2) = \mathbb{Z}$. The hedgehog number relationship in Eq. (3.1) is amenable to numerical analysis because the hedgehog density simplifies a 3-D vector field into a signed scalar field.

3.4.9 Hedgehog number computation

The winding number of a vector field can be expressed as

$$w = \frac{1}{4\pi} \int \mathbf{n} \cdot (\partial_1 \mathbf{n} \times \partial_2 \mathbf{n}) dx_1 dx_2 \tag{3.10}$$

which can be evaluated on any arbitrary surface [100]. Equivalently, the winding number can be understood as the summed solid angle spanned by groups of three neighboring vectors. To numerically evaluate this expression, we triangulate the surface of interest, then sum the solid angle subtended by three vectors laying on the vertices of each facet, as given by the expression [115]

$$\tan\left(\frac{\Omega}{2}\right) = \frac{\hat{a} \cdot (\hat{b} \times \hat{c})}{1 + \hat{a} \cdot \hat{b} + \hat{b} \cdot \hat{c} + \hat{c} \cdot \hat{a}}, \tag{3.11}$$

where Ω is the solid angle and $\hat{a}, \hat{b}, \hat{c}$ are directions of vectors at three vertices. The void surfaces were generated by extracting the boundary facets of the alphaShape [116] triangulation of the scalar reconstruction. The hedgehogs in bulk were first identified by local maxima in the hedgehog volume density, and then verified by numerically evaluating the hedgehog number on the enclosing surface.

3.4.10 Emergent B field

The emergent $\mathbf{B}_\mathrm{e}$ field generated by the magnetization field $\mathbf{n}$ is given by

$$B_i = \frac{1}{8\pi} \epsilon_{ijk} \mathbf{n} \cdot (\nabla_j \mathbf{n} \times \nabla_k \mathbf{n}) \tag{3.12}$$

where ϵ_{ijk} is the Levi-Civita symbol. Hedgehogs form sources and sinks of the $\mathbf{B}_\mathrm{e}$ field as given by

$$\nabla \cdot \mathbf{B_e} = \rho \text{ or } \mathcal{Q} = \int d\mathbf{S} \cdot \mathbf{B}_\mathrm{e}, \tag{3.13}$$

where ρ is the hedgehog density. The sign of the hedgehog charge is not obvious from the configuration of $\mathbf{n}$. However, we can use $\mathbf{B_e}$ to determine the sign of hedgehogs, as seen in fig. 3.S7, since $\mathcal{Q}$ is the source of $\mathbf{B_e}$.

3.4.11 Resolution quantification

In order to quantify the reconstruction resolution, the entire set of projections was divided into two halves and reconstructed independently. The Fourier shell correlation (FSC) was calculated between the two reconstructions, as shown in fig. 3.S4A. The conventional 0.1 threshold indicates the effective resolution is $\sim$ 10 nm. As a further validation, we analyze the reconstructed hedgehog pair shown in fig. 3.S4B, in which the distance between the hedgehog and antihedgehog is $\sim$ 15 nm. We perform the hedgehog number calculation for the antihedgehog and hedgehog separately as an additional resolution benchmark. The surfaces of integration are denoted in green in fig. 3.S4(B-D) and the resulting hedgehog numbers are $\mathcal{Q} = 0$, $\mathcal{Q} = -1$ and $\mathcal{Q} = +1$, respectively.

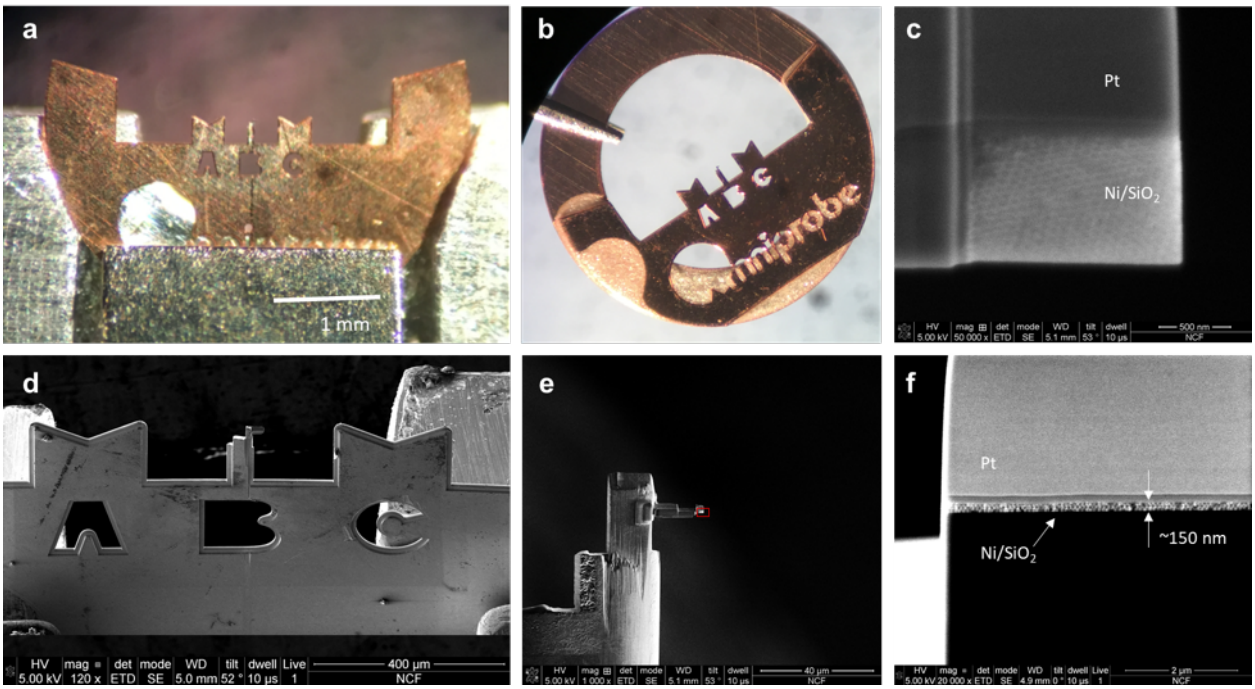

Figure 3.S1. Sample preparation and SEM images. The FIB milling prepared sample is first mounted on a 3-mm TEM lift-out grid (**A** microscope image, and **B**, SEM image) and then glued on a copper ring (**C**, microscope image). **E**. An SEM image shows the sample (red box) on a copper post, with a zoom-in 45° tilted view in **F**. The sample thickness used in the x-ray experiment is about 150 nm as seen in a side view in **C**. The mounting geometry is critical to successfully perform vector tomography with three in-plate rotations.

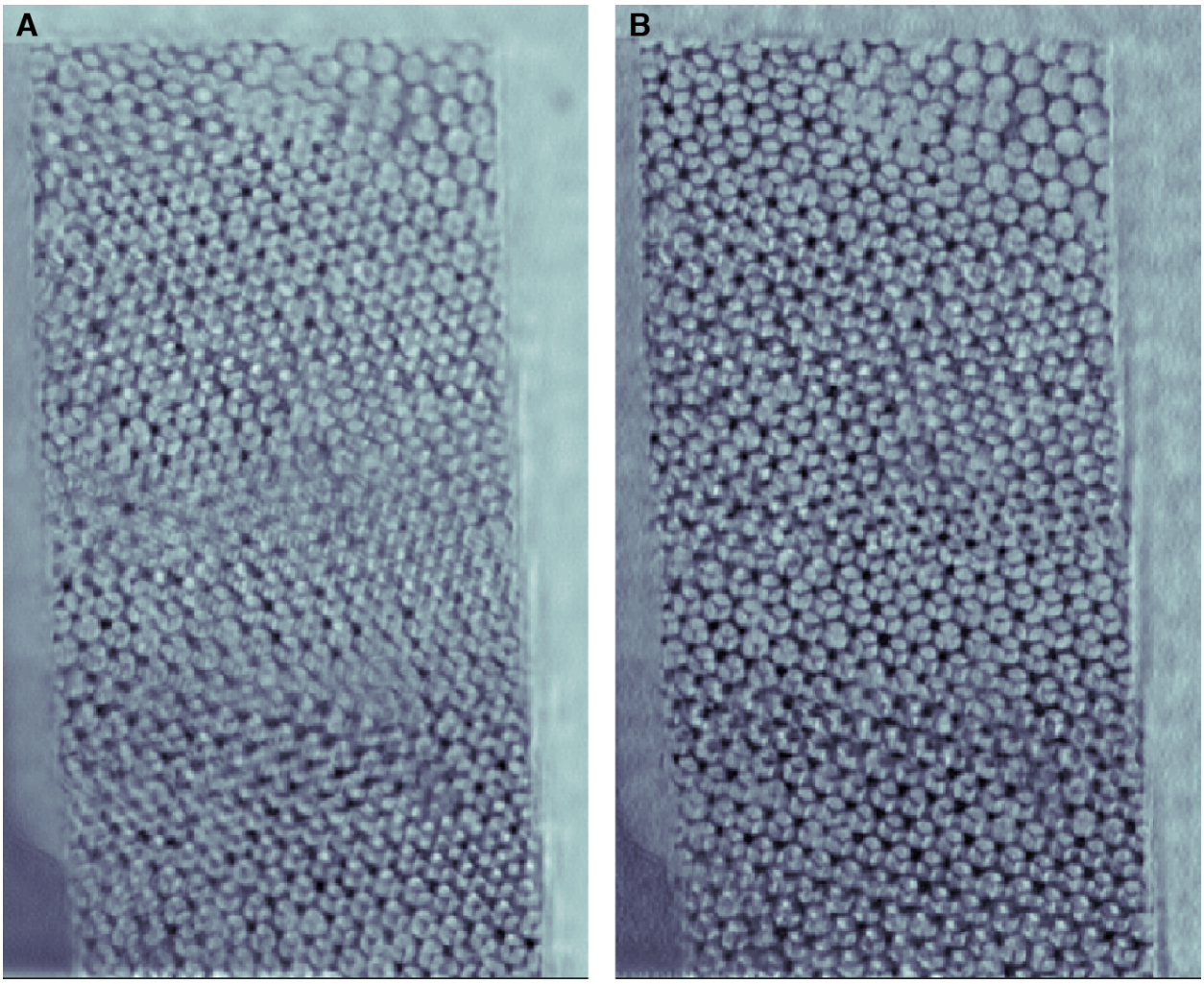

Figure 3.S2. Ptychography reconstruction before and after gradient based bad frame detection.(A) A ptychography reconstruction of a dataset with a small number of bad diffraction patterns causing reconstruction artifacts. **(B)** The same dataset with the bad diffraction patterns detected and removed.

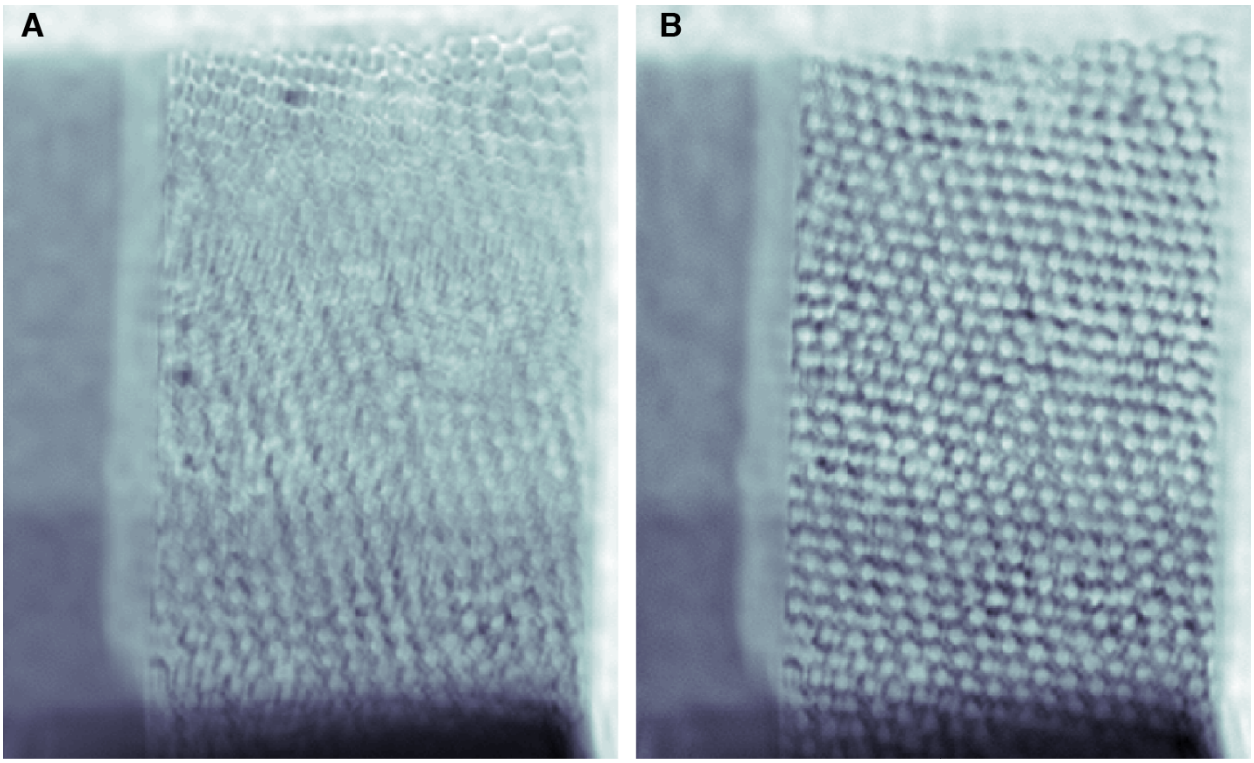

Figure 3.S3. Ptychography reconstruction before and after defocus correction.(A) A high tilt ptychography reconstruction exhibiting contrast inversion that is characteristic of defocus. **(B)** The same dataset reconstructed with iterative defocus correction.

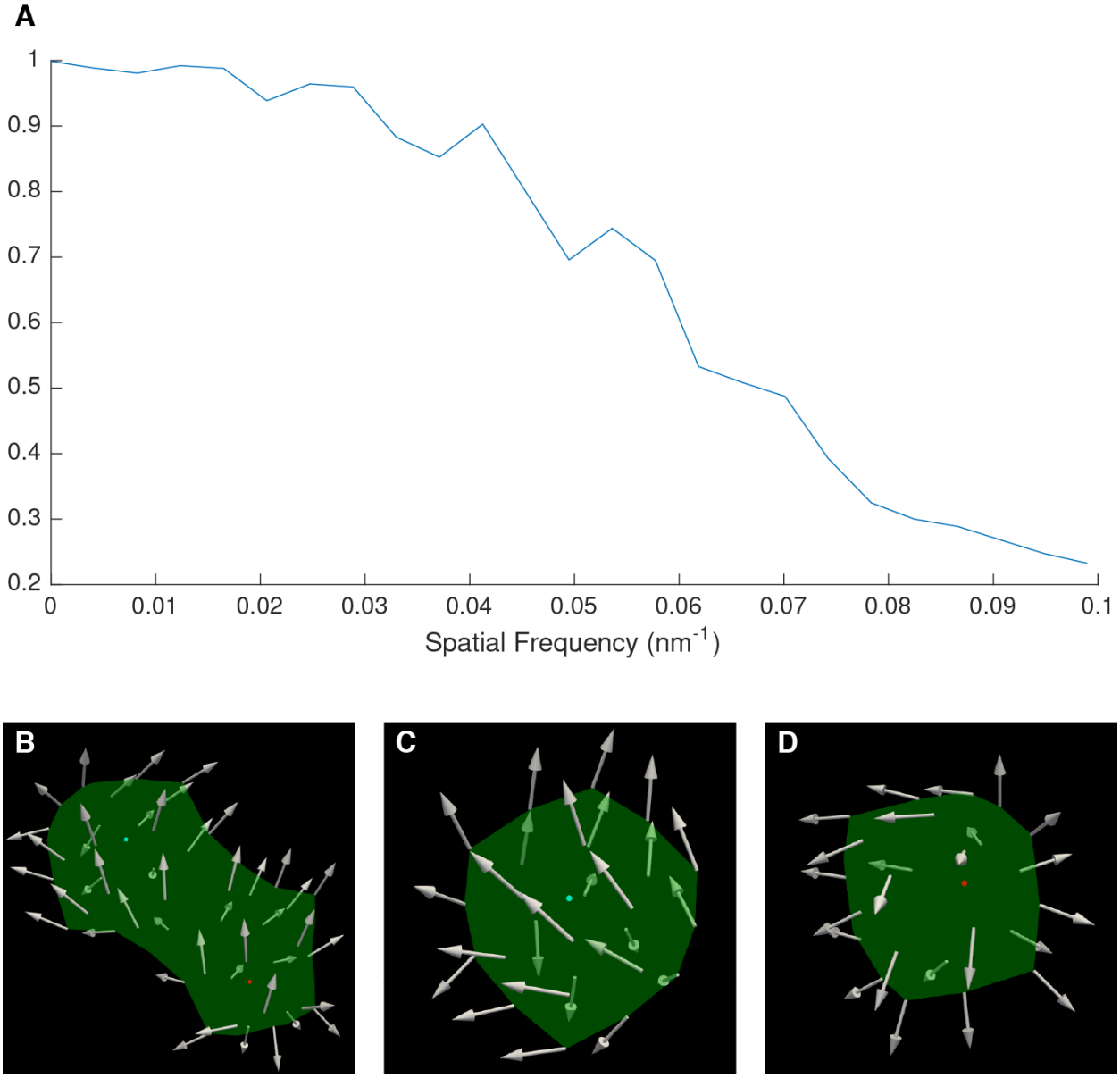

Figure 3.S4. Reconstruction resolution. **(A)** The fourier shell correlation (FSC) indicating a correlation above the 0.1 threshold at the diffraction limit resolution. **(B)** A hedgehog pair in bulk, with hedgehog separation of $\sim$ 15 nm. The surface of integration is shown in green. The antihedgehog and hedgehog are shown separately in **(C)** and **(D)** respectively.

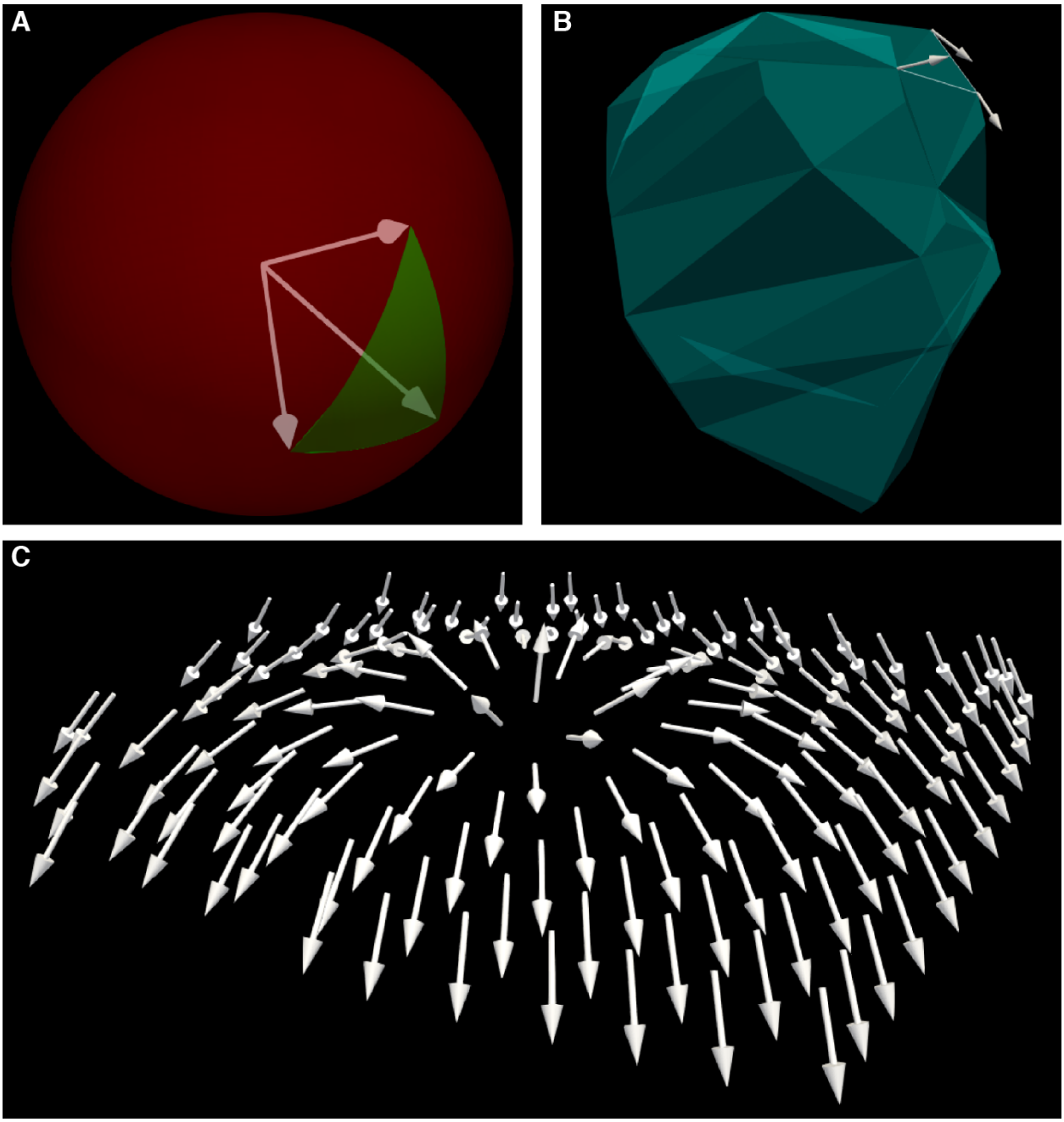

Figure 3.S5. Order parameter space representation of a virtual hedgehog. (A) The solid angle subtended by one facet in $\mathbb{S}^2$. **(B)** The $\mathbb{R}^3$ representation of the same facet shown in (A). **(C)** The stereographic projection of the parameter space $\mathbb{S}^2$ covered by the virtual hedgehog shown in (B).

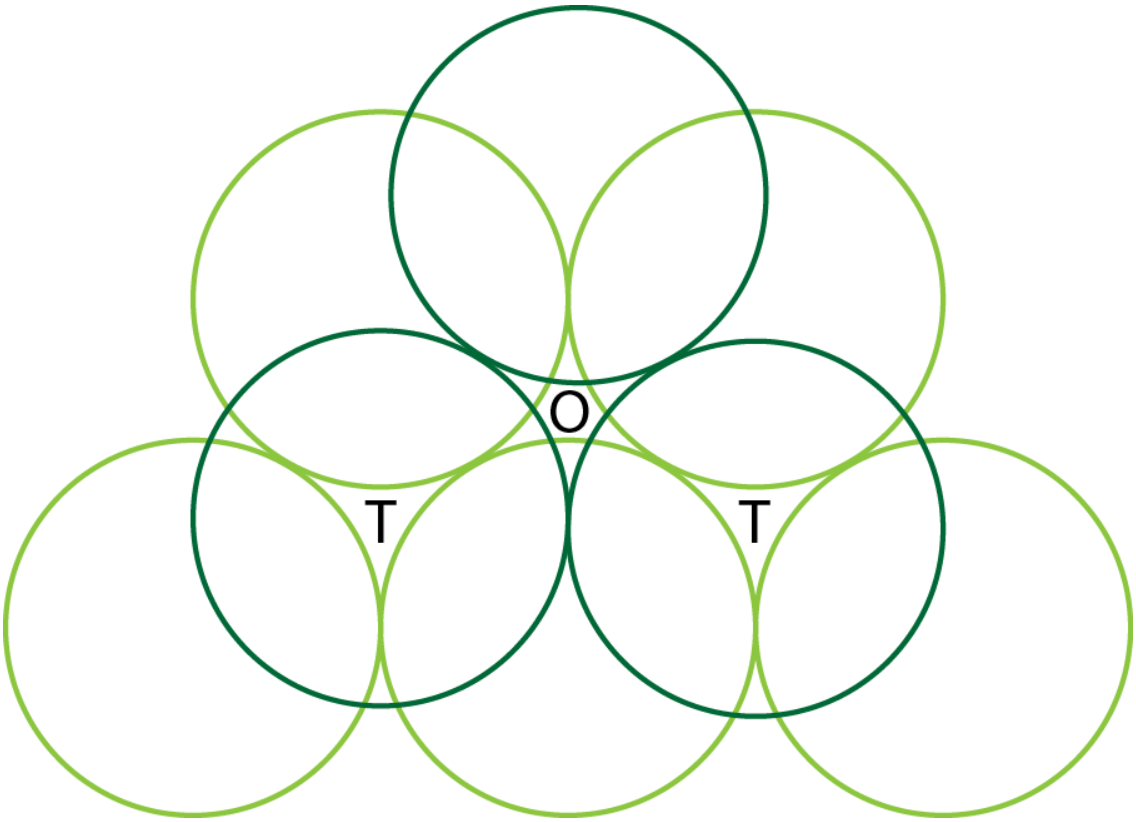

Figure 3.S6. Tetrahedral and octahedral interstitial meta-atoms. An illustration of two layers of close-packed spheres, denoting the positions of tetrahedral (T) and octahedral(O) sites.

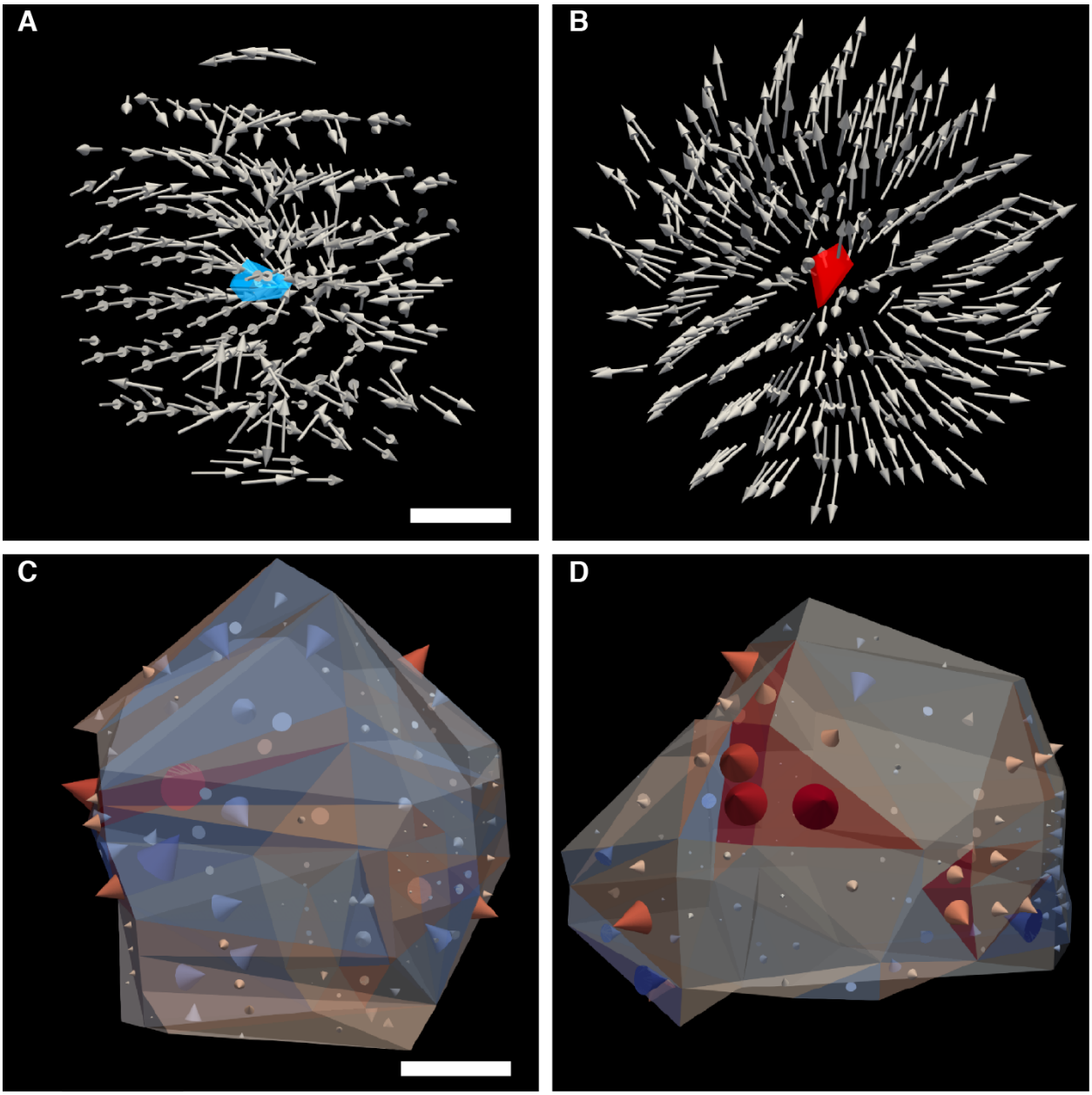

Figure 3.S7. Hedgehog and Anti-Hedgehog magnetization and emergent B_e field vector plots. **(A)** and **(B)** The emergent B field of the anti-hedgehog and hedgehog shown in 3.2C and E, respectively. The vector plots indicate that hedgehogs and anti-hedgehogs form sources and sinks in the emergent field. **(C)** and **(D)** The emergent B field of a virtual hedgehog and anti-hedgehog, respectively. The cone size and color represents the total emergent flux through the facet, while the facet color is the flux density. The scale bars in (A) and (C) are 5 nm and 15 nm, respectively.

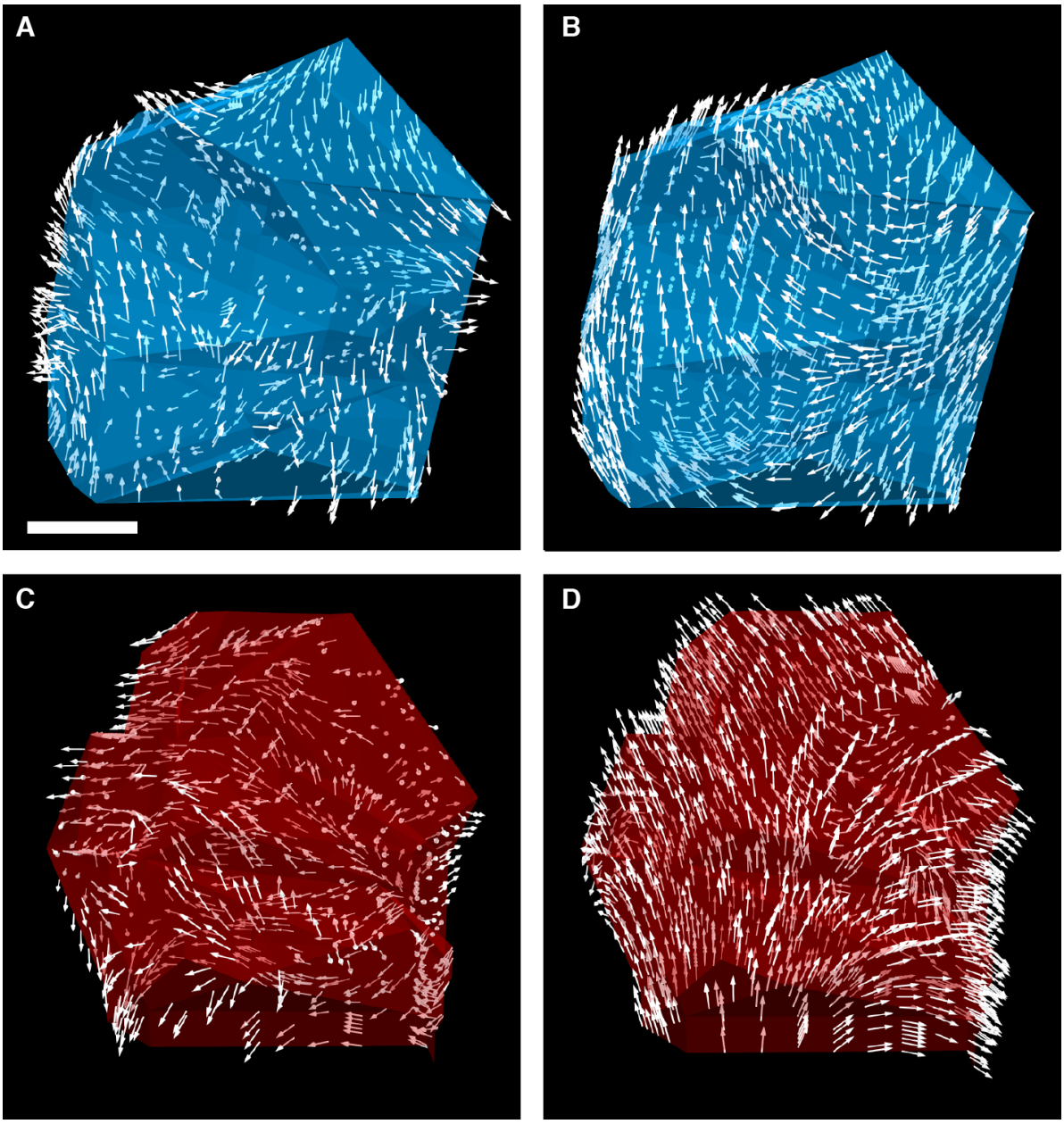

Figure 3.S8. Topologically non-trivial voids in experimental reconstruction and micromagnetic simulation. **(A)** The same experimentally reconstructed void surface shown in fig. 3.4A ($\mathcal{Q} = -0.99$). **(B)** The same void surface shown in (A) with the magnetization texture obtained from micromagetic simulation ($\mathcal{Q} = -0.99$). **(C)** The same experimentally reconstructed void surface shown in fig. 3.4C ($\mathcal{Q} = +0.96$). **(D)** The same void surface shown in (C) with the magnetization texture obtained from micromagetic simulation ($\mathcal{Q} = +0.95$). Scale bar, 15 nm.

Location	N_+	N_-	N_{total}
Octahedral	44	46	**90**
Tetrahedral/Bond	20	19	**39**
N/A	4	5	**9**

Table 3.S1: **Hedgehog location categorized by meta-atom type.** The number of hedgehogs (N_+) and anti-hedgehogs (N_-) found in the three structural components of a metalattice (octahedral meta-atom, tetrahedral meta-atom, meta-bond). Hedgehogs located in an ambiguous location are listed in the third row.

CHAPTER 4

Conclusion

This dissertation contains recent developments which leverage fundamental light-matter interactions to extend the information retrieval capabilities of CDI beyond the charge density at a single wavelength.

4.1 Summary

The first work proposes a broadband ptychographical reconstruction algorithm in the context of attosecond imaging. Incoherence has been an obstacle to conventional imaging, but in this work we turn in into a strength by being able to separate individual spectral modes and harness all of the available flux. The use of modified constraints in a ptychography framework in combination with denoising techniques allows for high quality reconstructions, even when the bandwidth approaches 100%. When attosecond imaging is demonstrated in an experimental setting, it will be a big leap forward both for imaging and ultrafast science.

The second work demonstrates that XMCD, optimized in the soft x-ray regime, can be used to reveal topologically non-trivial states in a geometrically confined ferromagnet. Recent developments in chemical fluid deposition allowed for the fabrication of high quality metalattices on the nanoscale, which had been theoretically investigated nearly 20 years ago. Using the novel vector RESIRE tomography algorithm, we were able to reconstruct the native magnetization of a Nickel metalattice and rigorously determine the presence of multiple hedgehog point defects and topologically non-trivial void surfaces. We intend for

this work to serve as a foundational study for further investigation into the spin transport properties of magnetic metalattices. This work is also a demonstration of the interdisciplinary and collaborative effort that is involved to tackle problems in modern science. All aspects of this project including sample growth and fabrication, algorithm design, data acquisition, and data analysis, required collaboration between scientists across disciplines and institutions.

4.2 Outlook

The scientific frontier of CDI is two-fold—namely, to push the spatio-temporal limit and information extraction efficiency. As HHG and x-ray free electron laser technologies mature and stabilize, they will serve as vital tools for the eventual imaging of ultrafast dynamics. Other avenues for investigation are super-resolution and ankylography techniques [117–119]. Both methods aim to maximize the information extracted from diffraction measurements, the former by exceeding the conventional diffraction limited resolution, and the latter by extracting 3-D information from a 2-D measurement by accounting for curvature in Ewald's sphere. Further, recent developments in electron ptychography show it as a promising candidate for imaging low-Z elements with lower dose as compared to traditional HAADF TEM imaging [48, 120, 121]. The technique could have large impact on the scope and applicability of atomic electron tomography (AET) [122–125].

Technologically, there are challenges which present the opportunity for further interdisciplinary research. CDI would universally benefit from a directed effort to reduce the data requirements. Ptychography, and emphatically vector ptychography, being inherently data-heavy, would especially benefit from such efforts. At the time of writing, machine learning techniques are starting to invade imaging science, and may serve as a key to solving many of the data-related issues described here. Additionally, the continual improvement of beamline facilities serve to reduce data acquisition time and the non-trivial hardships of performing experiments. As in-situ and in-operando imaging experiments become more demanding and

complex, there will need to be directed efforts to develop and maintain hardware and software to make data acquisition as automated as possible.

This is an exciting time for CDI, as some of the underpinning technologies mature and others are in rapid development. While the challenges of modern science increase in complexity, so do the techniques and capabilities of the tools used to solve them. I look toward the future of CDI with curiosity and optimism.

APPENDIX A

X-ray linear dichroic ptychography

Biominerals such as seashells, coral skeletons, bone, and tooth enamel are optically anisotropic crystalline materials with unique nanoscale and microscale organization that translates into exceptional macroscopic mechanical properties, providing inspiration for engineering new and superior biomimetic structures. Using *Seriatopora aculeata* coral skeleton as a model, here, we experimentally demonstrate X-ray linear dichroic ptychography and map the c-axis orientations of the aragonite ($CaCO_3$) crystals. Linear dichroic phase imaging at the oxygen K-edge energy shows strong polarization-dependent contrast and reveals the presence of both narrow ($< 35°$) and wide ($> 35°$) c-axis angular spread in the coral samples. These X-ray ptychography results are corroborated by four-dimensional (4D) scanning transmission electron microscopy (STEM) on the same samples. Evidence of co-oriented, but disconnected, corallite subdomains indicates jagged crystal boundaries consistent with formation by amorphous nanoparticle attachment. We expect that the combination of X-ray linear dichroic ptychography and 4D STEM could be an important multimodal tool to study nano-crystallites, interfaces, nucleation, and mineral growth of optically anisotropic materials at multiple length scales.

A.1 Introduction

Humans have been using biogenic materials as tools since the dawn of humanity. Biominerals such as bone, teeth, seashells, and coral skeletons exhibit remarkable mechanical properties and complex hierarchical organization [126]. Due to these unique characteristics,

biominerals often outperform their geologic or synthetic inorganic counterparts, thus attracting significant interest in understanding the mechanisms of the biologically controlled mineralization processes for modern nanotechnology [127]. Careful understanding of the three-dimensional ($3D$) arrangement of biominerals has important engineering implications and has led to bioinspired materials that outperform nonbiomimetic, inorganic synthetic analogs [128].

One of the most common natural biominerals is calcium carbonate ($CaCO_3$), which occurs in bacteria, algae, marine organisms, and humans [129]. $CaCO_3$ absorbs light anisotropically, such that the π-bonded p orbitals of O and C atoms parallel to the crystal c axis exhibit maximum absorption when aligned parallel to linearly polarized light. The absorption intensity changes with a cos^2 law with respect to the azimuthal orientation of the carbonate groups in the crystal. This information can reveal structural and mechanical properties in $CaCO_3$ biominerals [130]. Coral biomineralization is a subject of intense studies, and the mechanisms of crystal nucleation and growth in coral skeletons are only beginning to be revealed [131–134].

The optical anisotropy in $CaCO_3$ has been leveraged in polarized visible light microscopy to study macroscopic biomineral structure and formation mechanisms [135, 136] and with imaging polarimetry to study crystal orientation uniformity [137, 138]. In the shorter-wavelength regime, X-ray absorption near-edge structure spectroscopy has been used to study the orientations of various polymorphs of $CaCO_3$ [139, 140], and polarization-dependent imaging contrast (PIC) mapping using X-ray photoemission electron microscopy (X-PEEM) has been demonstrated to quantitatively map crystal orientations in $CaCO_3$ [140–142]. Currently, PIC mapping mostly uses X-PEEM in reflection geometry to achieve tens-of-nanometer resolution. However, PEEM's limited achievable spatial resolution ($\sim$ 20 nm) and the confinement to polished two-dimensional surfaces are insurmountable limits. Scanning transmission X-ray microscopy (STXM) has taken advantage of dichroic contrast to study polymer fibers [143] to resolve 30 nm features, but it is limited in achievable spatial reso-

lution by the focusing optics, which also have a low efficiency and a short working-distance constraint.

Although macroscopic morphologies in biominerals have been studied extensively, their nanoscopic structures are still not studied routinely in a quantitative fashion, mostly due to the lack of a proper transmission microscope that offers bulk-sensitive information with spatial resolution down to the nanometer scale. With the development of high-brilliance synchrotron radiation facilities worldwide, advancements in high-resolution imaging techniques, and the increasing availability of insertion-device X-ray sources providing polarization control, such as elliptically polarizing undulators (EPUs), new synchrotron-based tools are now becoming available for probing nanoscale crystal orientation in $CaCO_3$ minerals and biominerals. By taking advantage of brilliant X-ray sources, coherent diffractive imaging (CDI) can directly achieve high-resolution structural information of noncrystalline samples and nanocrystals from their diffraction patterns [5, 38, 42–44, 144–148]. In particular, ptychography, a scanning CDI technique [38], has attracted considerable attention for its general applicability [41, 49, 149, 150]. Ptychography measures a series of diffraction patterns from spatially overlapping illumination probes on a sample, where phase-retrieval algorithms are used to iteratively recover the incident wave and complex exit wave of the sample. This versatile diffractive imaging technique has been applied to study various biological materials in two and three dimensions with high resolution [66, 151–157].

In this work, we present X-ray linear dichroic ptychography of biominerals using the aragonite ($CaCO_3$) coral skeleton of *Seriatopora aculeata* as a model. Aragonite is an orthorhombic $CaCO_3$ polymorph, with all three crystal axes being unequal in length and perpendicular to one another [126]. Carbonate crystals grow acicularly with a needle-like habit and with 10 times greater growth rate along the c axis than along the a axis [158], resulting in densely packed bundles of thin crystals in coral skeletons. It has been hypothesized that this elongated growth pattern with crystals growing mostly along the fast c axis but in all directions is the most efficient way for aragonite to fill 3D space [131].

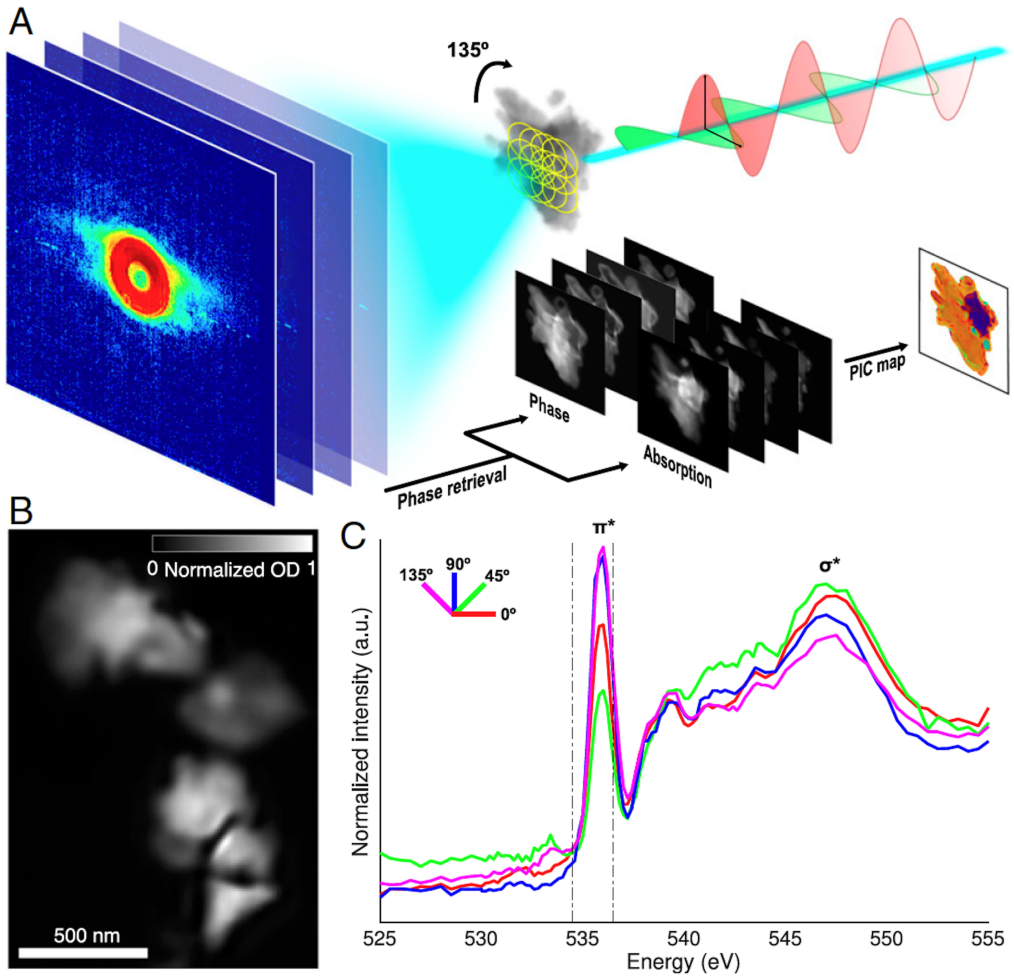

Figure A.1. Experimental schematic of X-ray linear dichroic ptychography. (A) Horizontally and vertically polarized X-rays incident on the specimen as spatially overlapping diffraction patterns were acquired below (534.5 eV) and on (536.5 eV) the *O K*-edge absorption edge to obtain 0° and 90° polarization data. The sample was then rotated 135° and measured again to obtain the 45° and 135° data. The diffraction patterns were directly phased to obtain high-resolution polarization-dependent ptychographic images, from which absorption images were used to compute the PIC maps.(B) Ptychography absorption image of a coral particle used to collect linear dichroic absorption spectra. (C) Experimental XAS spectra of the coral particle at four polarizations, showing the dependence of the $CaCO_3$ π^* peak intensity on the incident X-ray polarization angle. A.u., arbitrary units; OD, optical density. *(Figure reprinted from [68])*

Consequently, this space-filling strategy may endow a unique evolutionary advantage to host organisms that adhere to the pattern by providing greater resilience to environmental stresses such as ocean acidification [159]. Therefore, the exact nanoscopic mechanisms of biomineral growth along various crystal axes are of significant scientific interest in understanding the macroscopic structural changes in coral species around the world.

We imaged several coral-skeleton samples on and off the O K-edge π^* peak and observed significant contrast differences between absorption and phase images. Using three linear dichroic ptychography images, we performed PIC mapping to quantitatively determine crystal c-axis orientations in the coral with 35 nm spatial resolution. Our dichroic ptychography results were qualitatively validated by correlating the ptychography PIC maps with four-dimensional (4D) scanning transmission electron microscopy (STEM), a scanning nanoelectron diffraction technique for probing crystal orientations in crystalline materials [160]. We observed that, at the nanoscale, crystallite orientations can be narrowly distributed, as is characteristic of spherulitic crystals, but also randomly distributed in submicrometer particles. Moreover, we verified linear dichroic phase contrast at a pre-edge energy below the absorption resonance. The use of such phase contrast may lead to new dose-efficient dichroic imaging techniques for studying anisotropic biominerals and has important implications for understanding the nanoscale organization of crystallites in biominerals.

A.2 Results

X-ray linear dichroic ptychography

Soft X-ray ptychographic microscopy measurements were performed at the imaging branch of the undulator beamline, COherent Scattering and MICroscopy (COSMIC), at the Advanced Light Source (ALS) [161, 162]. COSMIC provides monochromatic soft X-rays with energies variable from 250 to 2500 eV, spanning the carbon and sulfur K-edges. Coherent and monochromatic X-rays were focused onto the sample by using a Fresnel zone plate, with

45 nm outer zone width and a total coherent flux of $\sim 10^9$ photons/s at the sample position. The transmission electron microscopy (TEM) grid containing the *S. aculeata* coral-skeleton sample was secured by using a Hummingbird 3 mm half-grid tip (*Materials and methods*) and then mounted onto a standard FEI CompuStage sample manipulator derived from an FEI CM200 series TEM. Diffraction data were recorded with a 1000 frame-store charge-coupled device (CCD) [163]. Diffraction patterns were acquired without a beam stop and were automatically preprocessed onsite.

Ptychographic measurements consisted of single diffraction patterns recorded at each scan point with 200 or 300 ms dwell time and scanned in a square grid with 40 nm steps to cover a $\sim 1.5 \times 1.5$ μm field of view, with a reconstruction pixel size of 10.1 nm / pixel. Linear dichroic ptychography data were collected at 0°, 45°, 90°, and 135° linear polarizations. The 0° and 90° data were collected with the EPU tuned to horizontal and vertical polarizations, respectively. Since, at the time of these measurements, only linear horizontal and vertical polarizations were under remote computer control, the TEM grid was physically rotated clockwise in-plane by $\sim 135°$ with respect to the upstream beam, and then the 45° and 135° data were collected by using the horizontal and vertical polarizations again.

The same linear dichroic data with four polarization angles were collected at two X-ray energies around the O K-edge π^* peak: one pre-edge (at 534.5 eV, or 1.5 eV before the π^* peak) and another on-peak (at 536.5 eV, or 0.5 eV after the π^* peak maximum). The pre-edge energy was estimated to be near the negative phase peak and, thus, had the most negative phase shift relative to vacuum to achieve optimal phase contrast. The on-peak energy was chosen to be slightly off the maximum absorption peak at 536 eV to reduce beam absorption and attenuation caused by specimen thickness. The resonant energy at the O edge rather than the C edge was chosen in this study because the $3:1$ ratio of O to C in $CaCO_3$ means imaging at O resonance gives three times higher signal-to-noise ratio and contrast. After all data were acquired, ptychography reconstructions were performed by using a regularized ptychographic iterative engine [108] with 300 iterations, with $\beta_{obj} = 0.7$ and $\beta_{probe} = 0.7$,

and updating the initial probe only after the 100^{th} iteration.

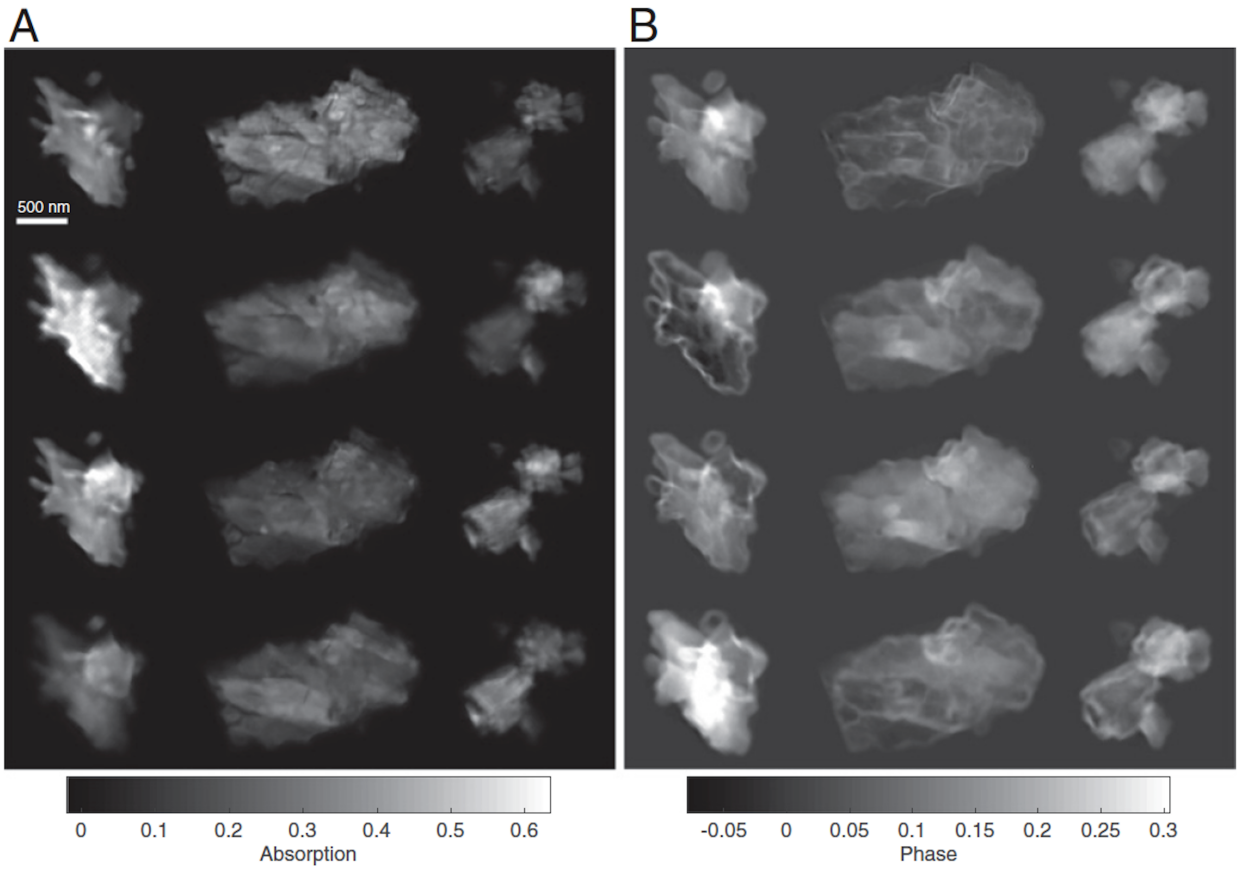

Figure A.2. X-ray linear dichroic ptychography of coral-skeleton particles. (A) Ptychography absorption images of three aragonite particles ($P1$, $P2$, and $P3$, from left to right) recorded on the O K-edge absorption resonance at 536.5 eV (Fig. A.1C), across four linear polarizations (top to bottom: 0°, 45°, 90°, and 135°), showing strong polarization-dependent absorption contrast and revealing nanoscale morphologies ranging from smooth homogeneous particles several hundred nanometers in size to sub-100 nm fine features. (B) Ptychography phase images of the same particles and polarizations recorded at an energy slightly before O K-edge absorption edge of 534.5 eV (Fig. A.1C), showing strong polarization-dependent phase contrast and more edge-sensitive features in internal coral structures. *(Figure reprinted from [68])*

Fig. A.1 shows the experimental schematic of the linear dichroic X-ray ptychography experiment. Fig. A.1C shows the O K-edge spectra obtained from STXM with X-ray absorption spectroscopy (XAS) at each linear polarization (*Materials and methods*), showing the expected dependence of X-ray absorption on the relative angle between crystal c-axis and X-ray polarization [140]. The π^* peak absorption occurs around 536 eV and is maximum when X-ray polarization is parallel to the π orbitals of C and O in the trigonal planar carbonate group. The broad σ^* peak occurs around 547 eV and is anticorrelated with the π^* peak.

To study the effects of linear dichroism on the absorptive component of the coral's complex exit wave, we imaged three coral particles at two energies, pre- and on-peak. Fig. A.2A shows on-peak ptychography absorption contrast images of three coral particles at 0°, 45°, 90°, and 135° polarizations from top to bottom, and the particles are denoted from left to right as $P1$, $P2$, and $P3$, respectively. Relative contrast within the particles changes dramatically with polarization, signifying the presence of differently oriented nanoscale domains in each particle. $P1$ displayed overall smooth features with little internal structures, whereas $P2$ and $P3$ contained multiple nanodomains and striations. While resonant imaging revealed rich polarization-dependent absorption contrast due to the linear dichroism, imaging off resonance produced no absorption contrast when varying polarizations (Fig. A.S3A).

To examine the effects of linear dichroism on the phase component of the complex exit wave of the coral-skeleton particles, we also measured ptychographic images at 534.5 eV (Fig. A.2B), an energy slightly before the π^* peak. In general, the negative phase peak is at lower energy than both the positive phase peak and the absorption peak and provides the greatest contrast with respect to nonresonant material [164]. Phase-contrast images revealed sharp boundaries and complex surface morphologies in the particles. On the other hand, on-edge phase images of the coral particles revealed polarization-dependent contrast that agreed very well with on-edge absorption images (Fig. A.S3B). According to the Kramers–Kronig relation, the effects of linear dichroism in crystal orientation manifest in both components

of the complex refractive index. But as we observed in ptychographic maps, while the effect on absorption was significant on resonance (Fig. A.2A), the effect on phase was maximum off resonance (Fig. A.2B). Resolution of the ptychographic images was estimated to be 35 nm by using the knife-edge method with 10 to 90% intensity cutoff (Fig. A.S4). Given a mass attenuation coefficient (μ/ρ) of 2×10^4 cm^2/g for $CaCO_3$ on O K-edge and an $\sim 50\%$ overlap, each recorded projection absorbed an estimated dose of 1.44×10^8 Gy. At this dose and estimated resolution, no noticeable deterioration was observed in the sample [165].

PIC mapping

Ptychographic PIC mapping revealed that the orientations of crystals were much more diverse at the nanoscale than previously appreciated (*Materials and methods*). As is clear from Fig. A.3, and, in particular, from the broad range of colors in the three particles in Fig. A.3A and the large width of the histograms in Fig. A.3B, many crystallites were present in what was previously assumed to be single crystals (e.g., $P2$) or two crystals (e.g., $P1$). These crystallites varied in orientation gradually, as displayed by color gradients across all larger domains, as in the mustard-color domain of $P1$, the green-blue domain of $P2$, or the yellow-red-blue domain of $P3$. There were also unexpected, smaller ($\sim$ 100 nm) domains with orientation different from the larger domain, but not randomly oriented as expected from sample preparation artifacts, e.g., randomly aggregated particles. These small domains were co-oriented with one another, but spatially separate from one another. Other smaller domains in $P2$ were the red-dot crystallites near the edges. $P3$ shows several blue-green crystals of similar smaller sizes and orientations, that are interspersed with the rest of the particle shown as yellow-red-yellow. These nano-crystallites are highly surprising, as they were not revealed by previous methods, such as PIC mapping using X-PEEM in previous work [131, 134] or in this work in Fig. A.S5. PEEM-PIC mapping shows that the smaller crystalline domains in the centers of calcification are randomly oriented in *Seriatopora aculeata* coral skeletons (Fig. A.S5). Ptychographic PIC mapping, instead, shows that several smaller ($\sim$ 100 nm)

crystallites are misoriented with respect to the larger crystal domains in which they are embedded, but co-oriented with one another (Fig. A.3A).

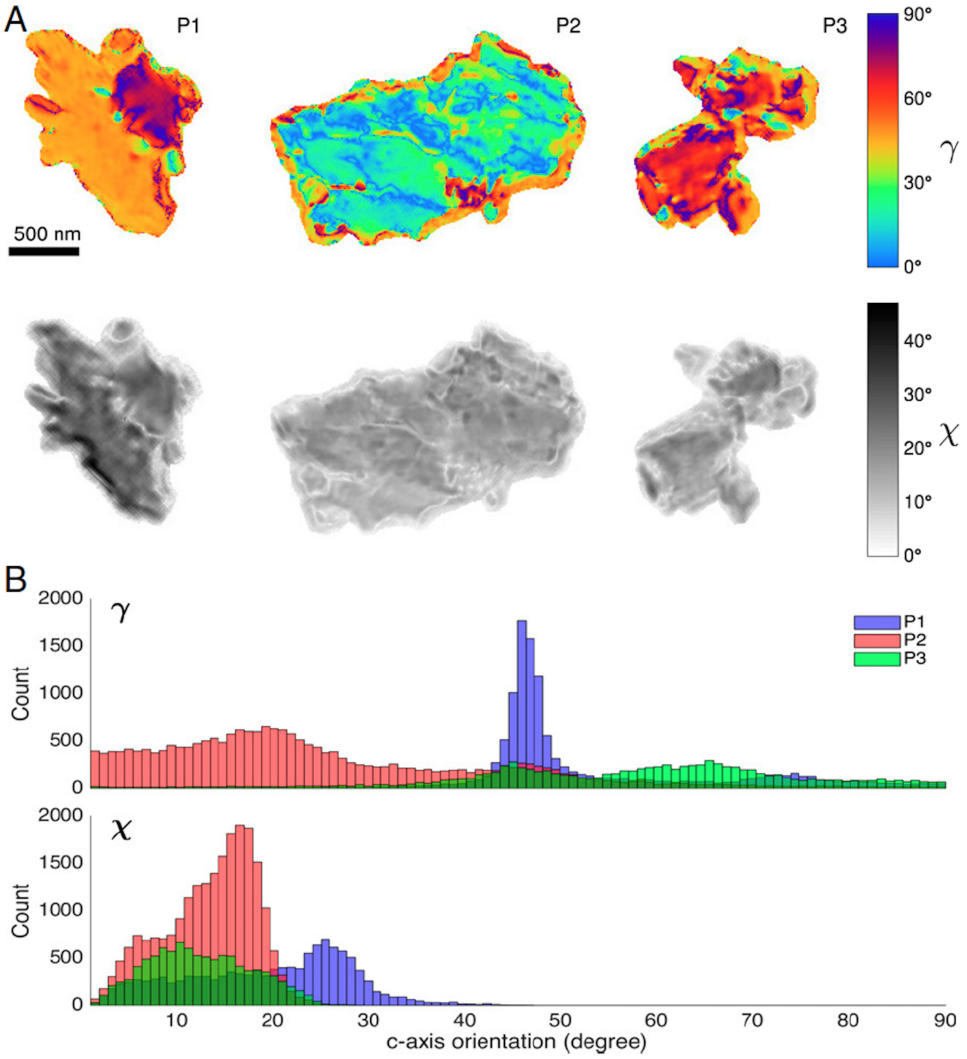

Figure A.3. Ptychography PIC map of aragonite coral-skeleton particles. (A) Quantitative PIC maps of the three aragonite particles, calculated using 0°, 45°, and 90° linear dichroic ptychography images. Hue (Upper) denotes in-plane azimuthal crystal c-axis angle (γ) of the crystallite, while brightness (Lower) denotes out-of-plane c-axis angle (χ), all ranging from 0° to 90°. $P1$ consists of mostly homogeneous orientations, whereas $P2$ and $P3$ show more orientational diversity. (B) Histograms of in-plane (γ; Upper) and out-of-plane (χ; Lower) angles for the three particles, showing a narrow γ angular spread ($< 35°$) for $P1$ and broader spread ($> 35°$) for $P2$ and $P3$, suggesting the presence of both spherulitic and randomly oriented submicrometer crystallites at the nanoscopic scale. *(Figure reprinted from [68])*

To better understand the co-oriented smaller domains, we performed PIC mapping on the on-edge linear dichroic ptychography absorption images to quantitatively map c-axis angles in the coral particles and analyzed the in-plane (γ) and out-of-plane (χ) c-axis orientation angles (*Materials and methods*). The PIC maps in Fig. A.3A were calculated by using the 0°, 45°, and 90° polarization images, and a second set of PIC maps was computed by using 0°, 135°, and 90° polarization images (Fig. A.S6). In each PIC map, in-plane angles are color-coded according to the coral's crystal axes relative to the X-ray polarization, which is horizontal at 0°. Orientation ranges from 0° to 90°, since angles beyond that range are degenerate and cannot be distinguished from contrast alone. The out-of-plane angles between the c-axes and X-ray polarization are represented by brightness, such that c-axes aligned with the imaging plane are displayed with high brightness, and c-axes that are perpendicular to the imaging plane are shown in low brightness, and are lowest when the axes align directly with the X-ray beam.

Histograms of γ (Upper) and χ (Lower) in Fig. A.3B present the c-axis angular distribution derived from the PIC maps. $P1$ exhibits two distinct subdomains, within which the angular spread is $< 35°$, but these are oriented more than 35° apart from one another. In contrast, $P2$ and $P3$ show greater submicrometer orientational fluctuations that span more than 35°, suggesting that particles $P2$ and $P3$ comprise many differently oriented nanocrystals from the centers of calcification. To examine the abrupt orientational change between subdomains in $P1$, we performed electron tomography on the same $P1$ particle (*Materials and methods*), which revealed two separate particles on top of each other and, thus, confirmed the ptychography results (Fig. A.S7).

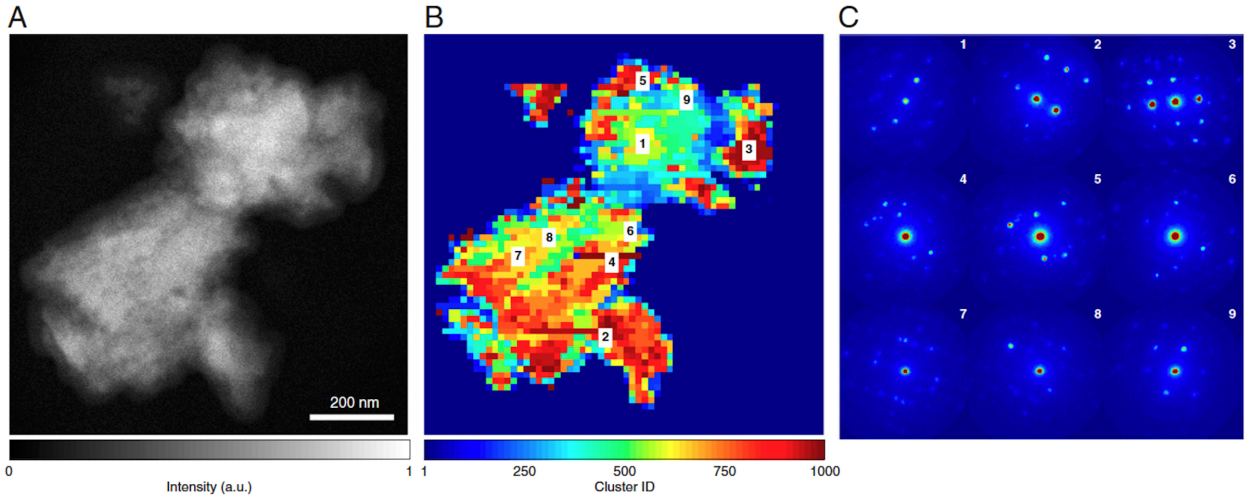

Figure A.4. Diffraction similarity map from 4*D* STEM with hierarchical clustering. (A) STEM image of particle *P*3, which was used to acquire scanning electron nano-diffraction patterns. (B) Crystal axis similarity map generated using hierarchical clustering of diffraction patterns. Areas with comparable color resemble subdomains with similar crystal orientations. The resulting map qualitatively agrees with the PIC map generated from ptychography PIC mapping (*P*3 in Fig. A.3). (C) Representative CBED patterns from various regions of the coral particle, co-labeled in B and C, showing nanoscale orientational diversity. (Scale bar, 200 nm.) A.u., arbitrary units. *(Figure reprinted from [68])*

The 4D STEM and clustering analysis

To validate the localization and orientation of crystallites observed in ptychographic PIC maps, we performed a 4D STEM experiment on particle $P3$ and assessed its nanoscale lattice changes over the entire particle (*Materials and methods*). The converging beam electron diffraction (CBED) patterns were analyzed by using unsupervised agglomerative hierarchical clustering to sort the particle into different regions with similar crystal orientations [166]. Fig. A.4A and B show a STEM image of $P3$ and the resulting similarity ranking map generated by hierarchical clustering, respectively. The closer the regions are in color, the more similar their corresponding CBED patterns are. Representative CBED patterns from the coral skeleton are shown in Fig. A.4C, with numbers corresponding to the labeled regions in Fig. A.4B.

The CBED patterns reveal variations and similarity in diffraction—hence, crystal orientations—across the particle. For instance, pattern 1 is similar to pattern 9, and both are in close proximity to one another. In contrast, patterns 4 and 6, although within the same region, have dissimilar diffraction patterns. Moreover, the similarity ranking map divides the particle $P3$ into subregions closely resembling those shown in the ptychographic PIC map in Fig. A.3A. In particular, distinct subdomains in regions 2, 3, 4, and 7 of the similarity ranking map match well with the corresponding areas in the ptychographic PIC map. This result serves as further confirmation of the orientation heterogeneity within $P3$.

A.3 Discussion

X-ray linear dichroic ptychography of coral particles shown in Fig. A.2 unveils strong polarization-dependent absorption and phase contrast that are evidence of differently oriented subdomains in each particle. Moreover, each particle exhibits diverse structural features and contains crystal-orientation domains that range in size from tens to hundreds of nanometers. While both on-edge absorption and pre-edge phase images reveal fine internal

features in the coral-skeleton particles, phase images are more sensitive to edges and, thus, show surface morphologies and boundaries more clearly. The use of phase information to visualize weakly scattering fine features has previously been demonstrated with visible light-phase ptychography to enhance cellular contrast in live cells [167]. In the case of biominerals, the simultaneous phase and absorption contrast imaging provided by X-ray ptychography can be used to probe nanoscale boundary features beyond the surface, enabling structural study of intercrystal topology that is critical in understanding biomineral nucleation and growth. This is a demonstration of combined linear dichroic absorption and phase imaging of optically anisotropic materials.

The orientations observed in the main domains of each particle are $< 35°$, as previously observed [131, 159, 168], and are consistent with spherulitic crystals [131]. PIC maps generated from the X-ray linear dichroic ptychography images (Fig. A.2 and Fig. A.S3) provide quantitative crystal-orientation information with high resolution and at a depth on the order of 100 to 500 nm, which is not available with the 5 nm surface-sensitive X-PEEM PIC mapping (Fig. A.S5). At the fine-grain level, the ptychographic PIC map of $P1$ shows the presence of two overlaid homogeneous particles, each having a c-axis angular spread of $< 35°$ (Fig. A.3B). Such narrow angular spread is typical of spherulitic crystal such as those that form all coral skeletons, fills space isotropically with anisotropic crystals, and thus provides the coral skeleton with the needed structural support [131, 134].

Similarly, the main crystalline domains in all three particles, $P1$, $P2$, and $P3$, are co-oriented within $35°$, as expected from spherulitic crystals. But, surprisingly, all three particles exhibit several smaller ($\sim$ 100 nm) domains differently oriented with respect to the main domain (Fig. A.3). Since the orientations of these smaller domains are not random, but co-oriented with one another, these crystallites cannot be the randomly oriented nanocrystals termed sprinkles observed at growth fronts in some coral species [134] or in CoC in others such as *Acropora* sp. [134], including *Seriatopora aculeata* studied here (Fig. A.S5). These smaller co-oriented domains in corals have not been observed with such detail before,

presumably because previous studies did not have the capability to detect bulk subdomain morphology. Evidence of such co-oriented, disconnected corallites cannot be easily explained by current models for coralskeleton formation [132, 169, 170]. Although additional evidence is needed to fully understand the source and formation mechanism of the observed co-oriented, disconnected crystallites, any model for coral-skeleton growth must be consistent with their formation.

The X-ray linear dichroic ptychography results presented in this work imply an important possibility. Conventionally, enhanced polarization-dependent contrast is derived from absorption contrast when imaged on elemental absorption edges, with the trade-off being that more energy is deposited into the sample per unit area and time, which inevitably exacerbates sample radiation damage. However, as this work has demonstrated, one major benefit of X-ray linear dichroic ptychography is that strong polarization-dependent phase contrast is also available when imaged at the off-resonant energy. Benefits of off-resonance, dose-efficient imaging have been reported [164, 171], in which the large phase shifts and strong energy dependence near atomic resonances play an important role in achieving high spatial resolution. It was observed that the maximum resolution peak falls at the energy of the most negative phase shift relative to vacuum, which yields the maximum phase contrast relative to the nonresonant material and points to phase contrast being a primary driver in ptychographic image resolution.

Altogether, our study indicates that linear dichroic phase-contrast imaging offers an alternative path to obtaining quantitative crystal-orientation insights without having to subject the sample to the same radiation dose as absorption-edge imaging. This potentially important finding can enable more sophisticated and data-intensive studies. Such dose-efficient technique will be especially advantageous when applying vector ptychographic tomography to biomaterials [172, 173], since many tilt projections are needed to achieve a high-quality 3D reconstruction. So far, most linear dichroism studies focused on absorption, because linear phase dichroism was difficult to obtain experimentally. Thus, X-ray linear dichroic phase

ptychography has the potential to become an important tool for studying dose-sensitive materials.

A.4 Conclusion

In this work, we present an experimental demonstration of X-ray linear dichroic ptychography. By imaging three *S. aculeata* coral-skeleton particles at pre- and on-peak *O K*-edge energies, we observed strong polarization-dependent phase and absorption contrasts. We performed PIC mapping on the dichroic ptychography absorption images to quantitatively estimate *c*-axis orientations in the corals and observed the presence of two types of previously known crystallites: a main domain in each particle with narrow angular spread $< 35°$ consistent with spherulitic crystals and with the randomly oriented submicrometer nanocrystal domains observed in the centers of calcification of *Acropora* coral skeletons [134]. Furthermore, we observed $\sim$ 100 nm crystallites misoriented with respect to the main domains in each particle, but co-oriented with one another, disconnected, and interspersed with and within larger crystals. We validated the X-ray dichroic ptychography results with 4D STEM and confirmed that regions of orientational diversity are largely consistent. The observation of strong linear phase dichroism off the absorption edge offers the potentially interesting possibility of using phase imaging rather than absorption imaging in future linear dichroism studies as a way to alleviate sample radiation damage. Although we used coral samples as a proof-of-principle in this work, we anticipate that X-ray linear dichroic ptychography can be coupled with 4D STEM and spatially resolved X-ray scattering [174] to study a wide range of optically anisotropic materials such as tooth enamel [175], bone [174], seashells [176], brittlestars [177], and polymers [143] at multiple length scales.

A.5 Materials and methods

S. aculeata skeleton preparation

The *S. aculeata* coral skeleton used in this study was a pencil-thick, short, and tapered branch, termed a nubbin (Fig. A.S1). An entire *S. aculeata* coral skeleton, $\sim 10 \times 10 \times 10$ cm^3 in size, was purchased from Tropical Fish World. To remove the tissue and obtain a clean aragonite skeleton, the living coral was immersed in 5% sodium hypochloride in water (Chlorox). After 7 d of bleaching, the skeleton was washed twice in double-distilled H_2O for 5 min and twice in ethanol for 5 min. An ~ 1 cm-long nubbin was broken off from the rest of the coral skeleton, placed in an agate mortar, and immersed in 100% ethanol, then gently fractured by an agate pestle into micrometer-sized grains. The resulting ethanol suspension was sonicated for 2 min for further dispersion, and the supernatant solution was transferred by pipette onto a 200 mesh copper TEM grid coated with carbon film and air-dried for 24 h before data acquisition.

XAS

STXM-XAS was measured at ALS beamline 7.0.1.2. The spectromicroscopy data were recorded with 5 ms dwell time and proceeded with 60 nm steps in a square grid scan, with energies spanning the entire O K-edge from 525 to 555 eV. Energy-scan steps proceeded with 0.5 eV steps from 525 to 530 eV, then 0.2 eV from 530 to 542 eV, and, finally, with 0.5 eV steps from 542 to 555 eV. The same energy-scan parameters were repeated for X-ray linear polarizations at 0°, 45°, 90°, and 135°). All spectra were normalized via subtraction of the average image from nonresonant energies from 525 to 530 eV.

X-ray absorption spectra were generated by using the MANTiS software [178]. STXM-XAS images at each linear polarization were first converted to optical densities by using fully transmitting regions in the specimen, then aligned by using cross-correlation. Principal

component analysis was used to reduce the dimensionality of spectral information in the images to obtain absorption signatures of the coral. The first principal component spectrum at each polarization, which represents the average absorption present in the coral, is shown in Fig. A.S2.

Ptychographic PIC mapping

Crystallographic c-axis orientations in coral particles were calculated by using PIC mapping [141], a method that uses linear dichroism effects to quantitatively determine the angular orientation of microcrystals and nanocrystals. We used the closed-form expression to compute the in-plane angle, χ, and out-of-plane angle, γ, of the crystal c axis with respect to the linear polarization vector. Here, in-plane is defined as the TEM grid plane that is perpendicular to the X-ray beam. Given three EPU polarization angles, 0°, 90°, and 45°, the electric field vectors at each polarization were $\vec{E}_1 = E_0\hat{\mathbf{x}}$, $\vec{E}_2 = E_0\hat{\mathbf{y}}$, and $\vec{E}_3 = \left(\vec{E}_1 + \vec{E}_2\right)/\sqrt{2}$, where $\hat{\mathbf{x}}$ and $\hat{\mathbf{y}}$ are unit vectors. The unit vector describing the c-axis orientation is $\hat{\mathbf{c}} = \hat{\mathbf{x}}sin\chi cos\gamma + \hat{\mathbf{y}}sin\chi sin\gamma + \hat{\mathbf{z}}cos\gamma$. For the i^{th} polarization, the signal intensity was $I_i = I_A + I_B\left(\vec{E}_i \cdot \vec{c}\right)$, where I_A and I_B are positive fitting parameters. Algebraic manipulations of the three components yield

$$cos^2\gamma = \frac{1}{2} + \frac{I_1 - I_2}{2\left[(I_1 - I_2)^2 + (I_1 + I_2 - 2I_3)^2\right]^{1/2}}\ , \tag{A.1}$$

$$sin^2\chi = \frac{1}{I_B}\left[(I_1 - I_2)^2 + (I_1 + I_2 - 2I_3)^2\right]^{1/2}\ . \tag{A.2}$$

Solving for γ and χ in the above equations gives the in-plane and out-of-plane c-axis angles, respectively. The range of χ contracts and expands as I_B varies, but the relative difference in χ between particles remains consistent. In this work, I_B was arbitrarily set to two. Since ptychography data at four EPU linear polarizations were collected, two sets of polarizations were used to calculate two PIC maps for each coral particle: the first set used 0°, 45°, and 90°, and the second set used 0°, 135°, and 90°.

PEEM-PIC mapping

The PIC maps were acquired by using the PEEM-3 instrument on Beamline 11.0.1.1 at ALS. Nine partly overlapping 60 $\mu m \times 60$ μm PIC map data were acquired and then tiled and blended in Photoshop. For each PIC map, a stack of 19 PEEM images was acquired on-peak at the O K-edge π^* energy as the linear polarization from the undulator was rotated from 0° to 90° in 5° increments. The 19 images were mounted as a stack and analyzed for fully quantitative crystal-orientation information in each 60 nm pixel by using the GG Macros in Igor Pro Carbon. As coral skeletons are made of $< 99.9\%$ aragonite ($CaCO_3$) and $< 0.1\%$ organic matrix [179], the contribution of organics to oxygen spectroscopy is $\ll 0.1\%$, which is not expected to exhibit any polarization dependence. Thus, PIC mapping in ptychography or PEEM only displays aragonite crystal orientations.

The 4D STEM and electron tomography

The 4D STEM and electron tomography data were collected at the National Center for Electron Microscopy, Molecular Foundry, Lawrence Berkeley National Laboratory. Both methods were used on the same three samples already analyzed with ptychography. A Titan $60-300$ equipped with an Orius 830 detector (Gatan) and four windowless silicon drift energy-dispersive detectors (FEI super-X) were used with a solid angle of 0.7 srad. The microscope operated in STEM mode at 200 kV with an electron-beam current of ~ 16 pA for $4D$ STEM datasets and ~ 40 pA for STEM imaging. The 4D STEM diffraction patterns were taken on an Orius CCD with a camera length of 300 mm using a convergence angle ~ 0.51 mrad, with 64×64 square grid scan positions. Before clustering of 4D STEM data, individual diffraction patterns were preprocessed by aligning the center of mass of the main beam to the image center to correct for horizontal and vertical shifts introduced by beam tilt.

A diffraction-similarity map was generated by using agglomerative hierarchical cluster-

ing [166] of 4D STEM data. Agglomerative hierarchical clustering initialized all data points, or individual diffraction patterns, as independent clusters. The algorithm then computed the proximity between every pair of data points using a specified distance metric (e.g., Euclidean distance, cosine similarity, or correlation). Next, pairs of data points were linked to one another by using a specified linkage metric (e.g., average distance, centroid distance, or nearest-neighbor distance) to form new grouped clusters and repeated until all data points were linked together into a hierarchical tree. Finally, the consistency of the resulting clusters was verified by evaluating the distances between each pair of neighboring clusters in the tree. A distance that was greater than a predefined inconsistency score constituted a natural partition between clusters, such that separate clusters were considered to be truly independent. This clustering was performed in a MATLAB (MathWorks) environment with the "linkage" function, using correlation as the distance metric, nearest neighbor as the linkage metric, and an inconsistency score of 1.2 .

Electron tomography was performed by using the GENeralized Fourier Iterative REconstruction (GENFIRE) [180], an algorithm that has been used to determine the 3D and 4D atomic structure in materials with unprecedented detail [125, 181, 182]. Before reconstruction, STEM projections were aligned to a common tilt axis by using the center-of-mass and common-line methods [122]. Next, a constant background—the average value in an empty region of the image—was subtracted from each projection, and the process was optimized by minimizing the differences between all common lines and a reference common line. The projections were then normalized to have the same total sum, since the integrated 3D density of the isolated coral particle should be consistent across all tilt angles. The preprocessed projections were used in GENFIRE reconstruction, which ran for 100 iterations with an oversampling ratio of two [3], 0.7 pixel interpolation distance, and the enforcement of positivity and support constraints.

Data availability

X-ray linear dichroic ptychography data presented in this work are available for download at the Coherent X-Ray Imaging Data Bank (https://www.cxidb.org/id-109.html), and electron tomography data presented in this work are available for download at Mendeley Data (https://data.mendeley.com/datasets/f62bfbndym/1). All data needed to evaluate the conclusions in the paper are present in the paper and/or supplemental figures A.6.

Acknowledgements

We thank Marcus Gallagher-Jones for guidance on 4D STEM analysis and Jared J. Lodico and Billy A. Hubbard for help handling the samples during the ptychography experiments at COSMIC. We thank NVIDIA Corporation for the donation of the Quadro K5200 GPU used for this research. This work was primarily supported by STROBE: A NSF Science & Technology Center under Grant DMR 1548924. The 4D STEM and electron tomography work were supported by the Department of Energy (DOE), Office of Science, Basic Energy Sciences (BES), Division of Materials Sciences and Engineering Award DE-SC0010378. P.U.P.A.G. received 40% support from DOE–BES–Chemical Sciences, Geosciences, Biosciences–Geosciences Grant DE-FG02-07ER15899, 40% support from the Laboratory Directed Research and Development (LDRD) program at Berkeley Lab, through DOE-BES, under Award Number DE-AC02-05CH11231, and 20% support from NSF Biomaterials Grant DMR-1603192. All X-ray experiments were done at the ALS, which is supported by the Director, Office of Science, BES, DOE Contract DE-AC02-05CH11231. The 4D STEM and electron tomography experiments were performed at the Molecular Foundry, which is supported by Office of Science, BES, DOE Contract DE-AC02-05CH11231. The electron tomography data were based on high-angle annular dark-field STEM images. D.M. was supported by the DOE National Nuclear Security Administration Stewardship Science Graduate Fellowship program, which is provided under Grant DENA0003864.

A.6 Supplemental figures

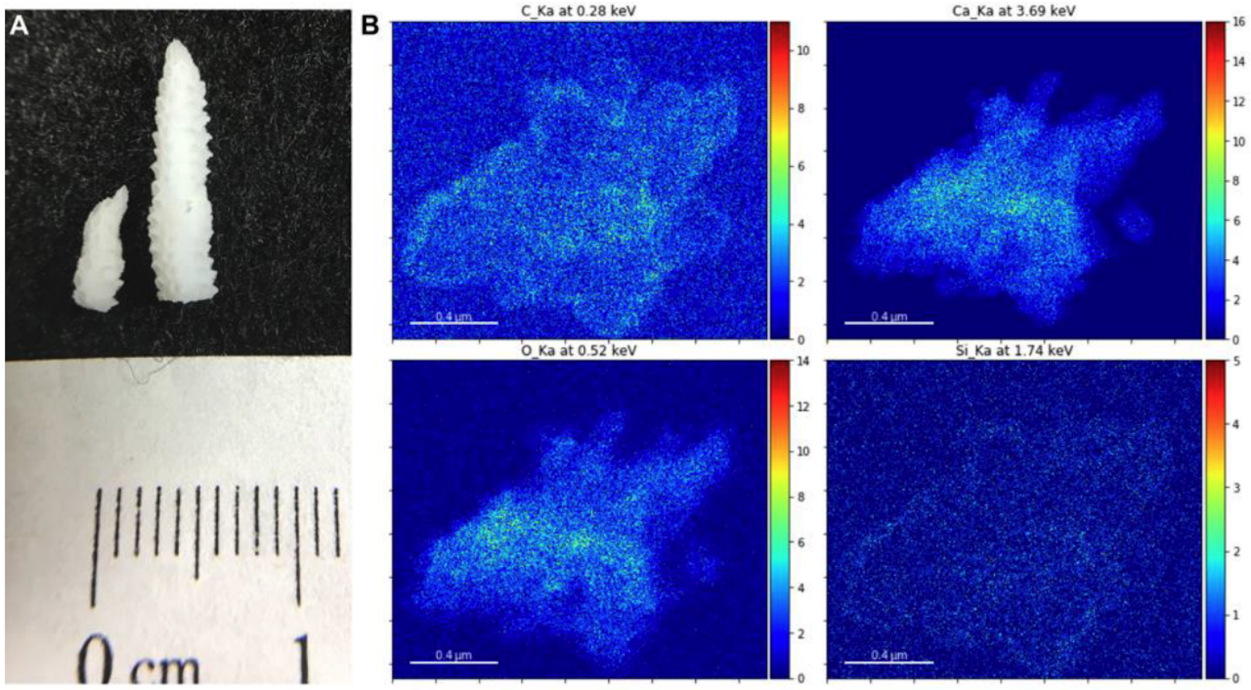

Figure A.S1. *Seriatopora aculeata* coral skeleton. (A) Bulk *S. aculeata* coral skeleton specimen from which micrometer-sized particles were milled and extracted for x-ray and electron measurements. (B) Energy dispersive spectroscopy of a coral particle, showing spectral images of 4 major elements in the particle and confirming aragonite's predominant composition of C, Ca and O, with some slight Si contamination. *(Figure reprinted from [68])*

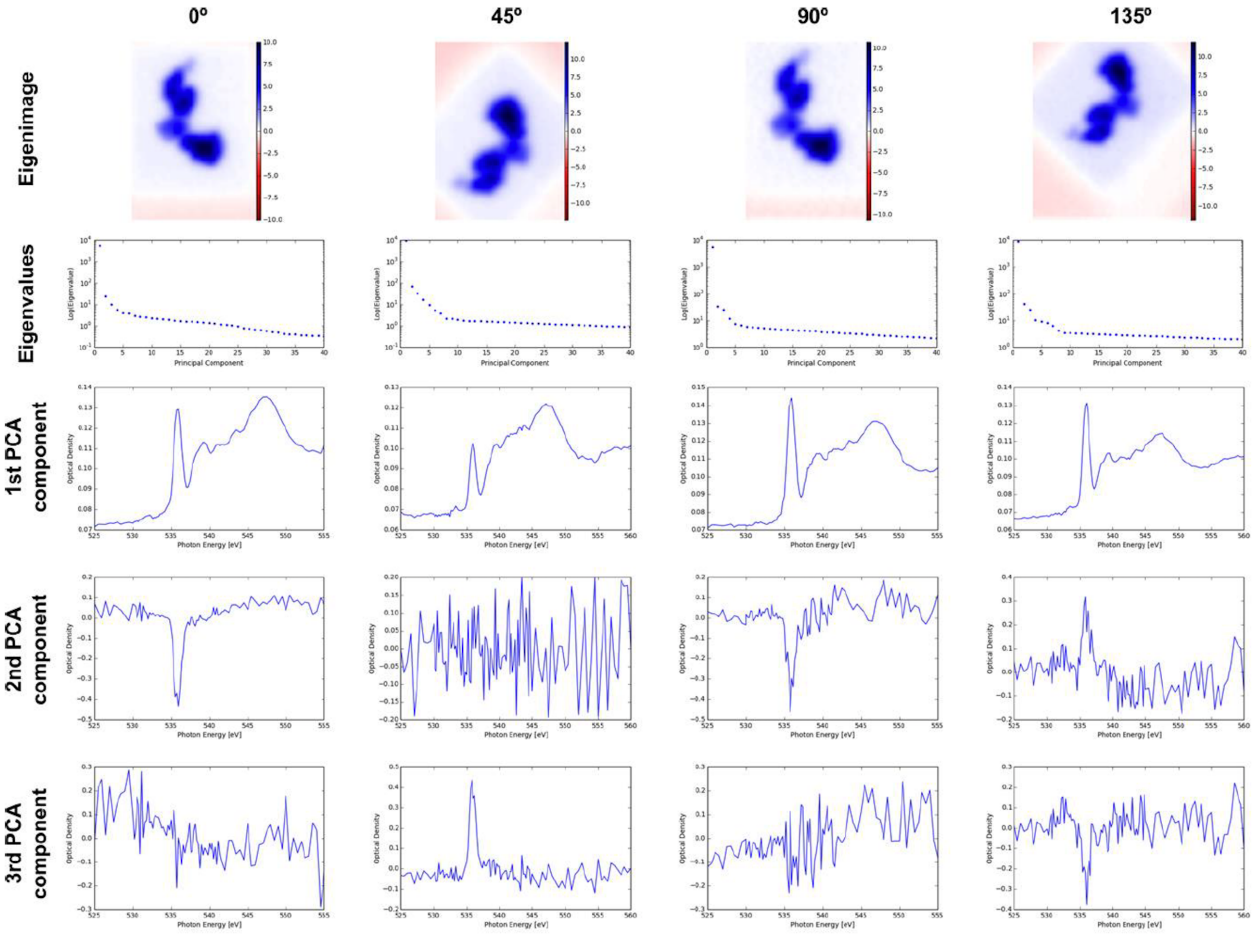

Figure A.S2. STXM-XAS spectral decomposition. First row: First eigenimages of the coral skeleton at each linear polarization, representing the average thickness. Second row: Eigenvalues generated from PCA. Third row: First principal component spectral decomposition, representing the average absorption spectrum of the entire specimen. Fourth row: Second principal component spectral decomposition. Fifth row: Third principal component spectral decomposition. Note that the 2nd and 3rd PCA components potentially embed miscellaneous errors (such as experimental errors from detector nonlinearities) that are mixed in with the average spectrum. However, these subsequent components represent variations with decreasing significance (as indicated by the respective eigenvalues), so any nonlinearity does not significantly affect the main spectroscopic signatures in the data. *(Figure reprinted from [68])*

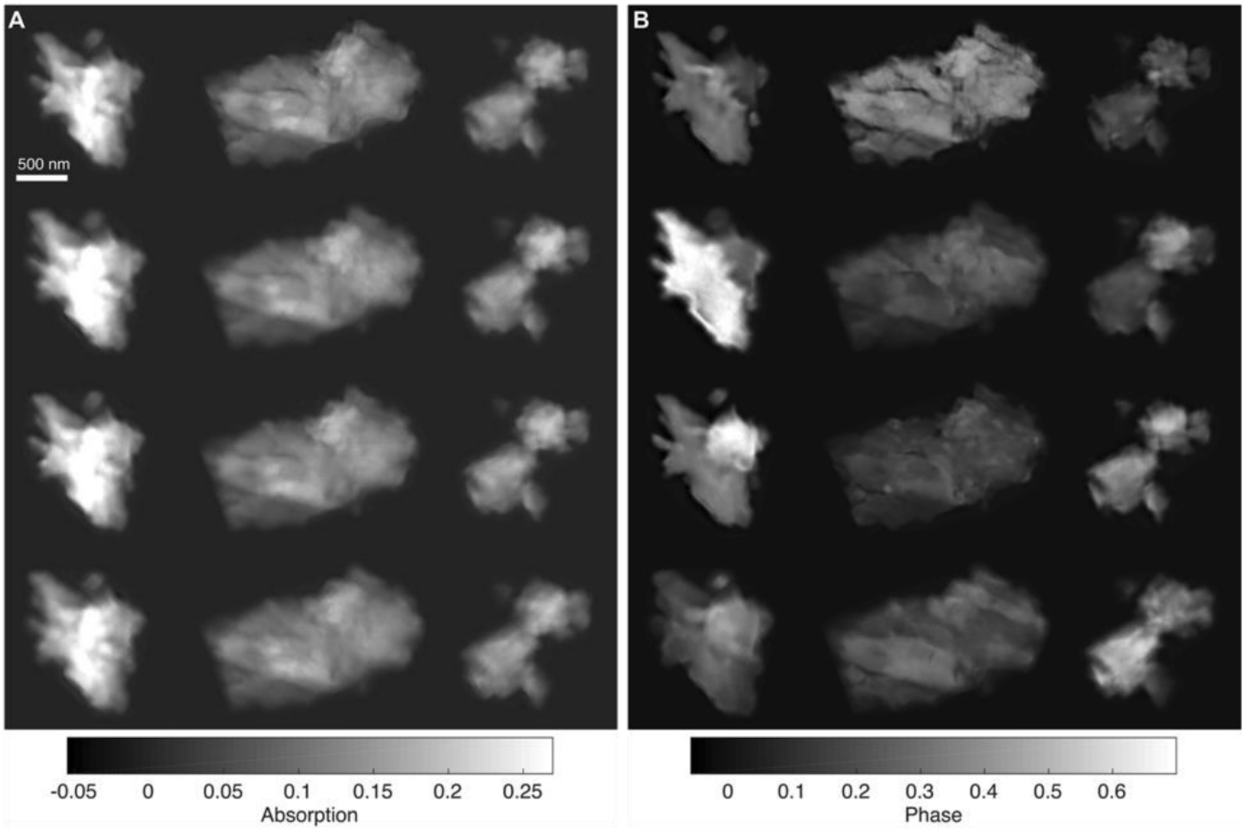

Figure A.S3. X-ray linear dichroic ptychography of coral particles at other energies. (A) Ptychography absorption images of 3 aragonite particles recorded at the *O* pre-edge energy of 534.5 eV across 4 linear polarizations, showing weak polarization-dependent absorption contrast and lower overall spatial resolution due to smaller scattering cross section. (B) Ptychography phase images of the same particles and polarizations recorded on *O* *K*-edge absorption resonance at 536.5 eV, showing strong polarization-dependent phase contrast that is analogous to on-edge absorption contrast. Scale bar: 500 nm. *(Figure reprinted from [68])*

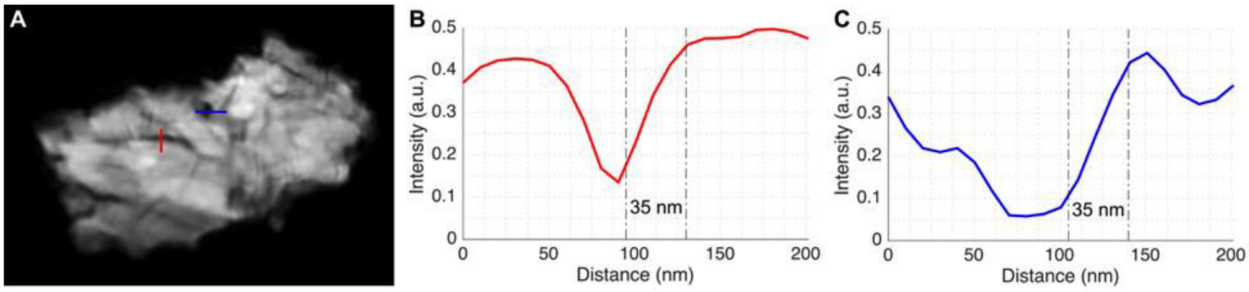

Figure A.S4. Estimated ptychography resolution. (A) Two fine internal features used to estimate highest achieved spatial resolution. (B) (C) Line scans across the fine features. Colors correspond to line cut in (A). Highest resolution achieved by linear dichroic ptychography is estimated to be 35 nm using the knife-edge method with $10-90\%$ intensity cutoff. *(Figure reprinted from [68])*

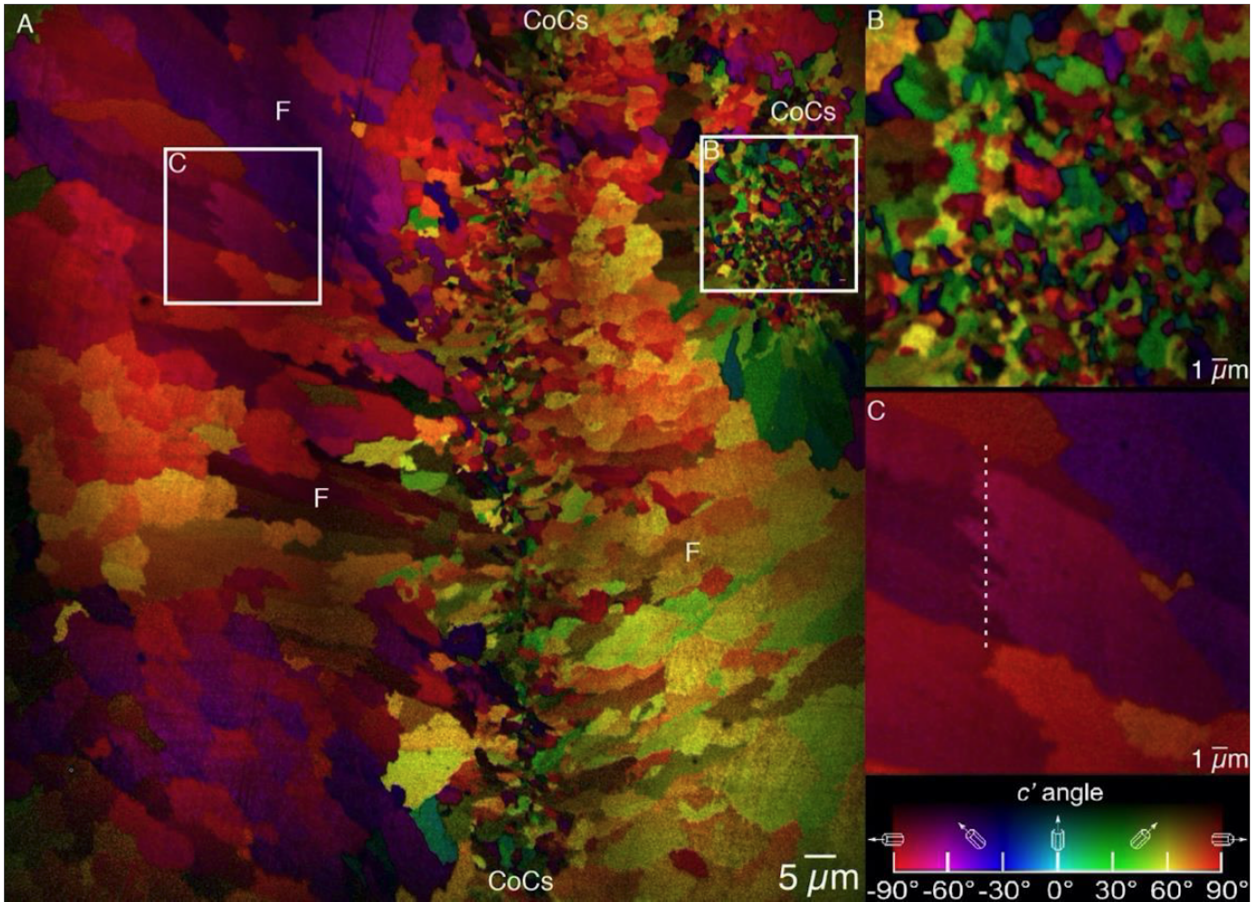

Figure A.S5. PEEM-PIC map of another sample from the same *S. aculeata* coral skeleton. The white boxes indicate the areas magnified in panel (B) and (C). (A) PIC map, where color (hue and brightness) represent the in-plane and off-plane angles of the *c*-axis with respect to the polarization plane. The centers of calcification (CoCs) extend along the vertical line between the two CoCs labels, and in another area on the right (B). Spherulitic fiber (F) crystals (e.g. in C) radiate out of the CoCs, and their angular spreads are narrowly distributed, always within 35°. (B) The CoCs exhibit randomly oriented and thus randomly colored submicron (200−2000 nm) crystals, which have a broadly distributed angular spread. (C) Magnified spherulitic fiber crystals, exhibiting jagged edges. The dashed line indicates a hypothetical cut surface, resulting in spatially separate, but consistently oriented domains with two interspersed orientations. *(Figure reprinted from [68])*

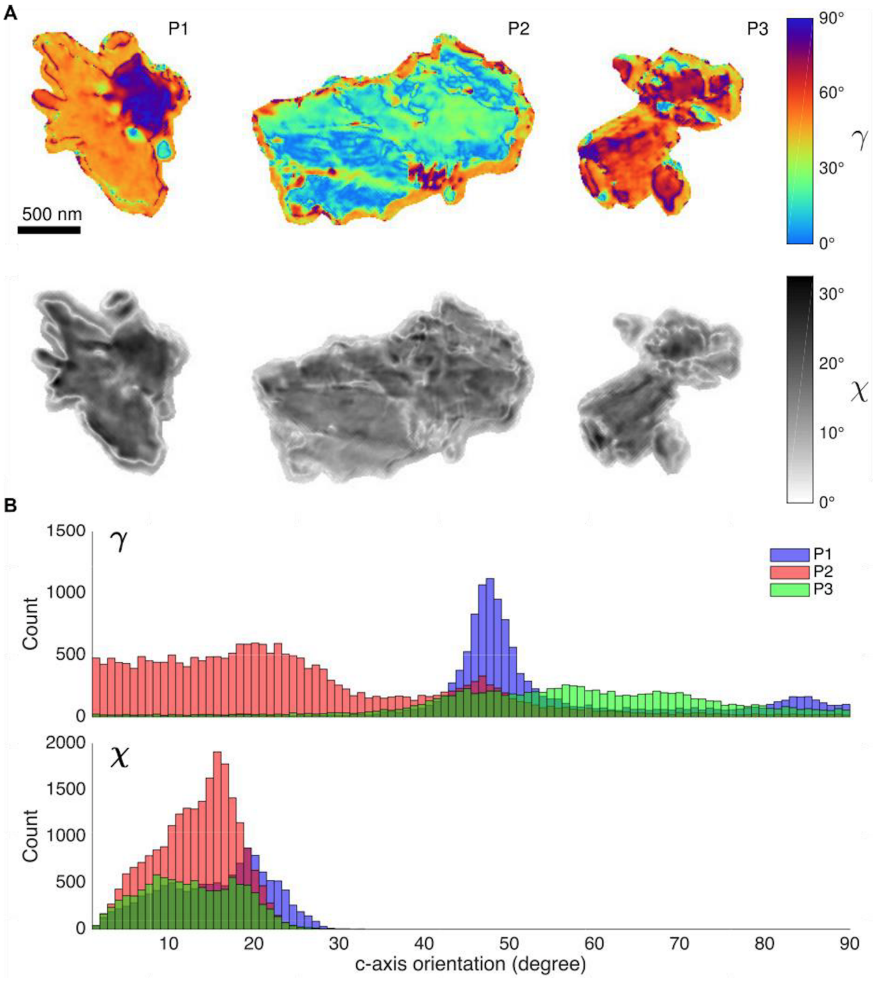

Figure A.S6. Ptychography polarization-dependent contrast (PIC) map of aragonite particles with second set of polarizations. (A) Quantitative PIC maps of the 3 aragonite particles, calculated using 0°, 135° and 90° linear dichroic ptychography images. Hue (top row) denotes in-plane azimuthal crystal *c*-axis angle (γ) of the crystallite, while brightness (bottom row) denotes out-of-plane c-axis angle (χ), all ranging from 0° to 90°. Relative angular spreads in the 3 particles agree well with PIC maps shown in Fig. A.3. (B) Histograms of γ (top) and χ (bottom) for the 3 particles, again showing narrow γ angular spread for $P1$ of $< 35°$, and much broader spread for $P2$ and $P3$ of $> 35°$. Scale bar: 500 nm. *(Figure reprinted from [68])*

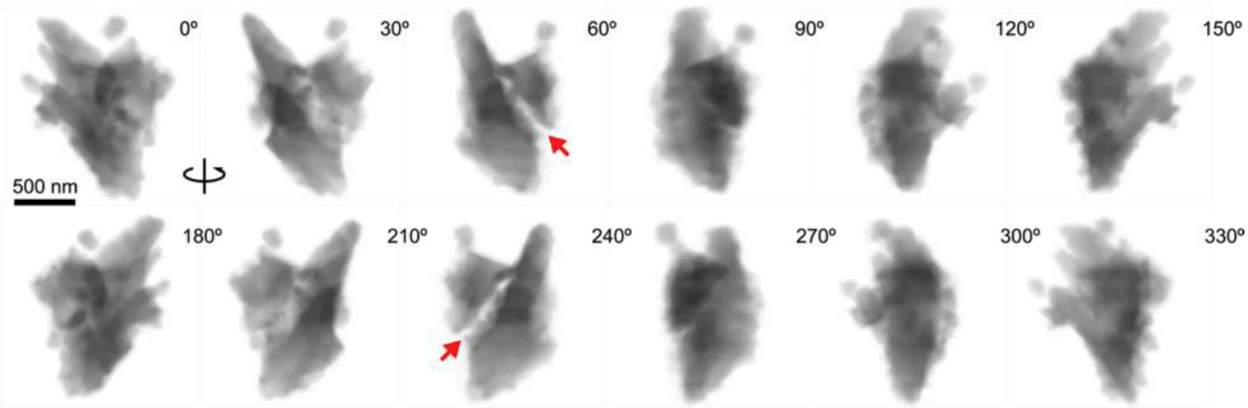

Figure A.S7. Electron tomography of $P1$. Projected azimuthal views of 3D coral particle, rotated to the right in 30° increments. Views along the 60° and 210° reveal the coral particle consists of two joint particles overlapping on top of each other (red arrows). This explains the drastic orientational change across the two subdomains that is observed in Fig. A.3's PIC map. Scale bar: 500 nm. *(Figure reprinted from [68])*

REFERENCES

[1] D. Sayre, "Some implications of a theorem due to Shannon", *Acta Crystallographica*, vol. 5, no. 6, pp. 843–843, 1952.

[2] R. Bates, *Fourier Phase problems are uniquely solvable in more than 1 dimension*, 1982.

[3] J. Miao, D. Sayre, and H. N. Chapman, "Phase retrieval from the magnitude of the Fourier transforms of nonperiodic objects", *Journal of the Optical Society of America A*, vol. 15, no. 6, p. 1662, Jun. 1998.

[4] J. Miao, T. Ishikawa, E. H. Anderson, and K. O. Hodgson, "Phase retrieval of diffraction patterns from noncrystalline samples using the oversampling method", *Physical Review B*, vol. 67, no. 17, May 2003.

[5] J. Miao, P. Charalambous, J. Kirz, and D. Sayre, "Extending the methodology of X-ray crystallography to allow imaging of micrometre-sized non-crystalline specimens", *Nature*, vol. 400, p. 342, Jul. 1999.

[6] S. P. Boyd and L. Vandenberghe, *Convex optimization*. Cambridge, UK ; New York: Cambridge University Press, 2004, ISBN: 978-0-521-83378-3.

[7] J. R. Fienup, "Reconstruction of a complex-valued object from the modulus of its Fourier Transform using a support constraint", 1987.

[8] J. Rodenburg, "Ptychography and Related Diffractive Imaging Methods", in *Advances in Imaging and Electron Physics*, vol. 150, Elsevier, 2008, pp. 87–184, ISBN: 978-0-12-374217-9.

[9] J. M. Rodenburg, A. C. Hurst, A. G. Cullis, B. R. Dobson, F. Pfeiffer, O. Bunk, C. David, K. Jefimovs, and I. Johnson, "Hard-X-Ray Lensless Imaging of Extended Objects", *Physical Review Letters*, vol. 98, no. 3, p. 034 801, Jan. 2007.

[10] M. Pham, A. Rana, J. Miao, and S. Osher, "Semi-implicit relaxed Douglas-Rachford algorithm (sDR) for ptychography", *Optics Express*, vol. 27, no. 22, p. 31 246, Oct. 2019.

[11] A. M. Maiden and J. M. Rodenburg, "An improved ptychographical phase retrieval algorithm for diffractive imaging", *Ultramicroscopy*, vol. 109, no. 10, pp. 1256–1262, Sep. 2009.

[12] E. Wolf, *Introduction to the theory of coherence and polarization of light*. Cambridge: Cambridge University Press, 2007, ISBN: 978-0-521-82211-4.

[13] L. Mandel and E. Wolf, *Optical coherence and quantum optics*. Cambridge ; New York: Cambridge University Press, 1995, ISBN: 978-0-521-41711-2.

[14] H. S. Bennett and E. A. Stern, "Faraday Effect in Solids", *Physical Review*, vol. 137, no. 2A, A448–A461, Jan. 1965.

[15] J. L. Erskine and E. A. Stern, "Calculation of the ${M}_{23}$ magneto-optical absorption spectrum of ferromagnetic nickel", *Physical Review B*, vol. 12, no. 11, pp. 5016–5024, Dec. 1975.

[16] G. Schütz, W. Wagner, W. Wilhelm, P. Kienle, R. Zeller, R. Frahm, and G. Materlik, "Absorption of circularly polarized x rays in iron", *Physical Review Letters*, vol. 58, no. 7, pp. 737–740, Feb. 1987.

[17] J. Stöhr and Y. Wu, "X-Ray Magnetic Circular Dichroism: Basic Concepts and Theory for 3D Transition Metal Atoms", in *New Directions in Research with Third-Generation Soft X-Ray Synchrotron Radiation Sources*, A. S. Schlachter and F. J. Wuilleumier, Eds., Dordrecht: Springer Netherlands, 1994, pp. 221–250, ISBN: 978-94-010-4375-5.

[18] J. Stöhr and H. C. Siegmann, *Magnetism: from fundamentals to nanoscale dynamics*, ser. Springer series in solid-state sciences 152. Berlin ; New York: Springer, 2006, ISBN: 978-3-540-30282-7.

[19] C. T. Chen, F. Sette, Y. Ma, and S. Modesti, "Soft-x-ray magnetic circular dichroism at the L 2 , 3 edges of nickel", *Physical Review B*, vol. 42, no. 11, pp. 7262–7265, Oct. 1990.

[20] J. J. Sakurai and S. F. Tuan, *Modern quantum mechanics*, Rev. ed. Reading, Mass: Addison-Wesley Pub. Co, 1994, ISBN: 978-0-201-53929-5.

[21] E. C. Stoner and E. P. Wohlfarth, "A mechanism of magnetic hysteresis in heterogeneous alloys", *Philosophical Transactions of the Royal Society of London. Series A, Mathematical and Physical Sciences*, vol. 240, no. 826, pp. 599–642, May 1948.

[22] P. M. Paul, "Observation of a Train of Attosecond Pulses from High Harmonic Generation", *Science*, vol. 292, no. 5522, pp. 1689–1692, Jun. 2001.

[23] M. Hentschel, R. Kienberger, C. Spielmann, G. A. Reider, N. Milosevic, T. Brabec, P. Corkum, U. Heinzmann, M. Drescher, and F. Krausz, "Attosecond metrology", *Nature*, vol. 414, no. 6863, pp. 509–513, 2001.

[24] F. Krausz and M. Ivanov, "Attosecond physics", *Reviews of Modern Physics*, vol. 81, no. 1, pp. 163–234, Feb. 2009.

[25] P. B. Corkum and F. Krausz, "Attosecond science", *Nature Physics*, vol. 3, no. 6, pp. 381–387, Jun. 2007.

[26] P. Agostini and L. F. DiMauro, "The physics of attosecond light pulses", *Reports on Progress in Physics*, vol. 67, no. 8, pp. 1563–1563, Aug. 2004.

[27] A. Baltuška, T. Udem, M. Uiberacker, M. Hentschel, E. Goulielmakis, C. Gohle, R. Holzwarth, V. S. Yakovlev, A. Scrinzi, T. W. Hänsch, and F. Krausz, "Attosecond control of electronic processes by intense light fields", *Nature*, vol. 421, p. 611, Feb. 2003.

[28] J. Itatani, J. Levesque, D. Zeidler, H. Niikura, H. Pépin, J. C. Kieffer, P. B. Corkum, and D. M. Villeneuve, "Tomographic imaging of molecular orbitals", *Nature*, vol. 432, no. 7019, pp. 867–871, Dec. 2004.

[29] A. L. Cavalieri, N. Müller, T. Uphues, V. S. Yakovlev, A. Baltuška, B. Horvath, B. Schmidt, L. Blümel, R. Holzwarth, S. Hendel, M. Drescher, U. Kleineberg, P. M. Echenique, R. Kienberger, F. Krausz, and U. Heinzmann, "Attosecond spectroscopy in condensed matter", *Nature*, vol. 449, no. 7165, pp. 1029–1032, Oct. 2007.

[30] G. Sansone, F. Kelkensberg, J. F. Pérez-Torres, F. Morales, M. F. Kling, W. Siu, O. Ghafur, P. Johnsson, M. Swoboda, E. Benedetti, F. Ferrari, F. Lépine, J. L. Sanz-Vicario, S. Zherebtsov, I. Znakovskaya, A. L'Huillier, M. Y. Ivanov, M. Nisoli, F. Martín, and M. J. J. Vrakking, "Electron localization following attosecond molecular photoionization", *Nature*, vol. 465, p. 763, Jun. 2010.

[31] G. Sansone, E. Benedetti, F. Calegari, C. Vozzi, L. Avaldi, R. Flammini, L. Poletto, P. Villoresi, C. Altucci, R. Velotta, S. Stagira, S. De Silvestri, and M. Nisoli, "Isolated Single-Cycle Attosecond Pulses", *Science*, vol. 314, no. 5798, pp. 443–446, Oct. 2006.

[32] H. Kapteyn, O. Cohen, I. Christov, and M. Murnane, "Harnessing Attosecond Science in the Quest for Coherent X-rays", *Science*, vol. 317, no. 5839, p. 775, Aug. 2007.

[33] T. Popmintchev, M.-C. Chen, D. Popmintchev, P. Arpin, S. Brown, S. Ališauskas, G. Andriukaitis, T. Balčiunas, O. D. Mücke, A. Pugzlys, A. Baltuška, B. Shim, S. E. Schrauth, A. Gaeta, C. Hernández-García, L. Plaja, A. Becker, A. Jaron-Becker, M. M. Murnane, and H. C. Kapteyn, "Bright Coherent Ultrahigh Harmonics in the keV X-ray Regime from Mid-Infrared Femtosecond Lasers", *Science*, vol. 336, no. 6086, p. 1287, Jun. 2012.

[34] J. Li, X. Ren, Y. Yin, K. Zhao, A. Chew, Y. Cheng, E. Cunningham, Y. Wang, S. Hu, Y. Wu, M. Chini, and Z. Chang, "53-attosecond X-ray pulses reach the carbon K-edge", *Nature Communications*, vol. 8, no. 1, p. 186, Dec. 2017.

[35] I. Newton, *Opticks: or, A treatise of the relexions, refractions, inflexions and colours of light : also two treaties of the species and magnitude of curvilinear figures.* London: Royal Society, 1704.

[36] M. Daumas, *Scientific instruments of the seventeenth and eighteenth centuries and their makers*. London: Portman Books, 1989, ISBN: 978-0-7134-0727-3.

[37] W. Chao, B. D. Harteneck, J. A. Liddle, E. H. Anderson, and D. T. Attwood, "Soft X-ray microscopy at a spatial resolution better than 15 nm", *Nature*, vol. 435, no. 7046, p. 1210, Jun. 2005.

[38] J. Miao, T. Ishikawa, I. K. Robinson, and M. M. Murnane, "Beyond crystallography: Diffractive imaging using coherent x-ray light sources", *Science*, vol. 348, no. 6234, pp. 530–535, May 2015.

[39] H. N. Chapman, A. Barty, M. J. Bogan, S. Boutet, M. Frank, S. P. Hau-Riege, S. Marchesini, B. W. Woods, S. Bajt, W. H. Benner, R. A. London, E. Plönjes, M. Kuhlmann, R. Treusch, S. Düsterer, T. Tschentscher, J. R. Schneider, E. Spiller, T. Möller, C. Bostedt, M. Hoener, D. A. Shapiro, K. O. Hodgson, D. v. d. Spoel, F. Burmeister, M. Bergh, C. Caleman, G. Huldt, M. M. Seibert, F. R. N. C. Maia, R. W. Lee, A. Szöke, N. Timneanu, and J. Hajdu, "Femtosecond diffractive imaging with a soft-X-ray free-electron laser", *Nature Physics*, vol. 2, no. 12, pp. 839–843, Dec. 2006.

[40] K. J. Gaffney and H. N. Chapman, "Imaging Atomic Structure and Dynamics with Ultrafast X-ray Scattering", *Science*, vol. 316, no. 5830, p. 1444, Jun. 2007.

[41] P. Thibault, M. Dierolf, A. Menzel, O. Bunk, C. David, and F. Pfeiffer, "High-Resolution Scanning X-ray Diffraction Microscopy", *Science*, vol. 321, no. 5887, pp. 379–382, Jul. 2008.

[42] Y. Nishino, Y. Takahashi, N. Imamoto, T. Ishikawa, and K. Maeshima, "Three-Dimensional Visualization of a Human Chromosome Using Coherent X-Ray Diffraction", *Physical Review Letters*, vol. 102, no. 1, p. 018 101, Jan. 2009.

[43] I. Robinson and R. Harder, "Coherent X-ray diffraction imaging of strain at the nanoscale", *Nature Materials*, vol. 8, no. 4, pp. 291–298, Apr. 2009.

[44] M. M. Seibert, T. Ekeberg, F. R. N. C. Maia, M. Svenda, J. Andreasson, O. Jönsson, D. Odić, B. Iwan, A. Rocker, D. Westphal, M. Hantke, D. P. DePonte, A. Barty, J. Schulz, L. Gumprecht, N. Coppola, A. Aquila, M. Liang, T. A. White, A. Martin, C. Caleman, S. Stern, C. Abergel, V. Seltzer, J.-M. Claverie, C. Bostedt, J. D. Bozek, S. Boutet, A. A. Miahnahri, M. Messerschmidt, J. Krzywinski, G. Williams, K. O. Hodgson, M. J. Bogan, C. Y. Hampton, R. G. Sierra, D. Starodub, I. Andersson, S. Bajt, M. Barthelmess, J. C. H. Spence, P. Fromme, U. Weierstall, R. Kirian, M. Hunter, R. B. Doak, S. Marchesini, S. P. Hau-Riege, M. Frank, R. L. Shoeman, L. Lomb, S. W. Epp, R. Hartmann, D. Rolles, A. Rudenko, C. Schmidt, L. Foucar, N. Kimmel, P. Holl, B. Rudek, B. Erk, A. Hömke, C. Reich, D. Pietschner, G. Weidenspointner, L. Strüder, G. Hauser, H. Gorke, J. Ullrich, I. Schlichting, S. Herrmann, G. Schaller, F. Schopper, H. Soltau, K.-U. Kühnel, R. Andritschke, C.-D. Schröter, F. Krasniqi, M. Bott, S. Schorb, D. Rupp, M. Adolph, T. Gorkhover, H. Hirsemann, G. Potdevin, H. Graafsma, B. Nilsson, H. N. Chapman, and J. Hajdu, "Single mimivirus particles intercepted and imaged with an X-ray laser", *Nature*, vol. 470, no. 7332, pp. 78–81, Feb. 2011.

[45] G. Zheng, R. Horstmeyer, and C. Yang, "Wide-field, high-resolution Fourier ptychographic microscopy", *Nature Photonics*, vol. 7, no. 9, pp. 739–745, Sep. 2013.

[46] D. F. Gardner, M. Tanksalvala, E. R. Shanblatt, X. Zhang, B. R. Galloway, C. L. Porter, R. Karl Jr, C. Bevis, D. E. Adams, H. C. Kapteyn, M. M. Murnane, and G. F. Mancini, "Subwavelength coherent imaging of periodic samples using a 13.5 nm tabletop high-harmonic light source", *Nature Photonics*, vol. 11, no. 4, pp. 259–263, Mar. 2017.

[47] M. Holler, M. Guizar-Sicairos, E. H. R. Tsai, R. Dinapoli, E. Müller, O. Bunk, J. Raabe, and G. Aeppli, "High-resolution non-destructive three-dimensional imaging of integrated circuits", *Nature*, vol. 543, no. 7645, pp. 402–406, Mar. 2017.

[48] Y. Jiang, Z. Chen, Y. Han, P. Deb, H. Gao, S. Xie, P. Purohit, M. W. Tate, J. Park, S. M. Gruner, V. Elser, and D. A. Muller, "Electron ptychography of 2D materials to deep sub-ångström resolution", *Nature*, vol. 559, no. 7714, pp. 343–349, Jul. 2018.

[49] F. Pfeiffer, "X-ray ptychography", *Nature Photonics*, vol. 12, no. 1, pp. 9–17, Jan. 2018.

[50] L. W. Whitehead, G. J. Williams, H. M. Quiney, D. J. Vine, R. A. Dilanian, S. Flewett, K. A. Nugent, A. G. Peele, E. Balaur, and I. McNulty, "Diffractive Imaging Using Partially Coherent X Rays", *Physical Review Letters*, vol. 103, no. 24, Dec. 2009.

[51] B. Abbey, L. W. Whitehead, H. M. Quiney, D. J. Vine, G. A. Cadenazzi, C. A. Henderson, K. A. Nugent, E. Balaur, C. T. Putkunz, A. G. Peele, G. J. Williams, and I. McNulty, "Lensless imaging using broadband X-ray sources", *Nature Photonics*, vol. 5, no. 7, pp. 420–424, Jun. 2011.

[52] S. Witte, V. T. Tenner, D. W. Noom, and K. S. Eikema, "Lensless diffractive imaging with ultra-broadband table-top sources: From infrared to extreme-ultraviolet wavelengths", *Light: Science & Applications*, vol. 3, no. 3, e163, Mar. 2014.

[53] J. Huijts, "Broadband Coherent X-ray Diffractive Imaging and Developments towards a High Repetition Rate mid-IR Driven keV High Harmonic Source", PhD thesis.

[54] J. Huijts, S. Fernandez, D. Gauthier, M. Kholodtsova, A. Maghraoui, K. Medjoubi, A. Somogyi, W. Boutu, and H. Merdji, "Broadband Coherent Diffraction for Single-Shot Attosecond Imaging", *arXiv:1909.11345 [physics]*, Sep. 2019.

[55] P. Thibault and A. Menzel, "Reconstructing state mixtures from diffraction measurements", *Nature*, vol. 494, no. 7435, pp. 68–71, Feb. 2013.

[56] D. J. Batey, D. Claus, and J. M. Rodenburg, "Information multiplexing in ptychography", *Ultramicroscopy*, vol. 138, pp. 13–21, Mar. 2014.

[57] B. Enders, M. Dierolf, P. Cloetens, M. Stockmar, F. Pfeiffer, and P. Thibault, "Ptychography with broad-bandwidth radiation", *Applied Physics Letters*, vol. 104, no. 17, p. 171 104, Apr. 2014.

[58] B. Enders, "Development and Application of Decoherence Models in Ptychographic Diffraction Imaging", PhD thesis, Technical University of Munich, 2015.

[59] B. Zhang, D. F. Gardner, M. H. Seaberg, E. R. Shanblatt, C. L. Porter, R. Karl, C. A. Mancuso, H. C. Kapteyn, M. M. Murnane, and D. E. Adams, "Ptychographic hyperspectral spectromicroscopy with an extreme ultraviolet high harmonic comb", *Optics Express*, vol. 24, no. 16, p. 18 745, Aug. 2016.

[60] B. K. Chen, P. Sidorenko, O. Lahav, O. Peleg, and O. Cohen, "Multiplexed single-shot ptychography", *Optics Letters*, vol. 43, no. 21, pp. 5379–5382, Nov. 2018.

[61] A. Rana, J. Zhang, M. Pham, A. Yuan, Y. H. Lo, H. Jiang, S. J. Osher, and J. Miao, "Potential of Attosecond Coherent Diffractive Imaging", *Physical Review Letters*, vol. 125, no. 8, p. 086 101, Aug. 2020.

[62] T. Gaumnitz, A. Jain, Y. Pertot, M. Huppert, I. Jordan, F. Ardana-Lamas, and H. J. Wörner, "Streaking of 43-attosecond soft-X-ray pulses generated by a passively CEP-stable mid-infrared driver", *Optics Express*, vol. 25, no. 22, pp. 27 506–27 518, Oct. 2017.

[63] M. Gallagher-Jones, J. A. Rodriguez, and J. Miao, "Frontier methods in coherent X-ray diffraction for high-resolution structure determination", *Quarterly Reviews of Biophysics*, vol. 49, e20, 2016.

[64] W. Hoppe, "Beugung im inhomogenen Primärstrahlwellenfeld. I. Prinzip einer Phasenmessung von Elektronenbeungungsinterferenzen", *Acta Crystallographica Section A*, vol. 25, no. 4, pp. 495–501, Jul. 1969.

[65] ——, "Trace structure analysis, ptychography, phase tomography", *Ultramicroscopy*, vol. 10, no. 3, pp. 187–198, Jan. 1982.

[66] M. Dierolf, A. Menzel, P. Thibault, P. Schneider, C. M. Kewish, R. Wepf, O. Bunk, and F. Pfeiffer, "Ptychographic X-ray computed tomography at the nanoscale", *Nature*, vol. 467, no. 7314, pp. 436–439, Sep. 2010.

[67] M. Guizar-Sicairos, A. Diaz, M. Holler, M. S. Lucas, A. Menzel, R. A. Wepf, and O. Bunk, "Phase tomography from x-ray coherent diffractive imaging projections", *Optics Express*, vol. 19, no. 22, p. 21 345, Oct. 2011.

[68] Y. H. Lo, J. Zhou, A. Rana, D. Morrill, C. Gentry, B. Enders, Y.-S. Yu, C.-Y. Sun, D. A. Shapiro, R. W. Falcone, H. C. Kapteyn, M. M. Murnane, P. U. P. A. Gilbert, and J. Miao, "X-ray linear dichroic ptychography", *Proceedings of the National Academy of Sciences*, vol. 118, no. 3, e2019068118, Jan. 2021.

[69] S. Eisebitt, J. Lüning, W. F. Schlotter, M. Lörgen, O. Hellwig, W. Eberhardt, and J. Stöhr, "Lensless imaging of magnetic nanostructures by X-ray spectro-holography", *Nature*, vol. 432, no. 7019, pp. 885–888, Dec. 2004.

[70] A. Tripathi, J. Mohanty, S. H. Dietze, O. G. Shpyrko, E. Shipton, E. E. Fullerton, S. S. Kim, and I. McNulty, "Dichroic coherent diffractive imaging", *Proceedings of the National Academy of Sciences*, vol. 108, no. 33, pp. 13 393–13 398, Aug. 2011.

[71] J. J. Turner, X. Huang, O. Krupin, K. A. Seu, D. Parks, S. Kevan, E. Lima, K. Kisslinger, I. McNulty, R. Gambino, S. Mangin, S. Roy, and P. Fischer, "X-Ray Diffraction Microscopy of Magnetic Structures", *Physical Review Letters*, vol. 107, no. 3, Jul. 2011.

[72] C. Donnelly, V. Scagnoli, M. Guizar-Sicairos, M. Holler, F. Wilhelm, F. Guillou, A. Rogalev, C. Detlefs, A. Menzel, J. Raabe, and L. J. Heyderman, "High-resolution hard x-ray magnetic imaging with dichroic ptychography", *Physical Review B*, vol. 94, no. 6, Aug. 2016.

[73] I. Bykova, K. Keskinbora, U. Sanli, J. Gräfe, M. Bechtel, G. Yu, E. Goering, H. Stoll, G. Schütz, and M. Weigand, "Soft X-ray Ptychography for Imaging of Magnetic Domains and Skyrmions in Sub-100 nm Scales", *Microscopy and Microanalysis*, vol. 24, no. S2, pp. 34–35, Aug. 2018.

[74] Y.-S. Yu, R. Celestre, B. Enders, K. Nowrouzi, H. Padmore, T. Warwick, J.-R. Jeong, and D. A. Shapiro, "Nanoscale Visualization of Magnetic Contrasts with Soft X-ray Spectro-Ptychography at the Advanced Light Source", *Microscopy and Microanalysis*, vol. 24, no. S2, pp. 530–531, Aug. 2018.

[75] X. Shi, P. Fischer, V. Neu, D. Elefant, J. C. T. Lee, D. A. Shapiro, M. Farmand, T. Tyliszczak, H.-W. Shiu, S. Marchesini, S. Roy, and S. D. Kevan, "Soft x-ray ptychography studies of nanoscale magnetic and structural correlations in thin SmCo5 films", *Applied Physics Letters*, vol. 108, no. 9, p. 094 103, Feb. 2016.

[76] N. D. Mermin, "The topological theory of defects in ordered media", *Reviews of Modern Physics*, vol. 51, no. 3, pp. 591–648, Jul. 1979.

[77] M. M. Soares, E. de Biasi, L. N. Coelho, M. C. dos Santos, F. S. de Menezes, M. Knobel, L. C. Sampaio, and F. Garcia, "Magnetic vortices in tridimensional nanomagnetic caps observed using transmission electron microscopy and magnetic force microscopy", *Physical Review B*, vol. 77, no. 22, p. 224 405, Jun. 2008.

[78] T. Tanigaki, K. Shibata, N. Kanazawa, X. Yu, Y. Onose, H. S. Park, D. Shindo, and Y. Tokura, "Real-Space Observation of Short-Period Cubic Lattice of Skyrmions in MnGe", *Nano Letters*, vol. 15, no. 8, pp. 5438–5442, Aug. 2015.

[79] X. Yu, J. Masell, F. S. Yasin, K. Karube, N. Kanazawa, K. Nakajima, T. Nagai, K. Kimoto, W. Koshibae, Y. Taguchi, N. Nagaosa, and Y. Tokura, "Real-Space Observation of Topological Defects in Extended Skyrmion-Strings", *Nano Letters*, vol. 20, no. 10, pp. 7313–7320, Oct. 2020.

[80] M. T. Birch, D. Cortés-Ortuño, L. A. Turnbull, M. N. Wilson, F. Groß, N. Träger, A. Laurenson, N. Bukin, S. H. Moody, M. Weigand, G. Schütz, H. Popescu, R. Fan, P. Steadman, J. a. T. Verezhak, G. Balakrishnan, J. C. Loudon, A. C. Twitchett-Harrison, O. Hovorka, H. Fangohr, F. Y. Ogrin, J. Gräfe, and P. D. Hatton, "Real-space imaging of confined magnetic skyrmion tubes", *Nature Communications*, vol. 11, no. 1, p. 1726, Apr. 2020.

[81] J. E. Han and V. H. Crespi, "Tuning Fermi-Surface Properties through Quantum Confinement in Metallic Metalattices: New Metals from Old Atoms", *Physical Review Letters*, vol. 86, no. 4, pp. 696–699, Jan. 2001.

[82] ——, "Abrupt Topological Transitions in the Hysteresis Curves of Ferromagnetic Metalattices", *Physical Review Letters*, vol. 89, no. 19, Oct. 2002.

[83] Y. Liu, S. Kempinger, R. He, T. D. Day, P. Moradifar, S.-Y. Yu, J. L. Russell, V. M. Torres, P. Xu, T. E. Mallouk, S. E. Mohney, N. Alem, N. Samarth, and J. V. Badding, "Confined Chemical Fluid Deposition of Ferromagnetic Metalattices", *Nano Letters*, vol. 18, no. 1, pp. 546–552, Jan. 2018.

[84] W. Döring, "Point Singularities in Micromagnetism", *Journal of Applied Physics*, vol. 39, no. 2, pp. 1006–1007, Feb. 1968.

[85] S. Muhlbauer, B. Binz, F. Jonietz, C. Pfleiderer, A. Rosch, A. Neubauer, R. Georgii, and P. Boni, "Skyrmion Lattice in a Chiral Magnet", *Science*, vol. 323, no. 5916, pp. 915–919, Feb. 2009.

[86] S. Heinze, K. von Bergmann, M. Menzel, J. Brede, A. Kubetzka, R. Wiesendanger, G. Bihlmayer, and S. Blügel, "Spontaneous atomic-scale magnetic skyrmion lattice in two dimensions", *Nature Physics*, vol. 7, no. 9, pp. 713–718, Sep. 2011.

[87] N. Romming, C. Hanneken, M. Menzel, J. E. Bickel, B. Wolter, K. von Bergmann, A. Kubetzka, and R. Wiesendanger, "Writing and Deleting Single Magnetic Skyrmions", *Science*, vol. 341, no. 6146, pp. 636–639, Aug. 2013.

[88] S. Villain-Guillot, R. Dandoloff, A. Saxena, and A. R. Bishop, "Topological solitons and geometrical frustration", *Physical Review B*, vol. 52, no. 9, pp. 6712–6722, Sep. 1995.

[89] R. Streubel, P. Fischer, F. Kronast, V. P. Kravchuk, D. D. Sheka, Y. Gaididei, O. G. Schmidt, and D. Makarov, "Magnetism in curved geometries", *Journal of Physics D: Applied Physics*, vol. 49, no. 36, p. 363 001, Sep. 2016.

[90] V. P. Kravchuk, U. K. Rößler, O. M. Volkov, D. D. Sheka, J. v. d. Brink, D. Makarov, H. Fuchs, H. Fangohr, and Y. Gaididei, "Topologically stable magnetization states on a spherical shell: Curvature stabilized skyrmions", *Physical Review B*, vol. 94, no. 14, p. 144 402, Oct. 2016.

[91] D. Mancilla-Almonacid, M. Castro, J. Fonseca, D. Altbir, S. Allende, and V. Carvalho-Santos, "Magnetic ground states for bent nanotubes", *Journal of Magnetism and Magnetic Materials*, vol. 507, p. 166 754, Aug. 2020.

[92] V. L. Carvalho-Santos, R. M. Corona, D. Altbir, and S. Castillo-Sepúlveda, "Shifts in the skyrmion stabilization due to curvature effects in dome- and antidome-shaped surfaces", *Physical Review B*, vol. 102, no. 2, p. 024 444, Jul. 2020.

[93] V. Vitelli and A. M. Turner, "Anomalous Coupling Between Topological Defects and Curvature", *Physical Review Letters*, vol. 93, no. 21, p. 215 301, Nov. 2004.

[94] M. Pham, Y. Yuan, A. Rana, J. Miao, and S. Osher, "RESIRE: Real space iterative reconstruction engine for Tomography", *arXiv:2004.10445 [eess, math]*, Apr. 2020.

[95] R. Streubel, F. Kronast, P. Fischer, D. Parkinson, O. G. Schmidt, and D. Makarov, "Retrieving spin textures on curved magnetic thin films with full-field soft X-ray microscopies", *Nature Communications*, vol. 6, no. 1, Dec. 2015.

[96] C. Phatak, M. Beleggia, and M. De Graef, "Vector field electron tomography of magnetic materials: Theoretical development", *Ultramicroscopy*, vol. 108, no. 6, pp. 503–513, May 2008.

[97] T. J. Davis, D. Janoschka, P. Dreher, and B. Frank, "Ultrafast vector imaging of plasmonic skyrmion dynamics with deep subwavelength resolution", *Science*, p. 7, 2020.

[98] J. Zou, S. Zhang, and Y. Tserkovnyak, "Topological transport of deconfined hedgehogs in magnets", *arXiv:2006.10910 [cond-mat]*, Jun. 2020.

[99] T. Skyrme, "A non-linear field theory", *Proceedings of the Royal Society of London. Series A. Mathematical and Physical Sciences*, vol. 260, no. 1300, pp. 127–138, Feb. 1961.

[100] J. Zang, V. Cros, and A. Hoffmann, Eds., *Topology in Magnetism*, ser. Springer Series in Solid-State Sciences. Cham: Springer International Publishing, 2018, vol. 192, ISBN: 978-3-319-97333-3.

[101] H.-B. Braun, "Topological effects in nanomagnetism: From superparamagnetism to chiral quantum solitons", *Advances in Physics*, vol. 61, no. 1, pp. 1–116, Feb. 2012.

[102] J. P. Sethna, *Statistical mechanics: entropy, order parameters, and complexity*, ser. Oxford master series in statistical, computational, and theoretical physics 14. Oxford ; New York: Oxford University Press, 2006, ISBN: 978-0-19-856676-2.

[103] J. Zou, S. K. Kim, and Y. Tserkovnyak, "Topological transport of vorticity in Heisenberg magnets", *Physical Review B*, vol. 99, no. 18, p. 180 402, May 2019.

[104] A. K. Jain, M. N. Murty, and P. J. Flynn, "Data clustering: A review", *ACM Computing Surveys*, vol. 31, no. 3, pp. 264–323, Sep. 1999.

[105] D. Cortés-Ortuño, N. Romming, M. Beg, K. von Bergmann, A. Kubetzka, O. Hovorka, H. Fangohr, and R. Wiesendanger, "Nanoscale magnetic skyrmions and target states in confined geometries", *Physical Review B*, vol. 99, no. 21, p. 214 408, Jun. 2019.

[106] D. A. Shapiro, R. Celestre, B. Enders, J. Joseph, H. Krishnan, M. A. Marcus, K. Nowrouzi, H. Padmore, J. Park, A. Warwick, and Y.-S. Yu, "The COSMIC Imaging Beamline at the Advanced Light Source: A new facility for spectro-microscopy of nano-materials", *Microscopy and Microanalysis*, vol. 24, no. S2, pp. 8–11, Aug. 2018.

[107] S. Marchesini, H. Krishnan, B. J. Daurer, D. A. Shapiro, T. Perciano, J. A. Sethian, and F. R. N. C. Maia, "SHARP: A distributed, GPU-based ptychographic solver", *Journal of Applied Crystallography*, vol. 49, no. 4, pp. 1245–1252, Aug. 2016.

[108] A. Maiden, D. Johnson, and P. Li, "Further improvements to the ptychographical iterative engine", *Optica*, vol. 4, no. 7, p. 736, Jul. 2017.

[109] J. P. Hannon, G. T. Trammell, M. Blume, and D. Gibbs, "X-Ray Resonance Exchange Scattering", *Physical Review Letters*, vol. 61, no. 10, pp. 1245–1248, Sep. 1988.

[110] S. W. Lovesey and S. P. Collins, *X-ray scattering and absorption by magnetic materials*, ser. Oxford series on synchrotron radiation 1. Oxford : New York: Clarendon Press ; Oxford University Press, 1996, ISBN: 978-0-19-851737-5.

[111] A. Vansteenkiste, J. Leliaert, M. Dvornik, M. Helsen, F. Garcia-Sanchez, and B. Van Waeyenberge, "The design and verification of MuMax3", *AIP Advances*, vol. 4, no. 10, p. 107 133, Oct. 2014.

[112] X. He, W. Zhong, C.-T. Au, and Y. Du, "Size dependence of the magnetic properties of Ni nanoparticles prepared by thermal decomposition method", *Nanoscale Research Letters*, vol. 8, no. 1, p. 446, 2013.

[113] S. Manna, J. W. Kim, M. V. Lubarda, J. Wingert, R. Harder, F. Spada, V. Lomakin, O. Shpyrko, and E. E. Fullerton, "Characterization of strain and its effects on ferromagnetic nickel nanocubes", *AIP Advances*, vol. 7, no. 12, p. 125 025, Dec. 2017.

[114] J. A. Fernandez-Roldan, Y. P. Ivanov, and O. Chubykalo-Fesenko, "Micromagnetic modelling of magnetic domain walls and domains in cylindrical nanowires", p. 24,

[115] A. V. Oosterom and J. Strackee, "The Solid Angle of a Plane Triangle", *IEEE Transactions on Biomedical Engineering*, vol. BME-30, no. 2, pp. 125–126, Feb. 1983.

[116] H. Edelsbrunner, D. Kirkpatrick, and R. Seidel, "On the shape of a set of points in the plane", *IEEE Transactions on Information Theory*, vol. 29, no. 4, pp. 551–559, Jul. 1983.

[117] R. P. Rambo and J. A. Tainer, "Super-Resolution in Solution X-Ray Scattering and Its Applications to Structural Systems Biology", *Annual Review of Biophysics*, vol. 42, no. 1, pp. 415–441, May 2013.

[118] T.-Y. Lan, P.-N. Li, and T.-K. Lee, "Method to enhance the resolution of x-ray coherent diffraction imaging for non-crystalline bio-samples", *New Journal of Physics*, vol. 16, no. 3, p. 033 016, Mar. 2014.

[119] K. S. Raines, S. Salha, R. L. Sandberg, H. Jiang, J. A. Rodríguez, B. P. Fahimian, H. C. Kapteyn, J. Du, and J. Miao, "Three-dimensional structure determination from a single view", *Nature*, vol. 463, no. 7278, pp. 214–217, Jan. 2010.

[120] J. Song, C. S. Allen, S. Gao, C. Huang, H. Sawada, X. Pan, J. Warner, P. Wang, and A. I. Kirkland, "Atomic Resolution Defocused Electron Ptychography at Low Dose with a Fast, Direct Electron Detector", *Scientific Reports*, vol. 9, no. 1, p. 3919, Dec. 2019.

[121] D. J. Chang, D. S. Kim, A. Rana, X. Tian, J. Zhou, P. Ercius, and J. Miao, "Ptychographic atomic electron tomography: Towards three-dimensional imaging of individual light atoms in materials", *Physical Review B*, vol. 102, no. 17, p. 174 101, Nov. 2020.

[122] M. C. Scott, C.-C. Chen, M. Mecklenburg, C. Zhu, R. Xu, P. Ercius, U. Dahmen, B. C. Regan, and J. Miao, "Electron tomography at 2.4-ångström resolution", *Nature*, vol. 483, no. 7390, pp. 444–447, Mar. 2012.

[123] C.-C. Chen, C. Zhu, E. R. White, C.-Y. Chiu, M. C. Scott, B. C. Regan, L. D. Marks, Y. Huang, and J. Miao, "Three-dimensional imaging of dislocations in a nanoparticle at atomic resolution", *Nature*, vol. 496, no. 7443, pp. 74–77, Apr. 2013.

[124] R. Xu, C.-C. Chen, L. Wu, M. C. Scott, W. Theis, C. Ophus, M. Bartels, Y. Yang, H. Ramezani-Dakhel, M. R. Sawaya, H. Heinz, L. D. Marks, P. Ercius, and J. Miao, "Three-dimensional coordinates of individual atoms in materials revealed by electron tomography", *Nature Materials*, vol. 14, no. 11, pp. 1099–1103, Nov. 2015.

[125] Y. Yang, C.-C. Chen, M. C. Scott, C. Ophus, R. Xu, A. Pryor, L. Wu, F. Sun, W. Theis, J. Zhou, M. Eisenbach, P. R. C. Kent, R. F. Sabirianov, H. Zeng, P. Ercius, and J. Miao, "Deciphering chemical order/disorder and material properties at the single-atom level", *Nature*, vol. 542, no. 7639, pp. 75–79, Feb. 2017.

[126] H. A. Lowenstam and S. Weiner, *On biomineralization*. New York: Oxford University Press, 1989, ISBN: 978-0-19-504977-0.

[127] U. G. K. Wegst, H. Bai, E. Saiz, A. P. Tomsia, and R. O. Ritchie, "Bioinspired structural materials", *Nature Materials*, vol. 14, no. 1, pp. 23–36, Jan. 2015.

[128] Z. Yin, F. Hannard, and F. Barthelat, "Impact-resistant nacre-like transparent materials", *Science*, vol. 364, no. 6447, pp. 1260–1263, Jun. 2019.

[129] N. K. Dhami, M. S. Reddy, and A. Mukherjee, "Biomineralization of calcium carbonates and their engineered applications: A review", *Frontiers in Microbiology*, vol. 4, 2013.

[130] J. Stöhr, K. Baberschke, R. Jaeger, R. Treichler, and S. Brennan, "Orientation of Chemisorbed Molecules from Surface-Absorption Fine-Structure Measurements: CO and NO on Ni(100)", *Physical Review Letters*, vol. 47, no. 5, pp. 381–384, Aug. 1981.

[131] C.-Y. Sun, M. A. Marcus, M. J. Frazier, A. J. Giuffre, T. Mass, and P. U. P. A. Gilbert, "Spherulitic Growth of Coral Skeletons and Synthetic Aragonite: Nature's Three-Dimensional Printing", *ACS Nano*, vol. 11, no. 7, pp. 6612–6622, Jul. 2017.

[132] T. Mass, A. J. Giuffre, C.-Y. Sun, C. A. Stifler, M. J. Frazier, M. Neder, N. Tamura, C. V. Stan, M. A. Marcus, and P. U. P. A. Gilbert, "Amorphous calcium carbonate particles form coral skeletons", *Proceedings of the National Academy of Sciences*, vol. 114, no. 37, E7670–E7678, Sep. 2017.

[133] C.-Y. Sun, C. A. Stifler, R. V. Chopdekar, C. A. Schmidt, G. Parida, V. Schoeppler, B. I. Fordyce, J. H. Brau, T. Mass, S. Tambutté, and P. U. P. A. Gilbert, "From particle attachment to space-filling coral skeletons", *Proceedings of the National Academy of Sciences*, vol. 117, no. 48, p. 30 159, Dec. 2020.

[134] C.-Y. Sun, L. Gránásy, C. A. Stifler, T. Zaquin, R. V. Chopdekar, N. Tamura, J. C. Weaver, J. A. Y. Zhang, S. Goffredo, G. Falini, M. A. Marcus, T. Pusztai, V. Schoeppler, T. Mass, and P. U. P. A. Gilbert, "Crystal nucleation and growth of spherulites demonstrated by coral skeletons and phase-field simulations", *Acta Biomaterialia*, vol. 120, pp. 277–292, Jan. 2021.

[135] M. J. Olszta, D. J. Odom, E. P. Douglas, and L. B. Gower, "A New Paradigm for Biomineral Formation: Mineralization via an Amorphous Liquid-Phase Precursor", *Connective Tissue Research*, vol. 44, no. 1, pp. 326–334, Jan. 2003.

[136] I. M. Weiss, N. Tuross, L. Addadi, and S. Weiner, "Mollusc larval shell formation: Amorphous calcium carbonate is a precursor phase for aragonite", *Journal of Experimental Zoology*, vol. 293, no. 5, pp. 478–491, Oct. 2002.

[137] R. A. Metzler, J. A. Jones, A. J. D'Addario, and E. J. Galvez, "Polarimetry of *Pinctada fucata* nacre indicates myostracal layer interrupts nacre structure", *Royal Society Open Science*, vol. 4, no. 2, p. 160 893, Feb. 2017.

[138] R. A. Metzler, C. Burgess, B. Regan, S. Spano, and E. J. Galvez, "Polarimetry of nacre in iridescent shells", in *The Nature of Light: Light in Nature V*, vol. 9187, International Society for Optics and Photonics, Sep. 2014, p. 918 704.

[139] R. A. Metzler, M. Abrecht, R. M. Olabisi, D. Ariosa, C. J. Johnson, B. H. Frazer, S. N. Coppersmith, and P. U. P. A. Gilbert, "Architecture of Columnar Nacre, and Implications for Its Formation Mechanism", *Physical Review Letters*, vol. 98, no. 26, Jun. 2007.

[140] R. T. DeVol, R. A. Metzler, L. Kabalah-Amitai, B. Pokroy, Y. Politi, A. Gal, L. Addadi, S. Weiner, A. Fernandez-Martinez, R. Demichelis, J. D. Gale, J. Ihli, F. C. Meldrum, A. Z. Blonsky, C. E. Killian, C. B. Salling, A. T. Young, M. A. Marcus, A. Scholl, A. Doran, C. Jenkins, H. A. Bechtel, and P. U. P. A. Gilbert, "Oxygen Spectroscopy and Polarization-Dependent Imaging Contrast (PIC)-Mapping of Calcium Carbonate Minerals and Biominerals", *The Journal of Physical Chemistry B*, vol. 118, no. 28, pp. 8449–8457, Jul. 2014.

[141] P. U. P. A. Gilbert, A. Young, and S. N. Coppersmith, "Measurement of c-axis angular orientation in calcite (CaCO3) nanocrystals using X-ray absorption spectroscopy", *Proceedings of the National Academy of Sciences*, vol. 108, no. 28, pp. 11 350–11 355, Jul. 2011.

[142] P. U. P. A. Gilbert, K. D. Bergmann, C. E. Myers, M. A. Marcus, R. T. DeVol, C.-Y. Sun, A. Z. Blonsky, E. Tamre, J. Zhao, E. A. Karan, N. Tamura, S. Lemer, A. J. Giuffre, G. Giribet, J. M. Eiler, and A. H. Knoll, "Nacre tablet thickness records formation temperature in modern and fossil shells", *Earth and Planetary Science Letters*, vol. 460, pp. 281–292, Feb. 2017.

[143] H. Ade and B. Hsiao, "X-ray Linear Dichroism Microscopy", *Science*, vol. 262, no. 5138, pp. 1427–1429, Nov. 1993.

[144] J. Miao, K. O. Hodgson, T. Ishikawa, C. A. Larabell, M. A. LeGros, and Y. Nishino, "Imaging whole Escherichia coli bacteria by using single-particle x-ray diffraction", *Proceedings of the National Academy of Sciences*, vol. 100, no. 1, pp. 110–112, Jan. 2003.

[145] H. N. Chapman, A. Barty, S. Marchesini, A. Noy, S. P. Hau-Riege, C. Cui, M. R. Howells, R. Rosen, H. He, J. C. H. Spence, U. Weierstall, T. Beetz, C. Jacobsen, and D. Shapiro, "High-resolution ab initio three-dimensional x-ray diffraction microscopy", *Journal of the Optical Society of America A*, vol. 23, no. 5, p. 1179, May 2006.

[146] C. Song, H. Jiang, A. Mancuso, B. Amirbekian, L. Peng, R. Sun, S. S. Shah, Z. H. Zhou, T. Ishikawa, and J. Miao, "Quantitative Imaging of Single, Unstained Viruses with Coherent X Rays", *Physical Review Letters*, vol. 101, no. 15, p. 158 101, Oct. 2008.

[147] H. Jiang, D. Ramunno-Johnson, C. Song, B. Amirbekian, Y. Kohmura, Y. Nishino, Y. Takahashi, T. Ishikawa, and J. Miao, "Nanoscale Imaging of Mineral Crystals inside Biological Composite Materials Using X-Ray Diffraction Microscopy", *Physical Review Letters*, vol. 100, no. 3, p. 038 103, Jan. 2008.

[148] J. A. Rodriguez, R. Xu, C.-C. Chen, Z. Huang, H. Jiang, A. L. Chen, K. S. Raines, A. Pryor Jr, D. Nam, L. Wiegart, C. Song, A. Madsen, Y. Chushkin, F. Zontone, P. J. Bradley, and J. Miao, "Three-dimensional coherent X-ray diffractive imaging of whole frozen-hydrated cells", *IUCrJ*, vol. 2, no. 5, pp. 575–583, Sep. 2015.

[149] J. M. Rodenburg and H. M. L. Faulkner, "A phase retrieval algorithm for shifting illumination", *Applied Physics Letters*, vol. 85, no. 20, pp. 4795–4797, Nov. 2004.

[150] D. A. Shapiro, Y.-S. Yu, T. Tyliszczak, J. Cabana, R. Celestre, W. Chao, K. Kaznatcheev, A. L. D. Kilcoyne, F. Maia, S. Marchesini, Y. S. Meng, T. Warwick, L. L. Yang, and H. A. Padmore, "Chemical composition mapping with nanometre resolution by soft X-ray microscopy", *Nature Photonics*, vol. 8, no. 10, pp. 765–769, Oct. 2014.

[151] K. Giewekemeyer, P. Thibault, S. Kalbfleisch, A. Beerlink, C. M. Kewish, M. Dierolf, F. Pfeiffer, and T. Salditt, "Quantitative biological imaging by ptychographic x-ray

diffraction microscopy", *Proceedings of the National Academy of Sciences*, vol. 107, no. 2, pp. 529–534, Jan. 2010.

[152] J. Deng, D. J. Vine, S. Chen, Y. S. G. Nashed, Q. Jin, N. W. Phillips, T. Peterka, R. Ross, S. Vogt, and C. J. Jacobsen, "Simultaneous cryo X-ray ptychographic and fluorescence microscopy of green algae", *Proceedings of the National Academy of Sciences*, vol. 112, no. 8, pp. 2314–2319, Feb. 2015.

[153] I. Zanette, B. Enders, M. Dierolf, P. Thibault, R. Gradl, A. Diaz, M. Guizar-Sicairos, A. Menzel, F. Pfeiffer, and P. Zaslansky, "Ptychographic X-ray nanotomography quantifies mineral distributions in human dentine", *Scientific Reports*, vol. 5, no. 1, p. 9210, Aug. 2015.

[154] M. E. Birkbak, M. Guizar-Sicairos, M. Holler, and H. Birkedal, "Internal structure of sponge glass fiber revealed by ptychographic nanotomography", *Journal of Structural Biology*, vol. 194, no. 1, pp. 124–128, Apr. 2016.

[155] M. Gallagher-Jones, C. S. B. Dias, A. Pryor, K. Bouchmella, L. Zhao, Y. H. Lo, M. B. Cardoso, D. Shapiro, J. Rodriguez, and J. Miao, "Correlative cellular ptychography with functionalized nanoparticles at the Fe L-edge", *Scientific Reports*, vol. 7, no. 1, Dec. 2017.

[156] F. Mastropietro, P. Godard, M. Burghammer, C. Chevallard, J. Daillant, J. Duboisset, M. Allain, P. Guenoun, J. Nouet, and V. Chamard, "Revealing crystalline domains in a mollusc shell single-crystalline prism", *Nature Materials*, vol. 16, no. 9, pp. 946–952, Sep. 2017.

[157] J. Deng, Y. H. Lo, M. Gallagher-Jones, S. Chen, A. Pryor, Q. Jin, Y. P. Hong, Y. S. G. Nashed, S. Vogt, J. Miao, and C. Jacobsen, "Correlative 3D x-ray fluorescence and ptychographic tomography of frozen-hydrated green algae", *Science Advances*, vol. 4, no. 11, eaau4548, Nov. 2018.

[158] A. Lin and M. A. Meyers, "Growth and structure in abalone shell", *Materials Science and Engineering: A*, vol. 390, no. 1-2, pp. 27–41, Jan. 2005.

[159] I. Coronado, M. Fine, F. R. Bosellini, and J. Stolarski, "Impact of ocean acidification on crystallographic vital effect of the coral skeleton", *Nature Communications*, vol. 10, no. 1, p. 2896, Dec. 2019.

[160] C. Ophus, "Four-Dimensional Scanning Transmission Electron Microscopy (4D-STEM): From Scanning Nanodiffraction to Ptychography and Beyond", *Microscopy and Microanalysis*, vol. 25, no. 3, pp. 563–582, Jun. 2019.

[161] R. Celestre, K. Nowrouzi, D. A. Shapiro, P. Denes, J. M. Joseph, A. Schmid, and H. A. Padmore, "Nanosurveyor 2: A Compact Instrument for Nano-Tomography at the Advanced Light Source", *Journal of Physics: Conference Series*, vol. 849, p. 012 047, Jun. 2017.

[162] D. A. Shapiro, R. Celestre, P. Denes, M. Farmand, J. Joseph, A. Kilcoyne, S. Marchesini, H. Padmore, S. V. Venkatakrishnan, T. Warwick, and Y.-S. Yu, "Ptychographic Imaging of Nano-Materials at the Advanced Light Source with the Nanosurveyor Instrument", *Journal of Physics: Conference Series*, vol. 849, p. 012 028, Jun. 2017.

[163] D. Doering, N. Andresen, D. Contarato, P. Denes, J. M. Joseph, P. McVittie, J. Walder, J. Weizeorick, and B. Zheng, "High speed, direct detection 1k Frame-Store CCD sensor for synchrotron radiation", in *2011 IEEE Nuclear Science Symposium Conference Record*, Oct. 2011, pp. 1840–1845.

[164] M. Farmand, R. Celestre, P. Denes, A. L. D. Kilcoyne, S. Marchesini, H. Padmore, T. Tyliszczak, T. Warwick, X. Shi, J. Lee, Y.-S. Yu, J. Cabana, J. Joseph, H. Krishnan, T. Perciano, F. R. N. C. Maia, and D. A. Shapiro, "Near-edge X-ray refraction fine structure microscopy", *Applied Physics Letters*, vol. 110, no. 6, p. 063 101, Feb. 2017.

[165] M. R. Howells, T. Beetz, H. N. Chapman, C. Cui, J. M. Holton, C. J. Jacobsen, J. Kirz, E. Lima, S. Marchesini, H. Miao, D. Sayre, D. A. Shapiro, J. C. H. Spence, and D.

Starodub, "An assessment of the resolution limitation due to radiation-damage in X-ray diffraction microscopy", *Journal of Electron Spectroscopy and Related Phenomena*, Radiation Damage, vol. 170, no. 1, pp. 4–12, Mar. 2009.

[166] L. Rokach and O. Maimon, "Clustering Methods", in *Data Mining and Knowledge Discovery Handbook*, O. Maimon and L. Rokach, Eds., New York: Springer-Verlag, 2005, pp. 321–352, ISBN: 978-0-387-24435-8.

[167] J. Marrison, L. Räty, P. Marriott, and P. O'Toole, "Ptychography – a label free, high-contrast imaging technique for live cells using quantitative phase information", *Scientific Reports*, vol. 3, no. 1, p. 2369, Dec. 2013.

[168] K. Benzerara, N. Menguy, M. Obst, J. Stolarski, M. Mazur, T. Tylisczak, G. E. Brown, and A. Meibom, "Study of the crystallographic architecture of corals at the nanoscale by scanning transmission X-ray microscopy and transmission electron microscopy", *Ultramicroscopy*, vol. 111, no. 8, pp. 1268–1275, Jul. 2011.

[169] L. C. Nielsen, D. J. DePaolo, and J. J. De Yoreo, "Self-consistent ion-by-ion growth model for kinetic isotopic fractionation during calcite precipitation", *Geochimica et Cosmochimica Acta*, vol. 86, pp. 166–181, Jun. 2012.

[170] B. R. Constantz, "Coral Skeleton Construction: A Physiochemically Dominated Process", *PALAIOS*, vol. 1, no. 2, p. 152, Apr. 1986.

[171] B. A. Collins, J. E. Cochran, H. Yan, E. Gann, C. Hub, R. Fink, C. Wang, T. Schuettfort, C. R. McNeill, M. L. Chabinyc, and H. Ade, "Polarized X-ray scattering reveals non-crystalline orientational ordering in organic films", *Nature Materials*, vol. 11, no. 6, pp. 536–543, Jun. 2012.

[172] C. Donnelly, M. Guizar-Sicairos, V. Scagnoli, S. Gliga, M. Holler, J. Raabe, and L. J. Heyderman, "Three-dimensional magnetization structures revealed with X-ray vector nanotomography", *Nature*, vol. 547, no. 7663, pp. 328–331, Jul. 2017.

[173] P. Ferrand, A. Baroni, M. Allain, and V. Chamard, "Quantitative imaging of anisotropic material properties with vectorial ptychography", *Optics Letters*, vol. 43, no. 4, p. 763, Feb. 2018.

[174] T. A. Grünewald, M. Liebi, N. K. Wittig, A. Johannes, T. Sikjaer, L. Rejnmark, Z. Gao, M. Rosenthal, M. Guizar-Sicairos, H. Birkedal, and M. Burghammer, "Mapping the 3D orientation of nanocrystals and nanostructures in human bone: Indications of novel structural features", *Science Advances*, vol. 6, no. 24, eaba4171, Jun. 2020.

[175] E. Beniash, C. A. Stifler, C.-Y. Sun, G. S. Jung, Z. Qin, M. J. Buehler, and P. U. P. A. Gilbert, "The hidden structure of human enamel", *Nature Communications*, vol. 10, no. 1, p. 4383, Sep. 2019.

[176] V. Schoeppler, R. Lemanis, E. Reich, T. Pusztai, L. Gránásy, and I. Zlotnikov, "Crystal growth kinetics as an architectural constraint on the evolution of molluscan shells", *Proceedings of the National Academy of Sciences*, vol. 116, no. 41, pp. 20 388–20 397, Oct. 2019.

[177] I. Polishchuk, A. A. Bracha, L. Bloch, D. Levy, S. Kozachkevich, Y. Etinger-Geller, Y. Kauffmann, M. Burghammer, C. Giacobbe, J. Villanova, G. Hendler, C.-Y. Sun, A. J. Giuffre, M. A. Marcus, L. Kundanati, P. Zaslansky, N. M. Pugno, P. U. P. A. Gilbert, A. Katsman, and B. Pokroy, "Coherently aligned nanoparticles within a biogenic single crystal: A biological prestressing strategy", *Science*, vol. 358, no. 6368, pp. 1294–1298, Dec. 2017.

[178] M. Lerotic, R. Mak, S. Wirick, F. Meirer, and C. Jacobsen, "*MANTiS* : A program for the analysis of X-ray spectromicroscopy data", *Journal of Synchrotron Radiation*, vol. 21, no. 5, pp. 1206–1212, Sep. 2014.

[179] L. Muscatine, C. Goiran, L. Land, J. Jaubert, J.-P. Cuif, and D. Allemand, "Stable isotopes (13C and 15N) of organic matrix from coral skeleton", *Proceedings of the National Academy of Sciences*, vol. 102, no. 5, pp. 1525–1530, Feb. 2005.

[180] A. Pryor, Y. Yang, A. Rana, M. Gallagher-Jones, J. Zhou, Y. H. Lo, G. Melinte, W. Chiu, J. A. Rodriguez, and J. Miao, "GENFIRE: A generalized Fourier iterative reconstruction algorithm for high-resolution 3D imaging", *Scientific Reports*, vol. 7, no. 1, Dec. 2017.

[181] J. Zhou, Y. Yang, Y. Yang, D. S. Kim, A. Yuan, X. Tian, C. Ophus, F. Sun, A. K. Schmid, M. Nathanson, H. Heinz, Q. An, H. Zeng, P. Ercius, and J. Miao, "Observing crystal nucleation in four dimensions using atomic electron tomography", *Nature*, vol. 570, no. 7762, pp. 500–503, Jun. 2019.

[182] X. Tian, D. S. Kim, S. Yang, C. J. Ciccarino, Y. Gong, Y. Yang, Y. Yang, B. Duschatko, Y. Yuan, P. M. Ajayan, J. C. Idrobo, P. Narang, and J. Miao, "Correlating the three-dimensional atomic defects and electronic properties of two-dimensional transition metal dichalcogenides", *Nature Materials*, vol. 19, no. 8, pp. 867–873, Aug. 2020.